

Boston University

OpenBU

<http://open.bu.edu>

Boston University Theses & Dissertations

Boston University Theses & Dissertations

2022

Scaling of avalanches

<https://hdl.handle.net/2144/46934>

"Downloaded from OpenBU. Boston University's institutional repository."

BOSTON UNIVERSITY
GRADUATE SCHOOL OF ARTS AND SCIENCES

Dissertation

SCALING OF AVALANCHES

by

SAKIB MATIN

B.A., Boston University, 2017

Submitted in partial fulfillment of the
requirements for the degree of
Doctor of Philosophy

2022

© 2022 by
SAKIB MATIN
All rights reserved

Approved by

First Reader

William Klein, PhD
Professor of Physics

Second Reader

Harvey Gould, PhD
Professor of Physics

Run, rabbit, run
Dig that hole, forget the sun
And when at last the work is done
Don't sit down it's time to dig another one

For long you'll live, and high you'll fly
But only if you ride the tide
And balanced on the biggest wave
You race towards an early grave

Dark Side of the Moon, Pink Floyd

SCALING OF AVALANCHES

SAKIB MATIN

Boston University, Graduate School of Arts and Sciences, 2022

Major Professor: William Klein, PhD
Professor of Physics

ABSTRACT

Many systems are characterized by emergent macroscopic phenomena which cannot be elucidated from microscopic dynamics. Emergent collective activity such as avalanches are ubiquitous in complex systems. Examples of such phenomena include earthquakes, neural avalanches, and the Barkhausen effect, which describes the collective flipping of magnetic domains due to an applied external field. These macroscopic phenomena exhibit universal traits such as scale-invariant distribution functions and universal firing rates, which appear to be independent of the underlying microscopic details. Understanding the mechanism behind these emergent behavior is also of practical importance to researchers in seismology and is an important step to understanding the function of neural avalanches in the brain.

In this thesis, we present a generalization of the Fisher-Stauffer cluster scaling theory, which was originally developed for the study of percolation models and equilibrium thermal systems, such as the Ising model. We apply the generalized Fisher-Stauffer scaling theory to study avalanches in integrate-and-fire systems, which have been used to model earthquakes and networks of neurons. By using the Fisher-Stauffer scaling theory, we identify the critical point and the corresponding tuning parameters in the Olami-Feder-Christensen (OFC) model, which is a discrete time integrate-and-fire system. We also derive universal scaling functions and scaling identities, which

relate the critical exponents in the OFC model. Additionally, we study the scaling behavior in the OFC model with spatial disorder to model earthquake phenomenology, such as Gutenberg-Richter scaling and Omori's law, which characterize temporal clustering of earthquakes. Lastly, we extend our scaling analysis to a simple model of neurons and discuss how the scaling laws for neural avalanches may be verified in future experiments.

Contents

1	Introduction	1
1.1	Power Laws and critical phenomena	2
1.2	Scale invariance and ‘Self-organized’ Criticality	4
1.3	The Olami-Feder-Christensen Model	5
1.4	Structure of the Thesis	8
2	Effective ergodicity breaking phase transition in a driven-dissipative system	11
2.1	Introduction	12
2.2	Breakdown of Effective Ergodicity	14
2.3	Recurrence Plots	16
2.4	Cluster Analysis	19
2.5	Long-Range stress transfer	22
2.6	Discussion	23
3	Scaling theory of avalanches in the Olami-Feder-Christensen Model	26
3.1	Introduction	27
3.2	Olami-Feder-Christensen Model	29
3.3	Fisher-Stauffer Scaling Theory	32
3.4	Scaling when $\eta > \eta_E$	33
3.4.1	Scale Invariant Avalanche Distribution at the Critical point	34
3.4.2	Finite Size Scaling	35
3.4.3	Response Function	39

3.5	Order parameter	40
3.5.1	Scaling Laws	41
3.5.2	Gap Exponent	43
3.5.3	Conditional distribution function relating avalanche size, area and lifetime	43
3.5.4	Universal Firing Rates	46
3.6	Scaling in the deterministic OFC model	48
3.6.1	Generic Scale Invariant Avalanche Distribution	48
3.6.2	Multifractal distribution	49
3.7	Discussion	50
4	Stability of Foreshocks and Aftershocks in the Long-Range Olami-Feder-Christen model	53
4.1	Introduction	53
4.2	Model	55
4.3	Results	55
4.4	Discussion	57
5	Scaling of causal neural avalanches in a neutral model	59
5.1	Introduction	60
5.2	Model	62
5.3	Theory	65
5.4	Scale-free avalanche distribution	68
5.5	Divergent Response Functions	73
5.6	Scaling Relations	74
5.7	Size-Duration scaling of avalanches	75
5.8	Universal Avalanche Profile	76
5.9	Critical Slowing down	78

5.10 Relaxation Dynamics	79
5.11 Discussion	81
6 Scaling theory of Random Walk Return times in Arbitrary Dimensions	85
6.1 Introduction	85
6.2 Model	86
6.3 Scaling Theory	87
6.4 Measured Values of Critical Exponents	89
6.5 Return times for one dimensional walker	89
6.6 Divergence Response Function	93
6.7 Discussion and Future work	96
7 Conclusions and Future Work	98
References	101
Curriculum Vitae	114

List of Tables

6.1	Measures values of τ , σ , and γ critical exponents for random walk return times in $D = 1, 2, 3, 4$	89
-----	--	----

List of Figures

2·1	The normalized inverse stress fluctuation metric as a function of time shows the breakdown of effective ergodicity at the critical noise. (a) For $\eta = 0.06 < \eta_c$ the inverse metric is flat, indicating that the system is not ergodic. (b) For $\eta = \eta_c \approx 0.071$, $\Omega(0)/\Omega(t)$ is initially flat, but becomes approximately linear during the observation time. (c) For $\eta = 0.08 > \eta_c$, $\Omega(0)/\Omega(t)$ is linear, and the system is effectively ergodic.	14
2·2	As the noise η approaches the critical noise η_c there is a rapid increase in the mixing time τ_M .	16
2·3	The dynamics of the stress on a site transitions from recurrent to stochastic as the noise η is increased past the critical noise η_c . The time series of the stress $\sigma(t)$ on a given site and the corresponding recurrence map is shown in the top and bottom rows, respectively. The dark points in the recurrence map corresponds to the recurrences. (a) For $\eta < \eta_c$ the dynamics is strongly recurrent, and the values of the stress on the site are confined to a small subset of the possible values. (b) For $\eta \approx \eta_c$, shown in the middle column, the dynamics is quasi-stationary. (c) If $\eta > \eta_c$, the dynamics is stochastic.	17
2·4	The recurrence fraction f_R as a function of η shows a transition from recurrent to stochastic dynamics for η near η_c .	18
2·5	The critical exponent γ determined from the power law behavior of the mean cluster size, χ , is estimated to be $\approx 2.01 \pm 0.14$.	20

2.6	The critical exponent ν characterizes the divergence of the connectedness length, ξ , and is estimated to be $\approx 1.20 \pm 0.13$	21
2.7	The measured value of Fisher exponents τ and σ is consistent with the hyperscaling laws. The number of clusters of size s , n_s , can be fitted to Eq. (2.6) to estimate the exponents τ and σ . (a) We find $\tau \approx 1.04 \pm 0.14$ for $\eta = 0.071$. (b) For $\eta = 0.08$ we estimate $\sigma = 0.43 \pm 0.03$	22
2.8	The measured value of the fractal dimension d_f is consistent with predictions of hyperscaling. (a) The cluster of failed sites appears to be a fractal. (b) The fractal dimension was computed using a box-counting method. The number of boxes needed to cover the cluster is $N(\delta)$, where δ is the box length. In the limit, that the box length $\delta \rightarrow 0$, the slope of $\ln [N(\delta)/\delta]$ corresponds to the fractal dimension. The estimated fractal dimension is $d_f = 1.79 \pm 0.03$	23
2.9	The critical noise, η_c , in the OFC model decreases as the range of stress transfer is increased.	24
3.1	The distribution of avalanche size s, area a and lifetime l is a power law at only at the critical point at $\lambda = 0$. Large avalanches are exponentially suppressed for finite dissipation $\lambda > 0$. The measured exponents are $\tau_s = 1.26 \pm 0.02$, $\tau_a = 1.23 \pm 0.02$ and $\tau_\ell = 1.37 \pm 0.06$. Insets show data collapse when we plot in terms of the rescaled variables $n_u \left[\lambda^{-\frac{\tau_u}{\sigma_u}} \right] \sim [u\lambda^{1/\sigma_u}]^{-\tau_u} \exp(-u\lambda^{1/\sigma_u})$ for $u = s, a, \ell$ respectively. . .	35
3.2	The characteristic size s_c, area a_c and lifetime ℓ_c diverges as the the critical point is approached $\lambda \rightarrow 0$. The s_c , a_c and ℓ_c are found by fitting the avalanche distributions using Eq. (3.4). The numerical estimates of the critical exponents are $\sigma_s = 0.75 \pm 0.03$, $\sigma_a = 0.97 \pm 0.07$ and $\sigma_\ell = 1.39 \pm 0.06$	36

3.3	The characteristic size s_c, area a_c and lifetime ℓ_c diverges with the system length L at the critical point. For $\lambda = 0$, $u_c \sim L^{1/(\sigma_u \nu)}$ for $u = s, a, \ell$	37
3.4	The distributions for avalanche size, area and lifetime are consistent with finite size scaling. Data collapse in the inset when the rescaled variables in Eq. (3.14) are plotted.	38
3.5	The response functions for avalanche size, area and lifetime, defined in Eq. (3.15), diverge as the critical point is approached. The estimated critical exponents are $\gamma_s = 1.26 \pm 0.04$, $\gamma_a = 1.02 \pm 0.06$, and $\gamma_\ell = 0.69 \pm 0.02$	39
3.6	The response functions diverges with the system length L at the critical point. For $\lambda = 0$, $\chi \sim L^{\gamma_u/\nu}$ for $u = s, a, \ell$	40
3.7	The distribution functions for avalanche size, area and lifetime are characterized by constant gap exponents as $\lambda \rightarrow 0$ for $\eta > \eta_E$. $R_u(k)$, defined in Eq. (3.26), diverges with as power laws $R_u(k) \sim \lambda^{-\frac{1}{\sigma_u}}$	44
3.8	The conditional distribution functions relating avalanche size, area and lifetimes are power laws at the critical point. The size-area conditional distribution function scales as $S(a) \sim a^\zeta$, where $\zeta = 1.38 \pm 0.07$. The size-lifetime conditional distribution function scales as $S(\ell) \sim \ell^\kappa$, where $\kappa = 1.35 \pm 0.07$. The area-lifetime conditional distribution function scales as $A(\ell) \sim \ell^\mu$, where $\mu = 1.77 \pm 0.07$	45
3.9	The OFC model exhibits universal avalanche profiles at the critical point when $\eta > \eta_E$. The rescaled firing rate $Fl^{1-\kappa}$ and rescaled first firing rate $G^{1-\mu}$ as a function of the rescaled time t/l show data collapse in Panels a and b respectively.	47

3.10 **The avalanche size distribution exhibits generic scale invariance in the deterministic OFC model.** The exponent τ_s characterizes the avalanche size distribution and is non-monotonic as a function of the dissipation λ in the OFC model when $\eta = 0$, in contrast to the Fisher-Stauffer scaling forms observed when $\eta > \eta_E$ 49

3.11 **The distribution functions for avalanche size, area and lifetime are not characterized by constant gap exponents in the deterministic OFC model.** $R_u(k)$, defined in Eq. 3.26, does not diverge as power laws when $\lambda \rightarrow 0$ for $\eta = 0$. The rate of divergence of $R_u(k)$ depends on k 50

4.1 **The two-dimensional OFC model with long-range stress transfer and asperities is consistent with Gutenberg Richter scaling in Ref. (Serino et al., 2011).** After the system was initialized, the first $T \times 10^6$ events were discarded, and the distribution for the following 10^6 earthquakes is plotted. The distribution of event sizes follows a power-law with the exponent $\tau = 3/2$. The system size is $L = 300$ with stress transfer range $R = 10$, 5% of the sites are asperities with a failure threshold $V^A = 12.0$, and noise is $\eta = 0.10$. Our parameters values are similar to Ref. (Kazemian et al., 2015). 56

4.2 The long-range OFC model with asperities exhibits strong temporal clustering of events with foreshocks and aftershocks.

The system size is $L = 300$, 5% of the sites are asperities with a failure threshold $V^A = 12.0$, and noise $\eta = 0.10$ is used. The different panels correspond to the time series of the earthquakes recorded after different transients since the initialization of the system. The transient in (a), (b) and (c) are 10^6 , 5×10^6 and 10^7 events respectively. The temporal clustering is non-stationary. The foreshocks and aftershocks becomes less pronounced over time. 57

4.3 Weakening temporal clustering of earthquakes in the OFC model is due to desynchronization of the stress on the asperity sites.

(a) and (b) correspond to a transient of 10^6 events. The sharp temporal clustering in (a) may be due to the large fraction of asperities that fail during the main shock as seen in (b). (c) and (d) correspond a transient of 10^7 events. (c) shows weaker temporal clustering compared to (a). 58

5.1 **Neutral theory describes the dynamics of causal neural avalanches.**

The boxes correspond to neurons and each column to the right is the system at a later time step. Different colors correspond to different causal avalanches. The rates for the dynamics are identical for all avalanches. A new avalanche is triggered at the driving rate ϵ and is marked with a star. An active neuron can trigger an inactive neuron anywhere in the system at the propagation rate λ . Both neurons share the same label as they are causally connected. An active neuron becomes inactive at the decay rate μ . For the neural avalanche labeled by black, the size $S = 2$ is the total number of activated neurons and the duration $D = 2$ is the time elapsed between the first activation until all the black neurons become inactive. 63

5.2 **The distribution of avalanche sizes and durations follows a power law at the critical point, $\Delta = 0$ and $\epsilon = 0$.** There is exponential suppression of large avalanches for $\Delta > 0$ and $\epsilon > 0$. The various exponents are the same for both tuning parameters. The inset shows data-collapse for the causal avalanche distributions. In the **top row**, $\Delta = 0$ and ϵ is varied. (A) The exponents for the avalanche size distribution $\tau = 1.53 \pm 0.05$. (B) The avalanche duration distribution is characterized by $\tau_D = 1.92 \pm 0.11$. In the **bottom row**, Δ is varied for $\epsilon = 0$. (C) The corresponding exponent $\tau = 1.51 \pm 0.05$. (D) $\tau_D = 1.93 \pm 0.11$ is the critical exponent for the avalanche duration distribution. 71

5.3	<p>The characteristic avalanche size S_c and duration D_c diverge as the critical point is approached. For each value of Δ or ϵ, we fit the avalanche size and duration distributions to Eq. 5.10 and Eq. 5.11 to obtain S_c and D_c respectively. In the top row, ϵ is varied at fixed $\Delta = 0$. (A) The characteristic avalanche size S_c diverges with critical exponent $\sigma = 0.54 \pm 0.07$. (B) The characteristic duration D_c diverges with critical exponent $\sigma_D = 0.95 \pm 0.06$. In the bottom row, Δ is varied at fixed $\epsilon = 0$. (C) The measured exponent for S_c is $\sigma = 0.52 \pm 0.08$. (D) The characteristic duration diverges with the exponent $\sigma_D = 1.02 \pm 0.09$.</p>	72
5.4	<p>The response function χ diverges as the system approaches the critical point. The exponent γ characterizes the divergence and is the same when the critical point is approached at constant driving $\epsilon = 0$ or $\Delta = 0$. (A) For $\epsilon = 0$, when Δ is varied the exponent is $\gamma = 2.00 \pm 0.02$ (B) Varying the driving rate ϵ, the exponent is $\gamma = 1.97 \pm 0.04$ for $\Delta = 0$.</p>	73
5.5	<p>The scaling of the average avalanche size as a function of the duration at the critical point is consistent with the scaling laws. At the critical point the scaling is $\langle S(D) \rangle \sim D^{1/\sigma\nu z}$. The numerical estimate of $\frac{1}{\sigma\nu z} = 1.96 \pm 0.03$ is consistent with Eq. 5.28.</p>	76
5.6	<p>Neural avalanches have a universal avalanche profile at the critical point. The firing rate scaled by $D^{1-1/(\sigma\nu z)}$ as a function of the rescaled time t/D shows data collapse for avalanches of different durations.</p>	77

5.7 **The equilibration time T_E diverges as the system approaches the critical point $\epsilon \rightarrow 0$ with $\Delta = 0$.** T_E is the the time for $U(t)$ to reach a steady-state value when the neutral contact process is initiated with a single active neuron. We find $T_E \sim \epsilon^{-\nu z}$. The measured value, $\nu z = 0.95 \pm 0.04$, is consistent with scaling arguments. 79

5.8 **The number of unique causal neural avalanches $U(t)$ decays as a power law, $U(t) \sim t^{-\alpha}$, at the critical point.** The measured critical exponent $\alpha = 0.99 \pm 0.04$ matches mean-field value $\alpha_{MF} = 1$. (A) For $\epsilon > 0$ and critical propensity $\Delta = 0$, $U(t)$ reaches a fluctuating state. (B) For sub-critical propensity $\Delta > 0$ and $\epsilon = 0$, $U(t)$ decays exponentially to the absorbing state. Inset plots show data collapse for the rescaled variables. 80

Chapter 1

Introduction

Methods from statistical mechanics such as scaling theory and renormalization group have been used to study how macroscopic collective phenomena emerges from complex interactions between microscopic dynamics (Stanley, 1999; Stanley, 1971; Klein et al., 2007; Klein et al., 1997; Serino et al., 2011; Matin et al., 2020; Sethna et al., 2001; Zapperi et al., 1998). Although very few systems such as the two-dimensional Ising model (Onsager, 1944) can be solved exactly, scaling theory can be used to understand emergent universal behavior commonly observed near phase transitions (Stanley, 1999; Stauffer, 1979; Stauffer and Aharony, 2018; Matin et al., 2021; Sethna et al., 2001; Zapperi et al., 1998). The focus of this thesis is on developing and applying scaling techniques to integrate-and-fire systems, which have been used to model earthquakes (Olami et al., 1992; Klein and Rundle, 1993; Serino et al., 2011; Matin et al., 2020; Kazemian et al., 2015; Hergarten and Neugebauer, 2002), and neural systems (Hopfield and Herz, 1995; Millman et al., 2010a; Martinello et al., 2017; Matin et al., 2021).

We will generalize the cluster scaling techniques developed in study of percolation models (Stauffer, 1979; Stauffer and Aharony, 2018) to study the cascades of activity, also known as avalanches, in integrate-and-fire model (Olami et al., 1992; Matin et al., 2020; Millman et al., 2010a). Avalanches have been observed in many disparate systems (Serino et al., 2011; Zierenberg et al., 2018a; de Carvalho and Prado, 2000; Fontenele et al., 2019a; Sethna et al., 2001; Matin et al., 2021; Gleeson and Durrett,

2017). There is strong evidence of universal behavior such as power law distributions (Serino et al., 2011; Zierenberg et al., 2018a; de Carvalho and Prado, 2000) and universal firing rates (Fontenele et al., 2019a; Sethna et al., 2001; Martin et al., 2021; Gleeson and Durrett, 2017). A deeper theoretical understanding of avalanches is of great practical importance to researchers in seismology (Kawamura et al., 2012; Serino et al., 2011), and also is an important step to understanding the function of neural avalanches for brain function (Muñoz, 2018a; Fontenele et al., 2019a; Beggs and Plenz, 2003; Chialvo, 2010).

1.1 Power Laws and critical phenomena

Many-body physical systems often exhibit scale invariant behaviors (Stanley, 1971; Stanley, 1999). To illustrate the physics processes we consider the example of the ordinary bar magnet, discussed in Ref. (Stanley, 1999), as an example of critical phenomena in everyday life. A bar magnet is ferromagnetic at room temperatures, and is capable of picking up objects that can be magnetized, such as thumb tacks. However, if we heat a bar magnet to a sufficiently high temperature, all thumb tacks will eventually fall to the ground as the bar magnetic has now lost its ferromagnetic properties and becomes a paramagnet (Stanley, 1999). For the bar magnet, the order parameter is the magnetization m , which goes continuously to zero at some critical temperature T_c (Stanley, 1999; Stanley, 1971). In fact, the order parameter behaves as a power-law at the critical point (Stanley, 1971),

$$m \sim (T - T_c)^\beta \tag{1.1}$$

where β is a critical exponent. Near the critical point, response functions such as magnetic susceptibility χ and the heat capacity C diverge as power laws,

$$\chi \sim |T - T_c|^{-\gamma} \quad (1.2)$$

$$C \sim |T - T_c|^{-\alpha} \quad (1.3)$$

The divergent response functions are related to emergent fluctuations at all length scales (Stanley, 1999). These critical exponents can be related by scaling laws (Stanley, 1971) and determine the universality class of a system.

We can also study the statistics of magnetic domain (neighboring spins aligned in the same direction) to understand the transition between paramagnetic and ferromagnetic phases. At the critical point, the magnetic domain sizes s are described by power-law distributions (Stauffer and Aharony, 2018; Klein et al., 2007),

$$n_s(s) \sim s^{-\tau} \quad (1.4)$$

where τ is yet another critical exponent. A system is scale-free or scale-invariant when the distribution follows a power law, $n_s \sim s^{-\tau}$ (Matin et al., 2021). We can plot $n_s = N_0 s^{-\tau_s}$ on log-log scaled plot to find a straight line with slope τ (Stauffer and Aharony, 2018; Matin et al., 2021).

For critical phenomena, the scale-invariant behavior requires fine tuning (Stanley, 1999; Stanley, 1971; Stauffer, 1979; Stauffer and Aharony, 2018). In the case of magnetic systems, the temperature has to be tuned to the critical value, $T \rightarrow T_c$ (Stanley, 1971). The emergent scaling behavior in magnetic systems depends on the relevant scaling field $\frac{T-T_c}{T_c}$.

In this thesis, we will apply techniques from statistical mechanics and critical phenomena to understand models of earthquake faults (Olami et al., 1992; Serino et al., 2011; Matin et al., 2020), and neural systems (Millman et al., 2010a; Matin

et al., 2021).

1.2 Scale invariance and ‘Self-organized’ Criticality

Interest in the scaling theory of collective activity or avalanches saw an explosive growth after the introduction of self-organized criticality (SOC) (Bak et al., 1987). SOC claims to describe systems which exhibit scale-invariant or power-law distributed avalanches, similar to critical points in statistical mechanical systems without the fine tuning of any external parameters (Bak et al., 1987). The original publication (Bak et al., 1987) has 9579 citations (at the time of writing), and has been applied to fields such as earthquakes (Hergarten and Neugebauer, 2002; Smyth et al., 2019; Sornette and Sornette, 1989) and neuroscience (Millman et al., 2010a; Muñoz, 2018a).

The two initial paradigmatic examples of SOC were the Bak-Tang-Wiesenfeld (Bak et al., 1987) model and the Manna model (Manna, 1991). Both models consist of a two-dimensional lattice of sites which can carry a certain number of blocks. During the loading stage, blocks are added randomly to different sites. When the number of blocks on a single site reaches some predefined threshold, then the site ‘topples’ or fires and the blocks are transferred to the neighbors. For the BTW model, the toppling threshold is 4, and each of the neighboring site receive one block each. For the Manna model, the height threshold is 2, and two of the neighbors randomly receive one block each. The neighbors that receive the blocks may also exceed the threshold and thereby also topple. The cascade toppling of sites is an avalanche. In the BTW and Manna models, the avalanches exhibit power-law distributions (Manna, 1991; Bak et al., 1987), analogous to the distributions of clusters in Ising and percolation models near their respective critical points (Stanley, 1971; Stanley, 1999; Stauffer and Aharony, 2018). In BTW and Manna models, the blocks leave the system only when sites near the edge of the lattice topple and the blocks are removed from the

system due to the open boundary conditions. In the original models, there is no dissipation in the bulk. Zero bulk dissipation was suggested as a possible necessary requirement for SOC. This suggestion raised the question whether a system could exhibit self-organized criticality in the presence of bulk dissipation.

1.3 The Olami-Feder-Christensen Model

The Olami-Feder-Christensen(OFC) model (Olami et al., 1992) was originally introduced to study how dissipation affects self-organized criticality (Bak et al., 1987). The OFC model was inspired by spring-block models such as Burridge-Knopoff model (Burridge and Knopoff, 1967) and the Rundle-Jackson-Brown model (Rundle and Jackson, 1977). Different variations of the OFC model have been introduced with long-range interactions, and disorder has also been used to model earthquakes (Serino et al., 2011; Kazemian et al., 2015; Klein et al., 2007; Dominguez et al., 2013; Klein et al., 1997; Peixoto and Prado, 2006; Peixoto and Davidsen, 2008; Kotani et al., 2008; Li and Wang, 2018; Duan-Ming et al., 2006). The OFC model is the slow driving limit of integrate-and-fire oscillators, and shares many similarities with the Hopfield models (Hopfield and Herz, 1995; Herz and Hopfield, 1995) of neural systems.

The OFC model consists of sites on a lattice (Olami et al., 1992) or a graph (Lise and Jensen, 1996), where each site holds some stress. Stress is added uniformly, until one site reaches a threshold when it fires. The firing site is reset to some residual stress (with noise in later variants of the OFC model (Serino et al., 2011; Kazemian et al., 2015; Matin et al., 2020)) and the fraction of the stress, that is not dissipated, is transferred to its connected neighbors, which then may also fire. The OFC model is described in more detail in Chapter 2.

Reference. (Olami et al., 1992) introduced and analyzed the deterministic OFC model with open boundary conditions. The OFC model exhibited some unusual

results such as power law distribution of avalanche sizes even for finite dissipation (Olami et al., 1992). The power law exponent which characterizes the avalanche distribution depends on the dissipation (Olami et al., 1992; Christensen and Olami, 1992; Boulter and Miller, 2003; Christensen et al., 1992; Middleton and Tang, 1995). This phenomena is in contrast to the equilibrium thermodynamic models such as the Ising model (Stanley, 1971; Klein et al., 2007) and percolation models (Stauffer and Aharony, 2018; Stauffer, 1979). Additionally, the finite size scaling analysis of the OFC model by the original authors (Olami et al., 1992) yielded some controversial results, namely that characteristic avalanche size with the system length as $s_c \sim L^B$, where $B \sim 2.7$ for finite dissipation ($\lambda > 0$). However, this result was shown to be nonphysical in Ref. (Klein and Rundle, 1993), which argued that the original OFC paper (Olami et al., 1992) did not use sufficiently large system sizes to observe the true scaling behavior. Reference (Grassberger, 1993) studied the 2D NN OFC model for larger system sizes than Ref. (Olami et al., 1992) and suggested that the finite size scaling may not apply to the OFC model, similar to the behavior in the Abelian Sandpile model (Kadanoff et al., 1989; Tebaldi et al., 1999). References (Lise and Paczuski, 2001b; Boulter and Miller, 2003) suggested a mutlifractal function to be a better fit than the standard finite size scaling form. Controversy around the numerical values of the power law exponent persisted. Early work indicated that better algorithms are needed to explore larger system sizes and longer simulation times (Klein and Rundle, 1993; Christensen, 1993).

The numerical analysis of the OFC model took a major leap, when Ref. (Grassberger, 1993) introduced an efficient algorithm to simulate the model. Reference. (Grassberger, 1993) showed that the boundary conditions (open or closed) can affect the dynamics and scaling of the deterministic OFC model. The deterministic OFC model with periodic boundary conditions exhibits periodic dynamics, and for sufficiently

high dissipation only avalanches with a single failing site occur (Grassberger, 1993; Miller and Boulter, 2003). The open boundary condition in the OFC model introduces a spatial inhomogeneity, which leads to the non-periodic scale invariant distribution of avalanches (Grassberger, 1993; Middleton and Tang, 1995; Wissel and Drossel, 2006; Boulter and Miller, 2003; Ramos et al., 2006). Other forms of spatial inhomogeneity such as non-uniform thresholds (Torvund and Frøyland, 1995) or dissipation (Mousseau, 1996) strongly affect the dynamics as well. The deterministic OFC model with open boundaries exhibits intricate spatiotemporal correlations (Middleton and Tang, 1995; Lise and Paczuski, 2001b; Lise and Paczuski, 2001a; Ramos et al., 2006; Drossel, 2002; Hergarten and Neugebauer, 2002). One striking example is partially synchronized stress domains, which appear as patches of identical on-site stress when we plot a snapshot of the system (Middleton and Tang, 1995; Lise and Paczuski, 2001b; Lise and Jensen, 1996). The domains originate at the edges and invade the bulk (Middleton and Tang, 1995; Lise and Paczuski, 2001b; Wissel and Drossel, 2006; Drossel, 2002). The transient time can be defined as the time taken for the invasion to reach the center (Middleton and Tang, 1995; Lise and Paczuski, 2001b; Ceva, 1998; Wissel and Drossel, 2006). The transient time and the characteristic radius of the stress domains depends on the dissipation (Middleton and Tang, 1995; Wissel and Drossel, 2006; Lise and Paczuski, 2001b). Numerical evidence suggests that the scaling exponents of edge and bulk events may be different (Lise and Paczuski, 2001a). The presence of the spatiotemporal correlations and very long transient times makes it difficult to analyze true scaling behavior of the deterministic OFC model (Lise and Paczuski, 2001b; Wissel and Drossel, 2006; Middleton and Tang, 1995; Ceva, 1998; Lise, 2002).

Due to the numerical and mathematical difficulties associated with studying the 2D deterministic OFC model, focus shifted to the Annealed Random Neighbor (ARN)

OFC model (Lise and Jensen, 1996; Kinouchi et al., 1998; Bröker and Grassberger, 1997), which is believed to be the mean-field limit. When a site fires the stress is transferred to four neighbors randomly chosen from the entire system (Lise and Jensen, 1996; Bröker and Grassberger, 1997; Kinouchi et al., 1998; Bröker and Grassberger, 1997). The ARN OFC model is stochastic as the neighbors are randomly chosen each time a site fires. In the ARN OFC model, the exponent which characterizes the avalanche size distribution, is independent of the dissipation (Lise and Jensen, 1996; Chabanol and Hakim, 1997; Bröker and Grassberger, 1997; Kinouchi et al., 1998; Eurich et al., 2002) in contrast to the deterministic OFC model. Early results suggested the ARN OFC model may exhibit scale invariant behavior for finite dissipation (Lise and Jensen, 1996). However, larger simulations using the branching ratio and analytic work showed that the ARN OFC model exhibits scale invariance only in the conservative limit (Chabanol and Hakim, 1997; Bröker and Grassberger, 1997; Miller and Boulter, 2002). Furthermore, the analysis of the fully connected Rundle-Jackson model (which is isomorphic to the OFC model) (Rundle and Jackson, 1977; Brown et al., 1991) reveals that the scale invariant distribution of avalanches is related to an underlying spinodal critical point (Klein et al., 1997; Klein et al., 2007). The majority of this thesis focuses on analyzing different aspects of the OFC model. We present a systematic study of noise, dissipation and disorder in the two-dimensional OFC model in Chapters 2, 3, and 4 respectively.

1.4 Structure of the Thesis

In this thesis, we apply a generalization of the Fisher-Stauffer scaling theory to analyze avalanches or collective activity in integrate-and-fire models. These tools are initially applied to different variations of the OFC model (Olami et al., 1992) in Chapters 2, 3 and 4. Then, we extend our analysis to a simple neural model (Martinello et al.,

2017) as well as the return times of random walks.

In Chapter 2, we perform a systematic study of the noise in the two-dimensional OFC Model with nearest neighbor interactions. We show that the model undergoes a phase transition as a function of the noise. We analyze this phase transition using tools from statistical mechanics such as the Fisher-Stauffer scaling theory (Stauffer, 1979; Stauffer and Aharony, 2018) as well as techniques such as recurrence plots (Eckmann et al., 1995; Marwan et al., 2007), which are commonly used in the study of nonlinear dynamical systems. Lastly, we discuss possible criteria for which tools from equilibrium statistical mechanics may be used to study nonequilibrium phase transitions (Matin et al., 2020).

In Chapter 3, we analyze scaling of avalanches in the OFC model as the bulk dissipation is varied. When the model has sufficiently high noise, the bulk dissipation is the relevant scaling field. Our results indicate that the stochastic two-dimensional OFC model is not consistent with self-organized criticality. The deterministic OFC model exhibits drastically different behavior such as multi-fractal scaling. Our work raises questions about the relation between multi-fractal scaling and apparent self-organized criticality in the deterministic OFC model.

In Chapter 5, we study the OFC model with long-range stress transfer and spatial inhomogeneity, which can lead to temporal clustering of avalanches. We use this variant of the OFC model to simulate foreshocks and aftershocks, which are observed in certain earthquake fault systems (Kazemian et al., 2015).

In Chapter 6, we apply the cluster scaling techniques to study neural avalanches in the model proposed in Ref. (Martinello et al., 2017). Unlike the OFC model, multiple concurrent avalanches can propagate in the system due to the constant bombardment of stimuli. We derive scaling laws for neural system and discuss how these scaling laws may be experimentally verified (Matin et al., 2021; Zierenberg et al., 2018a).

In Chapter 7, we look at the scaling theory of biased random walks return times. Although random walk return times are a well studied problem (Redner, 2001), our scaling analysis suggests that the biased random walk return times exhibits a critical point where the order depends on the dimension of the problem.

Finally, we discuss the impact of our work and outline future research directions in Chapter 8.

Chapter 2

Effective ergodicity breaking phase transition in a driven-dissipative system

This thesis chapter and accompanying appendix was published as the following research article:

Sakib Matin, Chon-Kit Pun, Harvey Gould, and W. Klein, “Effective ergodicity breaking phase transition in a driven-dissipative system,” *Phys. Rev. E* **101**, 022103 (2020).

Abstract

We show that the Olami-Feder-Christensen model exhibits an effective ergodicity breaking transition as the noise is varied. Above the critical noise, the system is effectively ergodic because the time-averaged stress on each site converges to the global spatial average. In contrast, below the critical noise, the stress on individual sites becomes trapped in different limit cycles, and the system is not ergodic. To characterize this transition, we use ideas from the study of dynamical systems and compute recurrence plots and the recurrence rate. The order parameter is identified as the recurrence rate averaged over all sites and exhibits a jump at the critical noise. We also use ideas from percolation theory and analyze the clusters of failed sites to find numerical evidence that the transition, when approached from above, can be characterized by exponents that are consistent with hyperscaling.

2.1 Introduction

The Fermi-Pasta-Ulam-Tsingou model (Berman and Izrailev, 2005) is a well known example of a system that exhibits broken ergodicity. The model exhibits quasi-regular dynamics below the critical energy threshold and reaches equipartition above the threshold. Understanding the nature of this type of transition may help extend the tools of equilibrium statistical mechanics to driven-dissipative systems (Olami et al., 1992), active matter (Vicsek et al., 1995), and other non-equilibrium phenomena.

In this paper we consider the nearest-neighbor Olami-Feder-Christensen (OFC) model (Olami et al., 1992). This model is a driven dissipative system that has been of particular interest in the context of the study of earthquakes. We simulate the OFC model on a square lattice of length L with $N = L^2$ sites and periodic boundary conditions. Each site i is initially assigned a stress $\sigma_i = \sigma_R \pm 0.25r$, where r is a uniform random number between ± 1 . At each time step or plate update the initiating site, which is the site with the maximum stress, is found. The stress on all sites is increased by the same amount such that the stress on the initiating site equals σ_F . This procedure corresponds to the zero velocity limit of the loading plate in the Rundle-Jackson model (Rundle and Jackson, 1977). When site i fails, its stress is reset to the residual stress $\sigma_{R,i} = \sigma_R + r\eta$ and the stress $(1 - \lambda)[(\sigma_i - \sigma_{R,i})/4]$ is transferred to its four nearest neighbors. The magnitude of the noise is η . The value of the dissipation parameter, λ , is $0 \leq \lambda < 1$. Sites fail when the stress is greater than or equal to σ_F . The failure of a site may cause neighboring sites to fail, triggering an avalanche. The stress is redistributed until the stress on all sites is less than σ_F . This process concludes one plate update.

Grassberger (Grassberger, 1994) showed that the OFC model with periodic boundary conditions is deterministic for zero noise and that the dynamics appears to be stochastic for sufficiently high values of the noise. However, the transition between

the two types of behavior was not explored.

In this chapter, we show that there is a effective ergodicity breaking transition in the nearest-neighbor OFC model as the noise is varied. In Sec. 2.2 we show that the OFC model is effectively ergodic (Thirumalai et al., 1989; Thirumalai and Mountain, 1990; Thirumalai and Mountain, 1993) for $\eta > \eta_c$, but is not effectively ergodic which implies not ergodic for $\eta < \eta_c$, where η_c is the critical noise. In Sec. 2.3, we characterize the high and low noise phases using recurrence plots, which are commonly used in nonlinear dynamics (Eckmann et al., 1995). From the recurrence plots of the stress on given sites, we calculate the recurrence rate (Marwan et al., 2007) and define the recurrence fraction, f_R , as the recurrence rate averaged over all sites. The recurrence fraction acts as a order parameter and differentiates the high and low noise phases.

We also use ideas from percolation theory to examine the critical behavior as the critical noise is approached from above. In Sec. 2.4 we treat all sites that fail in a plate update as part of the same cluster and determine the mean cluster size χ and the mean radius of gyration R_G (Stauffer, 1979). We determine the exponents γ and ν associated with the divergence of χ and R_G respectively as $\eta \rightarrow \eta_c$ (Stauffer, 1979). We also measure the Fisher exponents τ and σ for the cluster distribution near the critical noise (Fisher, 1967; Stauffer, 1979). Our measured exponents are consistent with hyperscaling.

The numerical results reported in the following are for $\sigma_F = 2.0$ and $\sigma_R = 1.0$, $\lambda = 0.01$, and $L = 500$. Our results for $\lambda \in [0.005, 0.1]$ are qualitatively similar. For all our runs, we discarded at least the first 5×10^6 plate updates before recording data for 3×10^6 plate updates.

2.2 Breakdown of Effective Ergodicity

For systems with many degrees of freedom, it is difficult to verify if a system is ergodic and ergodicity can be checked rigorously for only a few simple systems (Sinai, 1963). Instead, we use the stress fluctuation metric (Thirumalai et al., 1989; Thirumalai and Mountain, 1990; Thirumalai and Mountain, 1993) to determine if the system is effectively ergodic and to study the transition between phases that are not necessarily in equilibrium. The stress fluctuation metric describes how the spatial variance of the time-averaged stress on each site behaves for very long times. A spatially homogeneous system is effectively ergodic if the time average of the stress on each site approaches the same value. An analysis of the temporal properties of the metric can be found in Refs. (Thirumalai et al., 1989; Thirumalai and Mountain, 1990; Thirumalai and Mountain, 1993).

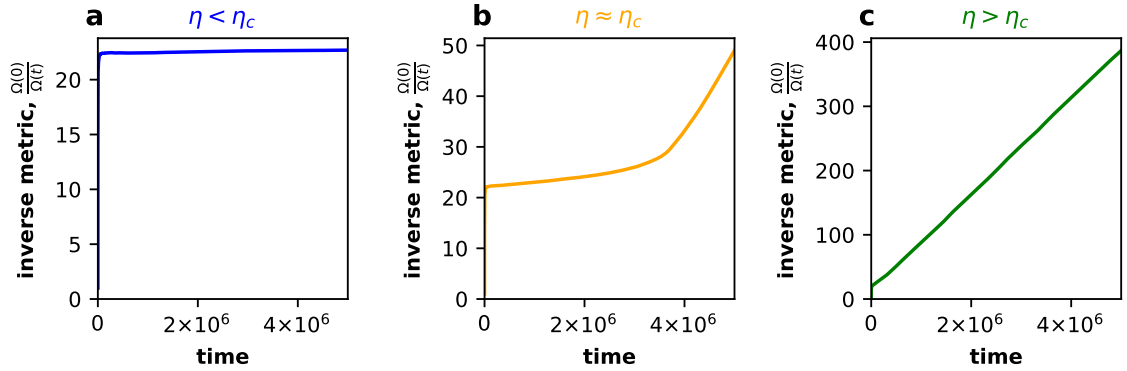


Figure 2-1: The normalized inverse stress fluctuation metric as a function of time shows the breakdown of effective ergodicity at the critical noise. (a) For $\eta = 0.06 < \eta_c$ the inverse metric is flat, indicating that the system is not ergodic. (b) For $\eta = \eta_c \approx 0.071$, $\Omega(0)/\Omega(t)$ is initially flat, but becomes approximately linear during the observation time. (c) For $\eta = 0.08 > \eta_c$, $\Omega(0)/\Omega(t)$ is linear, and the system is effectively ergodic.

We define the time average of the stress at site i , up to time t , as

$$\bar{\sigma}_i(t) = \frac{1}{t} \sum_{t'=1}^t \sigma_i(t'), \quad (2.1)$$

where t represents the number of plate updates. The spatial average of the time-averaged stress on all sites is

$$\langle \sigma(t) \rangle = \frac{1}{N} \sum_{i=1}^N \bar{\sigma}_i(t). \quad (2.2)$$

The stress fluctuation metric is defined as

$$\Omega(t) = \frac{1}{N} \sum_{i=1}^N [\bar{\sigma}_i(t) - \langle \sigma(t) \rangle]^2. \quad (2.3)$$

If the system is effectively ergodic, $\Omega(t)$ approaches zero as $1/t$ (Thirumalai et al., 1989; Thirumalai and Mountain, 1990; Thirumalai and Mountain, 1993). The system is not effectively ergodic during the observation time if the metric reaches a finite value, or does not increase linearly. The fluctuation metric provides a necessary but not sufficient condition for ergodicity.

As shown in Fig. 2-1, the inverse metric increases linearly and the system is effectively ergodic for $\eta > \eta_c \approx 0.071$. For $\eta \approx \eta_c$, the inverse metric is initially flat for some time before showing a slow linear increase. For $\eta < \eta_c$, the inverse metric reaches a plateau, implying that the system is no longer effectively ergodic during our observation time. As the noise is increased past the critical noise, the system transitions from a phase that is not effectively ergodic during the observation time to one that is effectively ergodic.

We can define the mixing time τ_M from the linear behavior of the inverse of the metric for $\eta > \eta_c$ as $\Omega(0)/\Omega(t) = t/\tau_M$. The mixing time is a measure of the how quickly the differences between the time-averaged stress on each site vanishes.

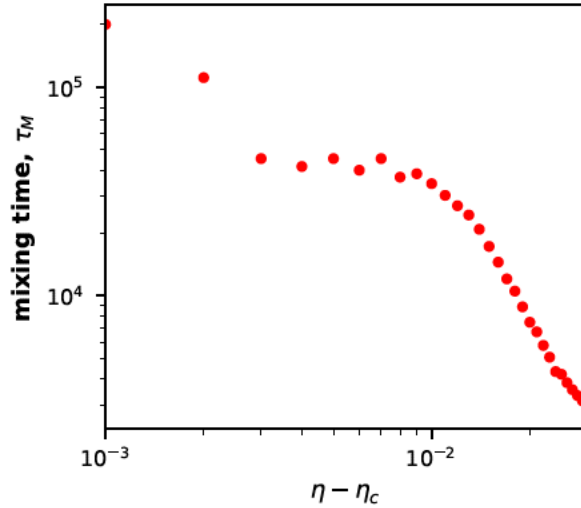


Figure 2.2: As the noise η approaches the critical noise η_c there is a rapid increase in the mixing time τ_M .

Systems for which the differences never approach zero are not ergodic. The mixing time as a function of the noise η is shown in Fig. 2.2. We see that there is an apparent divergence in τ_M as η approaches η_c from above, which implies the existence of critical slowing down.

2.3 Recurrence Plots

We can analyze the dynamical transition using recurrence plots (Marwan et al., 2007; Eckmann et al., 1995) to explore the short term dynamics of the system. The recurrence plots are generated as follows. If the stress on a given site at times t and $t' > t$ differs by less than ϵ , then the corresponding point on the two-dimensional recurrence plot assumes the value one. Otherwise, the value is zero. From the time series of the stress on a given site, the recurrence matrix, $R(t, t')$, is defined as

$$R_{t,t'}(\epsilon) = \begin{cases} 1 & \text{for } |\sigma(t') - \sigma(t)| < \epsilon \\ 0 & \text{for } |\sigma(t') - \sigma(t)| \geq \epsilon. \end{cases} \quad (2.4)$$

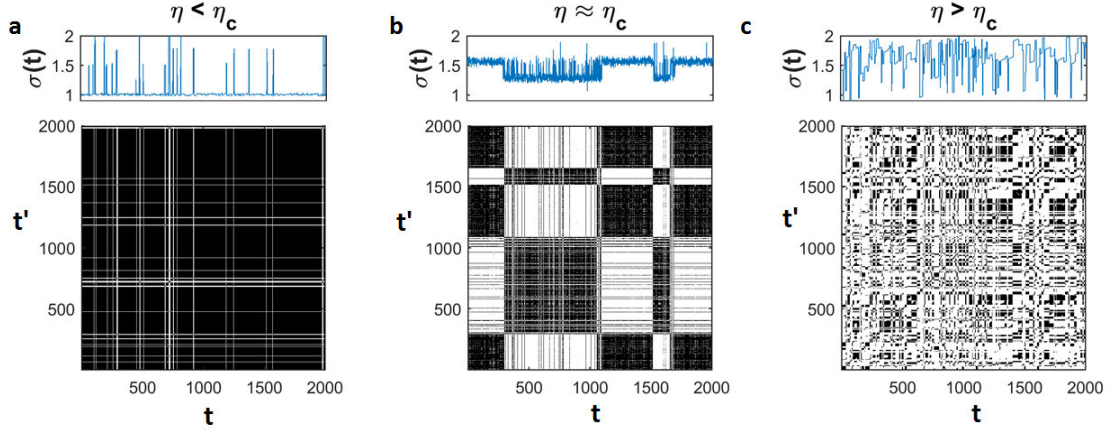


Figure 2-3: The dynamics of the stress on a site transitions from recurrent to stochastic as the noise η is increased past the critical noise η_c . The time series of the stress $\sigma(t)$ on a given site and the corresponding recurrence map is shown in the top and bottom rows, respectively. The dark points in the recurrence map corresponds to the recurrences. (a) For $\eta < \eta_c$ the dynamics is strongly recurrent, and the values of the stress on the site are confined to a small subset of the possible values. (b) For $\eta \approx \eta_c$, shown in the middle column, the dynamics is quasi-stationary. (c) If $\eta > \eta_c$, the dynamics is stochastic.

A common choice for the threshold ϵ is 10% of the range of values that the states can take (Marwan et al., 2007), which in our case is one, leading to the choice $\epsilon = 0.1$. We will show results only for $\epsilon = 0.1$, but our results for other values of ϵ are consistent.

The top row in Fig. 2-3 shows the time series of the stress on a given site and the bottom row shows the corresponding recurrence plot. For $\eta < \eta_c$ in Fig. 2-3(a), the time series of the stress is confined to a narrow set of values. The recurrence plot confirms that the trajectory is strongly recurrent. For $\eta \approx \eta_c$ in Fig. 2-3(b), the time series is quasi-stationary, and the recurrence map shows alternating black and white bands. The dynamics is stochastic for $\eta > \eta_c$, as shown by the time series and the corresponding recurrence map in Fig. 2-3(c). We conclude from the recurrent plots that the dynamics of the stress on a given site undergoes a significant change as the noise is varied from $\eta < \eta_c$ to $\eta > \eta_c$.

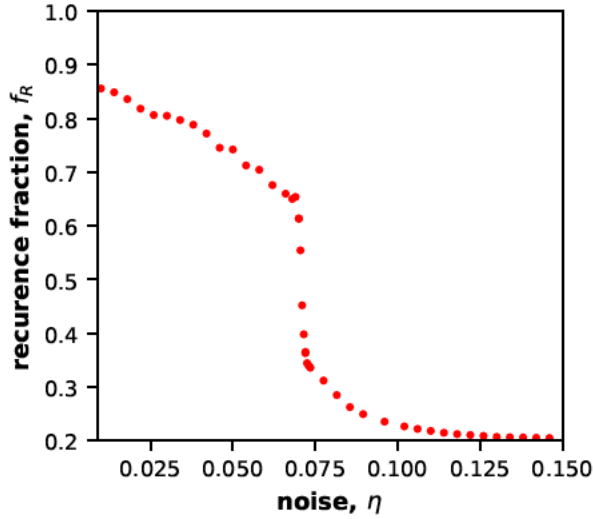


Figure 2-4: The recurrence fraction f_R as a function of η shows a transition from recurrent to stochastic dynamics for η near η_c .

We use the recurrence plots to introduce a scalar order parameter to differentiate between the phases above and below the critical noise. The recurrence rate RR (Marwan et al., 2007) measures the fraction of times the stress on a site returns to the neighborhood of its original value, averaged over all initial conditions. The recurrence rate RR for trajectories of duration, T , is given by

$$\text{RR}^{(i)} = \frac{1}{T^2} \sum_{t,t'=1}^T R_{t,t'}^{(i)}(\epsilon). \quad (2.5)$$

We define the recurrence fraction f_R as the recurrence rate averaged over all sites. We find that f_R averaged over 50 sites, chosen at random, gives a good measure of the average recurrence rate. If $f_R \approx 1$, the system is in the ordered state for which the trajectories of the stress on individual sites appear regular and are restricted to a subset of the allowed values of stress as shown in Fig. 2-3(a). If $f_R \approx 2\epsilon$, the system is in the disordered phase, and the local trajectories fluctuate almost randomly with no well defined order [see Fig. 2-3(c)]. In Fig. 2-3(b), we see quasi-periodic changes in the stress trajectory, and f_R for $\eta \approx \eta_c$ is larger than for $\eta > \eta_c$. Note that f_R

in Fig. 2.4 appears to show a discontinuous jump at η_c . However, we are limited by the rapid increase of the mixing time near $\eta \approx \eta_c$ in determining if there is an actual jump in the order parameter. The rapid change in f_R as the noise is varied implies a divergence in the fluctuations, which we will explore using the cluster analysis of the failed sites.

2.4 Cluster Analysis

In equilibrium statistical mechanics, we can learn about the nature of a transition from the geometric properties of the fluctuations (Coniglio and Klein, 1980; Klein et al., 2007) for certain systems. We map the failed sites onto a percolation problem by assuming that an event of s sites corresponds to a percolation cluster (Serino et al., 2011; Coniglio and Klein, 1980; Dominguez et al., 2013; Fisher, 1967). When the noise is greater than η_c , the system is effectively ergodic and the distribution of the clusters can be fit to a power law with an exponential cutoff as

$$n_s \sim s^{-\tau} \exp(-(\eta - \eta_c)s^\sigma), \quad (2.6)$$

where n_s is the number of clusters with s failed sites and τ and σ are the Fisher exponents. From Fig. 2.7 these exponents are estimated to be $\tau \approx 1.04 \pm 0.14$, and $\sigma = 0.43 \pm 0.03$.

We measure the mean event size (analogous to the susceptibility in thermal systems) χ and the connectedness length (analogous to the correlation length) ξ , which are defined as (Stauffer, 1979)

$$\chi = \frac{\sum_s s^2 n_s}{\sum_s s n_s} \quad (2.7)$$

and

$$\xi = \frac{\sum_s s R_G^2(s) n_s}{\sum_s s n_s}, \quad (2.8)$$

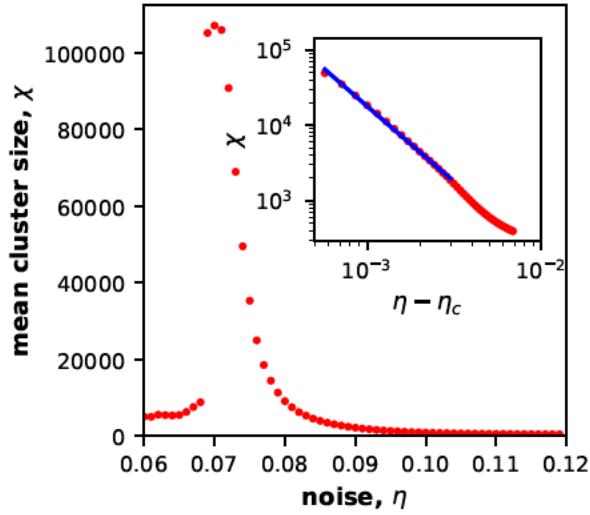


Figure 2-5: The critical exponent γ determined from the power law behavior of the mean cluster size, χ , is estimated to be $\approx 2.01 \pm 0.14$.

where, $R_G(s)$ is the mean radius of gyration of clusters with s sites (Stauffer, 1979). From Fig. 2-5 we see that χ diverges as $(\eta - \eta_c)^{-\gamma}$ with the exponent $\gamma \approx 2.01 \pm 0.14$. Similarly, from Fig. 2-6 we find that $\xi \sim (\eta - \eta_c)^{-\nu}$ with $\nu \approx 1.25 \pm 0.13$. The divergence of the mean cluster size is used to estimate that the critical noise is $\eta_c \approx 0.071$. This value of the critical noise is consistent the value of η at which the jump in the recurrence fraction occurs as seen in Fig 2-4. We are unable to determine the heat capacity and the exponent α directly because we have not identified an energy in the nearest-neighbor OFC model. We have shown that the nearest-neighbor OFC model is not ergodic for $\eta < \eta_c$. In the non-ergodic regime, tools of statistical mechanics may not apply, and we find that we are unable to properly fit critical exponents for $\eta < \eta_c$.

Although the exponents γ , ν , τ , and σ were estimated independently, they are related by hyperscaling scaling laws (Stanley, 1999). To test the consistency of the measured exponents with the scaling relations, we need to add one to the measured value of τ from our simulations, because the clusters in the OFC model are grown from a seed site (Stauffer, 1979; Dominguez et al., 2013). We define $\tilde{\tau} = \tau + 1$ as the

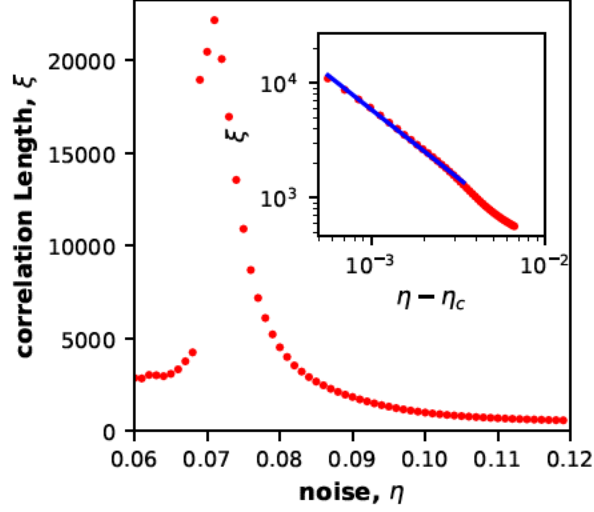


Figure 2-6: The critical exponent ν characterizes the divergence of the connectedness length, ξ , and is estimated to be $\approx 1.20 \pm 0.13$.

corrected exponent and the hyperscaling relations as $\gamma = (3 - \tilde{\tau})/\sigma$ and $\nu = (\tilde{\tau} - 1)/d\sigma$, where d is the spatial dimension. If we substitute $\gamma = 2$, $\nu = 5/4$, and $d = 2$, we find the Fisher exponents to be $\tau = 10/9$ and $\sigma = 4/9$. The predictions of hyperscaling are consistent with our numerical estimates of $\tau \approx 1.04 \pm 0.14$ and $\sigma = 0.43 \pm 0.03$. If we use the additional scaling relations, $\alpha = 2 - (\tilde{\tau} - 1)/\sigma$ and $\beta = (\tilde{\tau} - 2)/\sigma$, we find $\beta = 1/4$ and $\alpha = -1/2$, corresponding to the critical behavior of the order parameter and the heat capacity. We are unable to estimate β directly using f_R because β is close to zero and the range of η over which power law behavior is observed is too small. As we have discussed, we have not been able to identify an energy in the OFC model, so we cannot measure the “specific heat” exponent α directly and can only determine its value indirectly using hyperscaling.

Another exponent that we can measure independently is the fractal dimension, d_f , of the clusters. By using the scaling relations we can express the fractal dimension in terms of the measured exponents and the spatial dimension: $d_f = d - \beta/\nu = d - (\tilde{\tau} - 2)/(\sigma\nu)$. Our measured value of $d_f = 1.79 \pm 0.03$ is consistent with the prediction from hyperscaling.

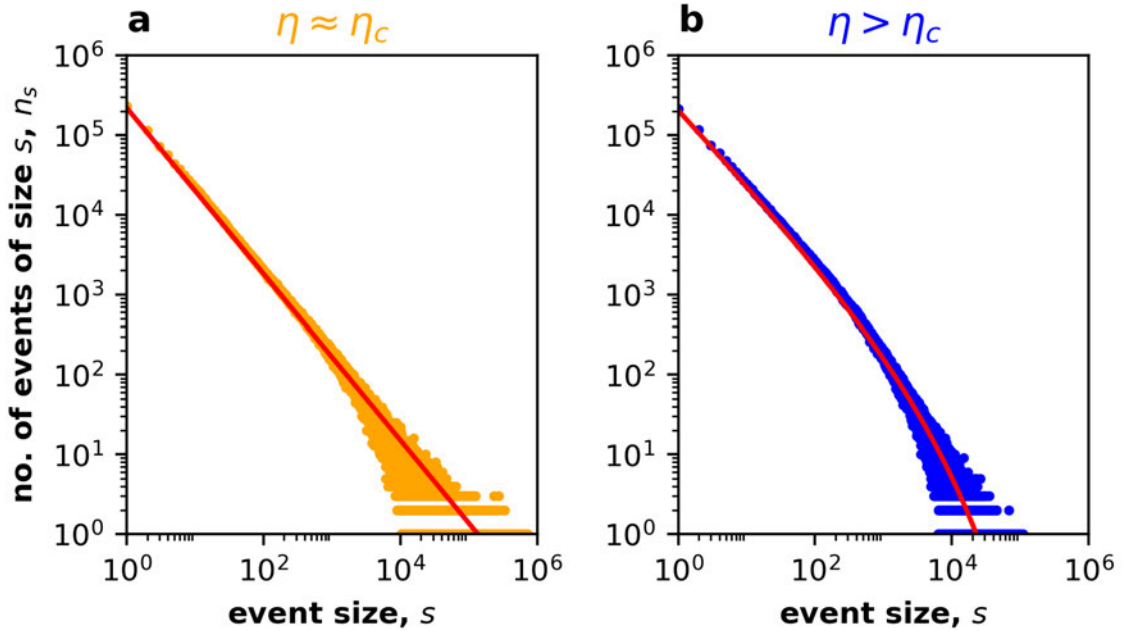


Figure 2-7: The measured value of Fisher exponents τ and σ is consistent with the hyperscaling laws. The number of clusters of size s , n_s , can be fitted to Eq. (2.6) to estimate the exponents τ and σ . (a) We find $\tau \approx 1.04 \pm 0.14$ for $\eta = 0.071$. (b) For $\eta = 0.08$ we estimate $\sigma = 0.43 \pm 0.03$.

2.5 Long-Range stress transfer

Our results for the nearest-neighbor OFC model also apply to long-range stress transfer. In this case, a failing site distributes its stress equally to all sites within a circle of radius, R , the stress transfer range. The nearest neighbor case corresponds to $R = 1$. Figure 2-9 shows that the value of the critical noise decreases as the range of stress transfer increases. For each value of the range R , the jump in the recurrence fraction f_R , the divergence in the mixing time τ_M and the mean cluster size χ occur at the same value of the noise.

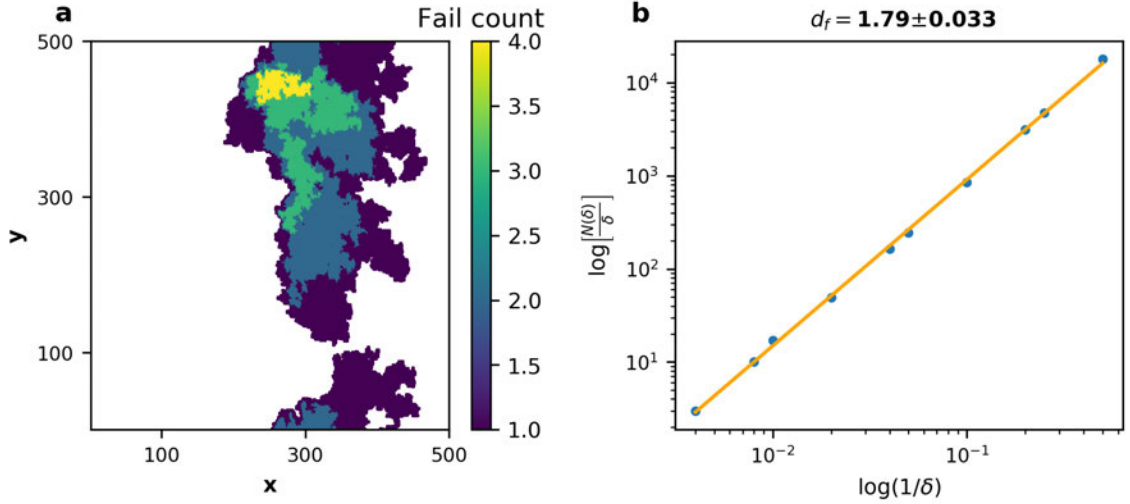


Figure 2-8: The measured value of the fractal dimension d_f is consistent with predictions of hyperscaling. (a) The cluster of failed sites appears to be a fractal. (b) The fractal dimension was computed using a box-counting method. The number of boxes needed to cover the cluster is $N(\delta)$, where δ is the box length. In the limit, that the box length $\delta \rightarrow 0$, the slope of $\ln [N(\delta)/\delta]$ corresponds to the fractal dimension. The estimated fractal dimension is $d_f = 1.79 \pm 0.03$.

2.6 Discussion

We have found a novel phase transition in the OFC model as the noise is varied for all stress transfer ranges studied. Below the critical noise η_c , the system is not ergodic and the stress on the sites appears to evolve via limit cycles. In contrast, for $\eta > \eta_c$ the system is effectively ergodic and the dynamics is stochastic. For $\eta < \eta_c$ recurrence plots show that individual sites are trapped in limit cycles with long lifetimes. As η approaches η_c^- , the limit cycles become unstable, and the trajectories of individual sites show deviations from limit cycle behavior. Larger values of η disrupt the limit cycles and for $\eta > \eta_c$ the trajectories appear random. We find that the recurrence fraction, f_R , is a convenient choice of the order parameter and describes the transition from limit cycle to stochastic behavior. The f_R appears to exhibit a discontinuous jump at $\eta = \eta_c$.

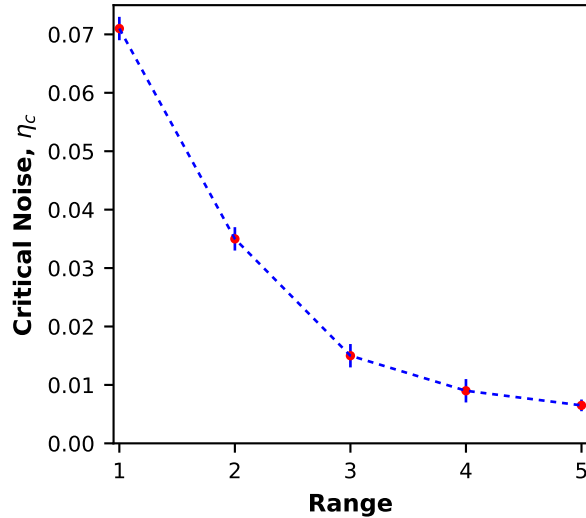


Figure 2.9: The critical noise, η_c , in the OFC model decreases as the range of stress transfer is increased.

We also investigated the transition for $\eta \rightarrow \eta_c^+$ using a cluster analysis to study properties such as the mean cluster size, the connectedness length, and the Fisher exponents. Our measured numerical values of the exponents are consistent with hyperscaling within statistical error. An unusual feature of this “percolation” description of the transition is that there is no “infinite cluster” or avalanche for η above or below η_c . Hence the percolation exponent β associated with how the probability that a site selected at random belongs to the infinite cluster goes to zero as the transition is approached cannot be measured directly. However, a measurement of the fractal dimension $d_f = d - \beta/\nu$ yields a value of β consistent with the relation $\gamma + 2\beta = d\nu$. Our measured critical exponents do not belong to the two-dimensional random percolation universality class. In the OFC model, the sites that fail are correlated. In contrast, the probability of a site being occupied in random site percolation is independent. The critical exponents of correlated models are often different from uncorrelated models such as random percolation (Stauffer, 1979).

Our results indicate that the effect of noise in non-equilibrium phase transitions is

more subtle than was previously suspected and that noise may play a significant role in transitions in systems such as Kuramoto model (Acebrón et al., 2005) and neural systems modeled by integrate-and-fire neurons (Hopfield and Herz, 1995). Of particular interest is the role of noise in the behavior of earthquake faults. The OFC model (and the virtually identical Rundle-Jackson model) with long-range stress transfer has been used to study earthquake fault systems (Serino et al., 2011; Dominguez et al., 2013), where the stress transfer occurs over large distances due to elastic forces. Figure 2-9 shows that the critical noise η_c decreases as the stress transfer range is increased. The noise in real earthquake fault systems is believed to be small (Vasarhelyi and Ván, 2006), so it is possible that earthquake faults operate near the critical noise. Therefore, small changes in the noise due to variations in water content of rocks or changes in the density of microcrack could drive the fault system into a different phase where the dynamics are considerably different. Our results suggest one possible mechanism by which a fault may change its behavior from quasi-periodic to scale-free distribution of events consistent with Gutenberg-Richter scaling (Wesnousky, 1994).

Acknowledgements

We would like to thank Tyler Xuan Gu for prompting the study of the OFC model for low noise and Erik Lascaris, Rashi Verma, and Shan Huang for helpful comments.

Chapter 3

Scaling theory of avalanches in the Olami-Feder-Christensen Model

This thesis chapter is slated for publication as the following research article:

Sakib Matin, Thomas Tenzin, W. Klein, and Harvey Gould. “Scaling theory of avalanches in the Olami-Feder-Christensen model” (manuscript in preparation).

Abstract

Scale invariant avalanches or collective activity are ubiquitous in complex systems. Power-law distributed collective activity such as earthquakes and neural avalanches are striking examples of emergent macroscopic behavior in certain many body systems. Here, we study the avalanches or collective firings of sites in the two-dimensional Olami-Feder-Christensen(OFC) model using the generalized Fisher-Stauffer scaling theory, which was originally developed to study critical fluctuations in thermodynamic systems. Recently work indicates that the strength of the noise in the OFC model can lead to markedly different dynamics. An effective-ergodicity noise threshold separates the two qualitatively different dynamical regimes. We show that when the noise is higher than the effective ergodicity noise threshold, the scale invariant avalanches are observed only at the critical point, which corresponds to dissipation approaching zero. Our work indicates that relevant scaling field is a function of the dissipation. We derive universal scaling functions for avalanche statistics and dynamics. The measured critical exponents are also consistent with the derived scaling laws.

In contrast, we find that the deterministic OFC model exhibits scale invariance for a range of dissipation rates. This generic scale invariance is typically interpreted as self-organized criticality(SOC). We show that the avalanche distributions functions in the deterministic OFC model are consistent with multifractal scaling, which manifests as a set of non-universal scaling exponents. Our work indicates that the strength of the noise strongly affects the scaling in the OFC model. An important question is whether certain systems exhibit apparent SOC behavior because the relevant scaling field is simply tuned to the critical value in the model definition.

3.1 Introduction

Cascades of activity, also known as avalanches, are ubiquitous in nature (Stanley, 1971; Serino et al., 2011; Zierenberg et al., 2018a; Martinello et al., 2017; Pak and Hayakawa, 2011; Fontenele et al., 2019a; Kawamura et al., 2012; Sethna et al., 2001; Beggs and Plenz, 2003; Chialvo, 2010; Herz and Hopfield, 1995; Matin et al., 2021; Matin et al., 2021; Ding and Lu, 1993; Zapperi et al., 1998; Gleeson and Durrett, 2017). Well known examples of avalanches include earthquakes (Serino et al., 2011; Kawamura et al., 2012), collective firings of neurons (neural avalanches) (Zierenberg et al., 2018a; Martinello et al., 2017; Fontenele et al., 2019a; Matin et al., 2021; Beggs and Plenz, 2003), collective flipping of magnetic domains under a driving field (Baukhausen effect) (Sethna et al., 2001; Zapperi et al., 1998) and the growth dynamics of economic systems (Stanley et al., 1996; Frey et al., 2019). In a given system, avalanches may span many spatial and temporal scales (Serino et al., 2011; Zierenberg et al., 2018a; de Carvalho and Prado, 2000; Sethna et al., 2001; Zapperi et al., 1998; Fontenele et al., 2019a; Bonachela and Munoz, 2009; Muñoz et al., 1999b). Although avalanches appear in many disparate systems, certain universal traits such as power law distributions (Serino et al., 2011; Zierenberg et al., 2018a; de Carvalho and

Prado, 2000) and universal firing rates (Fontenele et al., 2019a; Sethna et al., 2001; Matin et al., 2021; Gleeson and Durrett, 2017) appear to be independent of the underlying microscopic details (Stanley, 1999; Stauffer, 1979). A deeper understanding of avalanches is also of practical importance to researchers in siesmology (Kawamura et al., 2012; Serino et al., 2011) and is an important step toward understanding the function of neural avalanches (Muñoz, 2018a; Fontenele et al., 2019a; Beggs and Plenz, 2003; Chialvo, 2010).

We focus on scale invariant or power law distributed avalanches where there is no characteristic scale in the system and avalanches of an arbitrary large size are possible (Stanley, 1971; Stauffer and Aharony, 2018). An open question is whether scale invariant avalanches are related to an underlying critical point (Matin et al., 2021; Matin et al., 2020; Dickman et al., 1998; Hwa and Kardar, 1989; Perković et al., 1995; Vespignani and Zapperi, 1997; Mohanty and Dhar, 2002), similar to equilibrium thermal systems such as the Ising model (Stanley, 1971; Stauffer, 1979; Stauffer and Aharony, 2018). Any deviation from the critical point sets a characteristic scale in the system (Stanley, 1971; Stauffer and Aharony, 2018; Stauffer, 1979). Different physical observeables, which depend on the characteristic scale, diverge as the critical point is approached (Stanley, 1971; Stauffer and Aharony, 2018; Matin et al., 2021). For example, the magnetic domains in the Ising model are power law distributed when the temperature is tuned to its critical value (Stauffer, 1979; Stauffer and Aharony, 2018; Klein et al., 2007). The relevant scaling field in the Ising model is $(T - T_c)/T_c$, where T_c is the critical temperature (Stanley, 1971; Klein et al., 2007). In contrast, an alternate explanation of power-law distributions may be due to self organized criticality(SOC) (Bak et al., 1987; Olami et al., 1992; Turcotte, 1999), which claims to describe systems that exhibit scale-invariance without any apparent fine tuning. The clearest way to rule out SOC in a system is to identify the relevant scaling field

that must be fine tuned to observe scale invariant behavior (Stanley, 1971; Stauffer, 1979; Dickman et al., 1998; Perković et al., 1995).

We present a phenomenological scaling theory of avalanches by generalizing the Fisher-Stauffer cluster scaling theory, which was originally developed in the study of critical phenomena (Fisher, 1967) and percolation models (Stauffer and Aharony, 2018; Stauffer, 1979) and equilibrium thermal models (Coniglio and Klein, 1980). Here, we analyze avalanches in the two-dimensional Olami-Feder-Christensen model (Olami et al., 1992) with nearest neighbor interactions. The OFC model is defined in Sec. 3.2 and we review the results of previous studies of the model and discuss a recent finding that there is an effective ergodicity noise threshold for the 2D OFC model (Matin et al., 2020). Reference (Klein et al., b) show that the two-dimensional OFC model is in thermal equilibrium when the model has sufficiently high noise to be effectively ergodic (Matin et al., 2020). Section 3.3 provides a brief pedagogical introduction to the Fisher-Stauffer scaling theory. We analyze the avalanches using the Fisher-Stauffer scaling theory for noise greater than the effective ergodicity noise threshold in Sec. 3.4. Our results indicate that the scale invariance is caused by an underlying critical point. We show that the avalanches in the deterministic OFC model exhibits multifractal scaling in Sec. 3.6. Lastly, we discuss the implications of our work for other models such as the Bak-Tang-Wiesenfeld sandpile (Bak et al., 1987) and the Manna model (Manna, 1991) in Sec. 3.7.

3.2 Olami-Feder-Christensen Model

The OFC model was originally introduced to understand how dissipation affects self organized criticality (Bak et al., 1987) and has been used to model earthquakes (Serino et al., 2011; Kazemian et al., 2015; Klein et al., 2007; Dominguez et al., 2013; Klein et al., 1997; Peixoto and Prado, 2006; Peixoto and Davidsen, 2008; Kotani et al., 2008;

Li and Wang, 2018; Duan-Ming et al., 2006). The OFC model is the slow driving limit of integrate-and-fire oscillators, and shares many similarities with the Hopfield models (Hopfield and Herz, 1995; Herz and Hopfield, 1995) of neural systems.

We study the two-dimensional OFC model defined on a square lattice with nearest neighbor stress-transfer and open boundary conditions. Each site can hold some stress denoted by $V_{i,j}$. The system is initialized with all sites having stress randomly assigned between the residual stress V^R and the failure threshold V^F . The OFC model is driven uniformly until one site has stress equal to V^F . When the stress on the site equals V^F , it fires and is reset to $V^R + \eta r$, where r is a random uniform number between $[-1, 1]$ and η is the strength of the noise. The stress $(1 - \lambda) [V^F - (V^R + \eta r)] / 4$ is transferred to the four nearest neighbors, where λ is the dissipation rate. The remainder of the stress is dissipated. When a site near the edge fails, more stress is transferred out of the system due to the open boundary conditions. The neighboring sites receive stress from the firing site and fire if the stress exceeds V^F . This cascade of firings is called an avalanche. We record the size s of the avalanche (number of times sites fire), the area a of the avalanche (number of sites that fire at least once) and lifetime ℓ (time between the first and last firing site). No stress is added while an avalanche propagating. This large separation of timescales between the slow driving and fast relaxation gives us well defined local avalanches.

The two-dimensional OFC with nearest-neighbor stress-transfer exhibits remarkably different phenomena when noise is added (Matin et al., 2020). The OFC model undergoes an effective ergodicity (Thirumalai et al., 1989; Thirumalai and Mountain, 1990; Thirumalai and Mountain, 1993; Palmer, 1982) breaking transition at effective ergodicity noise threshold $\eta_E \approx 0.07$ (Matin et al., 2020). When the OFC model has noise $\eta \geq \eta_E$, the system can be characterized by cluster scaling methods (Matin et al., 2020). Similar cluster scaling methods have been applied to Barkhausen noise (Sethna

et al., 2001; Zapperi et al., 1998) and neural avalanches (Matin et al., 2021; Martinello et al., 2017; Fontenele et al., 2019a; Friedman et al., 2012).

In this paper, we will study the scaling behavior of the 2D nearest neighbor OFC model for $\eta > \eta_E$ and contrast the behavior with the deterministic 2D nearest neighbor OFC model. The parameters used for our simulations are $V^R = 1.0$ and $V^F = 2.0$. Linear system size $L = 500$ is used for most simulations. We discard the first 10^8 avalanches before collecting data for a run.

3.3 Fisher-Stauffer Scaling Theory

Universal scaling behavior across disparate systems has led to the scaling hypothesis (Stanley, 1971), which was later justified using renormalization group methods (Wilson, 1983). Certain scaling techniques originally developed in study of critical phenomena (Fisher, 1967) and then applied to percolation models (Stauffer, 1979; Stauffer and Aharony, 2018). We can use the Fisher-Stauffer scaling theory to analyze the critical point in a system by studying the statistics properties of the fluctuations or clusters in the system (Stauffer and Aharony, 2018; Klein et al., 2007; Stanley, 1971). References (Stauffer, 1979; Stauffer and Aharony, 2018) provides detailed discussion of cluster scaling in percolation theory.

Near the critical point, the asymptotic behavior of avalanche or cluster distributions are characterized by power laws (Stanley, 1971; Matin et al., 2020; Stauffer and Aharony, 2018; Klein et al., a). We can obtain thermal quantities from the size distribution n_s (Stauffer and Aharony, 2018). As the system approaches its critical point, the distribution for $s \gg 1$ is

$$n_s \sim s^{-\tau_s} G\left(\frac{s}{s_c}\right), \quad (3.1)$$

where τ_s is a critical exponent that characterizes the power law distribution at the critical point. The characteristic size s_c diverges as $s_c \sim h^{-1/\sigma_s}$, where h is a relevant scaling field. The critical point corresponds to $h = 0$. At the critical point the avalanche distribution functions become $n_s \sim s^{-\tau_s}$. A system is scale-free or scale-invariant when the avalanche distributions follows a power law, $n_s \sim s^{-\tau_s}$ (Matin et al., 2021). We can plot $n_s = N_0 s^{-\tau_s}$ on log-log scaled plot to find a straight line with slope τ_s (Stauffer and Aharony, 2018; Matin et al., 2021). When the system is not at the critical point, there are deviations from the power law (Stanley, 1971; Stauffer and Aharony, 2018; Matin et al., 2021; Klein et al., 2007). We use the

Fisher ansatz (Fisher, 1967; Stauffer, 1979; Stauffer and Aharony, 2018), $G(x) = \exp(-x)$, which has been applied to the percolation (Stauffer and Aharony, 2018) and thermal systems (Klein et al., 2007). The exponential cutoff appears as a “knee” or “bend” in the log-log plot (Stauffer and Aharony, 2018; Matin et al., 2021; Matin et al., 2020). Distributions with a cut-off at some characteristic value are not scale-invariant (Stanley, 1999; Matin et al., 2021; Stauffer, 1979; Stauffer and Aharony, 2018; Stumpf and Porter, 2012).

We use scaling arguments to relate the power laws near the critical point. The characteristic size s_c can be related to the correlation length ξ , which diverges as

$$\xi \sim h^{-\nu} \implies \xi^{-\frac{1}{\nu}} \sim h. \quad (3.2)$$

The characteristic size scales as

$$s_c \sim h^{-1/\sigma_s} \sim \left[\xi^{-\frac{1}{\nu}} \right]^{-1/\sigma_s} \sim \xi^{1/(\sigma_s \nu)}. \quad (3.3)$$

We will use similar scaling arguments to derive new scaling laws for the OFC model. Although, the Fisher-Stauffer scaling techniques originated as an equilibrium method (Stauffer, 1979; Stauffer and Aharony, 2018; Fisher, 1967), they appear to be valid in the OFC model when the noise is greater than η_E (Matin et al., 2020).

3.4 Scaling when $\eta > \eta_E$

We use the generalized Fisher-Stauffer scaling theory to analyze avalanches in the two-dimensional OFC model with nearest neighbor connections and open boundary conditions as the dissipation goes to zero, $\lambda \rightarrow 0$ for $\eta > \eta_E$. We find that the scaling of the avalanches can be related to the critical point at $\lambda = 0$. In this section, we consider the OFC model when $\eta = 0.15 > \eta_E$, where $\eta_E = 0.071 \pm 0.02$ (Matin et al., 2020).

3.4.1 Scale Invariant Avalanche Distribution at the Critical point

We analyze the avalanche size s , area a and lifetime l near the critical point. As $\lambda \rightarrow 0$, the distribution of avalanche size s , area a and lifetime l are characterized by the following scaling forms

$$n_u \sim u^{-\tau_u} \exp\left(-\frac{u}{u_c}\right) \quad \text{for } u = s, a, \ell, \quad (3.4)$$

where, s_c , a_c and ℓ_c are the characteristic size, area and lifetime respectively. Note that Eq. (3.4) corresponds to the Fisher-Stauffer scaling form (Stauffer and Aharony, 2018). When the system approaches the critical point $\lambda \rightarrow 0$ the characteristic values scale as

$$u_c \sim \lambda^{-1/\sigma_u} \quad \text{for } u = s, a, \ell. \quad (3.5)$$

Figure. 3-1 shows that the avalanche distributions for size, area and lifetime follow power laws only at the critical point. The critical exponents, which characterizes the power laws, are estimated to be $\tau_s = 1.26 \pm 0.02$, $\tau_a = 1.23 \pm 0.02$ and $\tau_\ell = 1.37 \pm 0.06$. For finite dissipation, the cutoffs are observed at the smaller values of the size, area and lifetimes when $\eta > \eta_E$. The exponential cutoffs correspond to characteristic size, area and lifetimes which diverge with the critical exponents $\sigma_s = 0.75 \pm 0.04$, $\sigma_a = 0.97 \pm 0.07$ and $\sigma_\ell = 1.39 \pm 0.06$ as $\lambda \rightarrow 0$, as seen in Fig. 3-2.

Universal scaling functions are a remarkable property of systems near a critical point and are obtained via data collapse where curves for different values of the tuning parameter collapse onto a single line after appropriate rescaling (Stanley, 1971; Stauffer and Aharony, 2018; Sethna et al., 2001; Matin et al., 2021). We start with the distribution functions, and using Eq. (3.5) we write

$$n_u \sim u^{-\tau_u} \exp\left(-\frac{u}{u_c}\right) \sim u^{-\tau_u} \exp(-u\lambda^{1/\sigma_u}). \quad (3.6)$$

We multiply both sides of the equation with $\lambda^{-\frac{\tau_u}{\sigma_u}}$ to find

$$n_u \lambda^{-\frac{\tau_u}{\sigma_u}} \sim \lambda^{-\frac{\tau_u}{\sigma_u}} \exp(-u \lambda^{1/\sigma_u}), \quad (3.7)$$

$$n_u \lambda^{-\frac{\tau_u}{\sigma_u}} \sim [u \lambda^{1/\sigma_u}]^{-\tau_u} \exp(-u \lambda^{1/\sigma_u}) \quad \text{for } u = s, a, \ell. \quad (3.8)$$

The rescaled variables are $n_u \lambda^{-\tau_u/\sigma_u}$ and $u \lambda^{1/\sigma_u}$. In the inset of Fig. 3-1, we observe data collapse when we plot the rescaled variables for the avalanche size, area and lifetime distributions. Data collapse of the avalanche distribution is strong evidence that the relevant scaling field is a function of the dissipation λ in the OFC model when $\eta > \eta_E$.

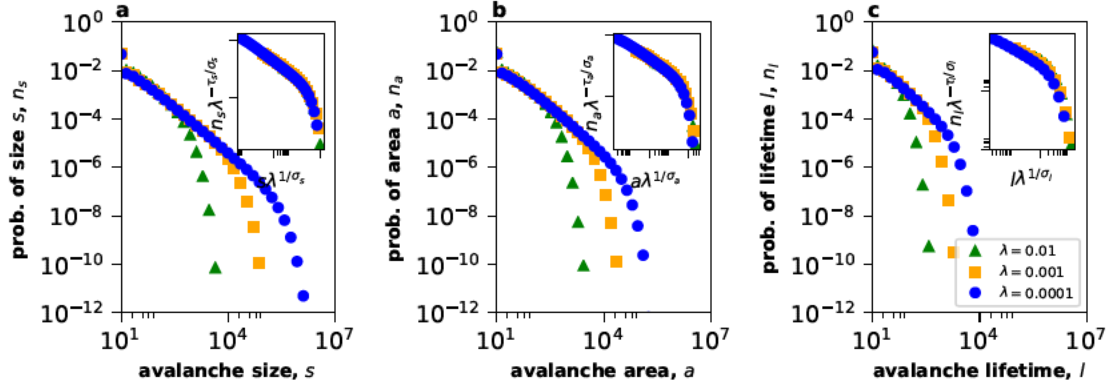


Figure 3-1: The distribution of avalanche size s , area a and lifetime l is a power law at only at the critical point at $\lambda = 0$. Large avalanches are exponentially suppressed for finite dissipation $\lambda > 0$. The measured exponents are $\tau_s = 1.26 \pm 0.02$, $\tau_a = 1.23 \pm 0.02$ and $\tau_\ell = 1.37 \pm 0.06$. Insets show data collapse when we plot in terms of the rescaled variables $n_u \left[\lambda^{-\frac{\tau_u}{\sigma_u}} \right] \sim [u \lambda^{1/\sigma_u}]^{-\tau_u} \exp(-u \lambda^{1/\sigma_u})$ for $u = s, a, \ell$ respectively.

3.4.2 Finite Size Scaling

Critical points are associated with singularities in thermodynamic functions, which are only observed for infinite system size or in the thermodynamic limit (Stanley,

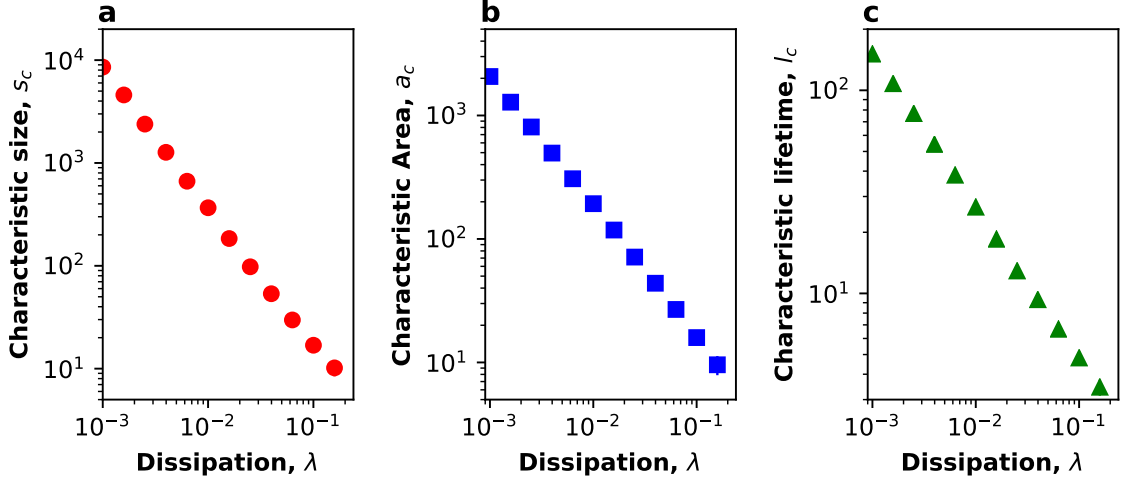


Figure 3.2: The characteristic size s_c , area a_c and lifetime ℓ_c diverges as the the critical point is approached $\lambda \rightarrow 0$. The s_c , a_c and ℓ_c are found by fitting the avalanche distributions using Eq. (3.4). The numerical estimates of the critical exponents are $\sigma_s = 0.75 \pm 0.03$, $\sigma_a = 0.97 \pm 0.07$ and $\sigma_\ell = 1.39 \pm 0.06$.

1971; Stauffer and Aharony, 2018). Unfortunately, simulations can be performed at finite system lengths, which sets a cut-off for the avalanche distributions (Stanley, 1971; Stauffer and Aharony, 2018). Finite size scaling seeks to exploit this apparent limitation by systematically studying how the cut-off (set by the lattice size) scales with the system length L (Stanley, 1971; Stauffer and Aharony, 2018).

In Eq. (3.3), we showed that the characteristic size scales as $s_c \sim \xi^{1/(\sigma_s \nu)}$. We can extend this scaling to the avalanche area and lifetime as well,

$$u_c \sim \xi^{1/(\sigma_u \nu)}, \quad \text{for } u = s, a, \ell. \quad (3.9)$$

At the critical point the correlation diverges and the scaling in Eq. (3.9) is valid up to the system length, and the scaling relation becomes

$$u_c \sim L^{1/(\sigma_u \nu)} \quad \text{for } u = s, a, \ell. \quad (3.10)$$

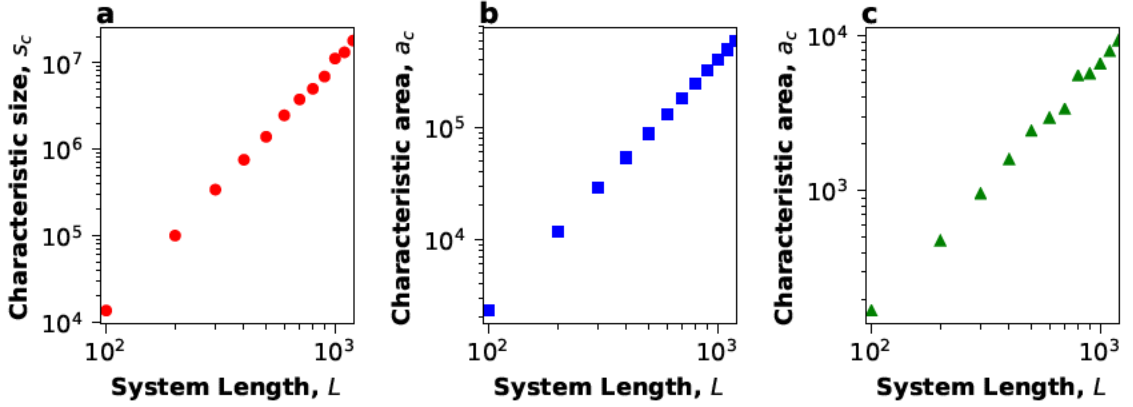


Figure 3-3: The characteristic size s_c , area a_c and lifetime ℓ_c diverges with the system length L at the critical point. For $\lambda = 0$, $u_c \sim L^{1/(\sigma_u \nu)}$ for $u = s, a, \ell$.

The dynamic exponent z characterizes how the characteristic time scales with the correlation length (Hohenberg and Halperin, 1977a), $\ell_c \sim L^z$. By using similar scaling arguments, we can rewrite the dynamic exponent as

$$z = \frac{1}{\sigma_\ell \nu}. \quad (3.11)$$

Using the estimates of the critical exponents in Fig. 3-2 and 3-3, we can estimate $\nu = 0.53 \pm 0.09$.

The fractal dimension can be expressed as

$$d_f = \frac{1}{\sigma_a \nu}. \quad (3.12)$$

We find that our estimate of the fractal dimension is consistent with the spatial dimension $d = 2$. Additionally, the Hausdorff dimension is $d_H = 2$ because the spatial distribution of the avalanches are compact. The fractal dimension and the Hausdorff dimension are equal to the spatial dimension for the the 2D OFC model for $\eta > \eta_E$.

We derive the rescaled variables for data collapse of the avalanche distribution

functions as L is varied. We start with the avalanche distribution function and use Eq. (3.10) to write

$$n_u \sim u^{-\tau_u} G(-u/u_c) \sim u^{-\tau_u} \exp(-uL^{-1/(\sigma_u\nu)}). \quad (3.13)$$

We multiply both sides with $L^{\tau_u/(\sigma_u\nu)}$ to find

$$L^{\tau_u/(\sigma_u\nu)} n_u \sim [L^{-1/(\sigma_u\nu)} s]^{-\tau_u} \exp[-uL^{-1/(\sigma_u\nu)}] \quad \text{for } u = s, a, \ell. \quad (3.14)$$

Our rescaled variables are $L^{\tau_u/(\sigma_u\nu)} n_u$ and $uL^{-1/(\sigma_u\nu)}$. In Fig. 3-4 we plot the avalanche distribution for size, area and lifetime at the critical point $\lambda = 0$ for different values of the system length L . The finite-size cut-off shifts to larger values as L increases. In the inset of Fig. 3-4, we observe data collapse when we plot the rescaled variables in Eq. (3.14). This result indicates that the OFC model is consistent with finite size scaling when $\eta > \eta_E$.

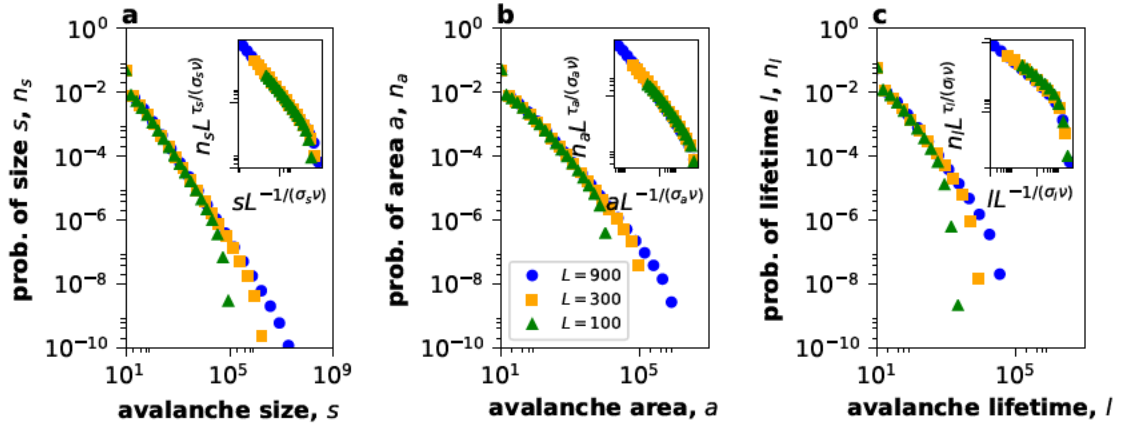


Figure 3-4: The distributions for avalanche size, area and lifetime are consistent with finite size scaling. Data collapse in the inset when the rescaled variables in Eq. (3.14) are plotted.

3.4.3 Response Function

Divergent response functions are hallmarks of systems near the critical point (Stanley, 1971; Stanley, 1999). Response functions quantify how changes in intensive parameters lead to changes in macroscopic quantities (Stanley, 1971; Stauffer and Aharony, 2018). We use the response function for the avalanche size, area and lifetimes,

$$\chi_u = \frac{\sum_u u^2 n_u}{\sum_u u n_u}, \quad \text{for } u = s, a, \ell. \quad (3.15)$$

obtained from percolation theory (Stauffer, 1979; Stauffer and Aharony, 2018; Stanley, 1971). The response functions are analogous to the magnetic susceptibility in the Ising model (Stanley, 1971; Stauffer and Aharony, 2018). The response functions diverge as dissipation approaches zero,

$$\chi_s \sim \lambda^{-\gamma_s} \quad \text{for } u = s, a, \ell. \quad (3.16)$$

In Fig. 3-5, we estimate the critical exponent for the response function to be $\gamma_s = 1.26 \pm 0.04$, $\gamma_a = 1.02 \pm 0.06$, and $\gamma_\ell = 0.69 \pm 0.02$.

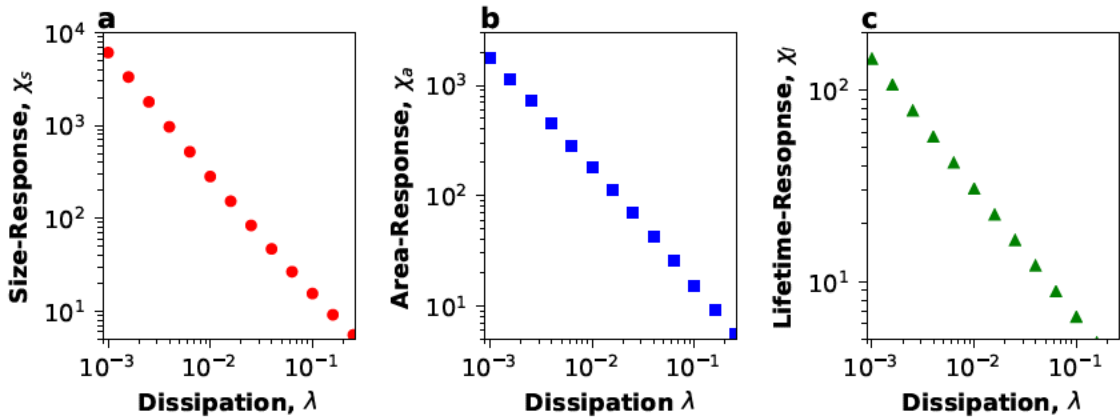


Figure 3-5: The response functions for avalanche size, area and lifetime, defined in Eq. (3.15), diverge as the critical point is approached. The estimated critical exponents are $\gamma_s = 1.26 \pm 0.04$, $\gamma_a = 1.02 \pm 0.06$, and $\gamma_\ell = 0.69 \pm 0.02$.

We show that the divergent response functions are consistent with finite size scaling. By using similar scaling arguments as in Section 3.4.2, we show that the response functions scale as

$$\chi_u \sim L^{\gamma_u/\nu} \text{ for } u = s, a, l. \quad (3.17)$$

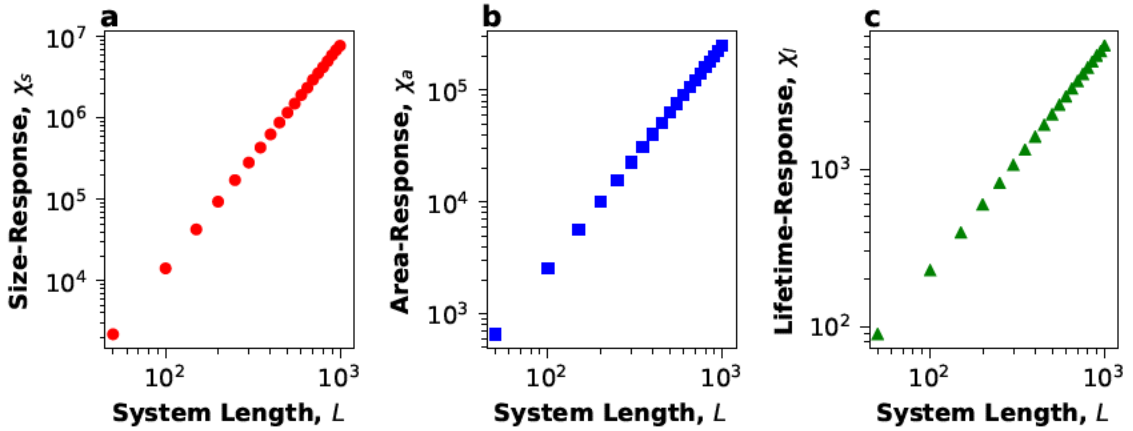


Figure 3-6: The response functions diverges with the system length L at the critical point. For $\lambda = 0$, $\chi \sim L^{\gamma_u/\nu}$ for $u = s, a, l$.

3.5 Order parameter

Critical points in thermodynamic systems can be characterized by an order parameter that is finite in the ordered state and zero in the disordered phase (Stanley, 1971). In the Ising model the magnetization per site is the order parameter, which is nonzero below the critical temperature when there is no external magnetic field (Stanley, 1971). The order parameter for percolation is the the fraction of sites that are part of the spanning cluster (Stauffer and Aharony, 2018). Below the percolating threshold(disordered phase in thermodynamic terms), there is no spanning cluster and the order parameter is zero (Stauffer and Aharony, 2018).

We have shown that the $\lambda = 0$ is the critical point for the OFC model. When

$\lambda > 0$, the OFC model is in the disordered phase where all the avalanches are finite. For $\lambda < 0$, the system appears to be in the ordered phase, characterized by infinite avalanches in the thermodynamic limit.

Our choice of the order parameter for the OFC model is motivated by work in percolation (Stauffer, 1979; Stauffer and Aharony, 2018) and directed percolation (Henkel et al., 2008). We choose as our order parameter the fraction of avalanches that are spanning $\mathcal{P}_{\text{span}}$. A spanning avalanche is when there is at least one firing site along each of the four edges in the lattice. The order parameter scales as

$$\mathcal{P}_{\text{span}} \sim \lambda^\beta, \text{ for } \lambda < 0. \quad (3.18)$$

By using finite size scaling arguments and Eq. (3.9), we show that the order parameter scales with the system size as

$$\mathcal{P}_{\text{span}} \sim L^{-\frac{\beta}{\nu}}. \quad (3.19)$$

Our numerical estimates indicate that $\frac{\beta}{\nu} \approx 0$, i.e. $\beta \approx 0$ as $\nu > 0$ in our prior estimates. The scaling law relating the order parameter exponent to the response functions $\beta + \gamma_u = \frac{1}{\sigma_u}$ (Stanley, 1971) is consistent with our numerical estimate of γ_u in Fig. 3.5 and σ_u in Fig. 3.2.

3.5.1 Scaling Laws

Near the critical point, the response function can be described by a generalized homogeneous function (Stanley, 1971; Stauffer and Aharony, 2018; Matin et al., 2021; Hankey and Stanley, 1972). We drop the subscripts on the critical exponents for the following derivation to improve readability. For $u \gg 1$, the response functions can be

written as

$$\chi_u = \frac{\sum_{u \geq 1} u^2 n_s}{\sum_{u \geq 0} u n_u} \approx \frac{\int_1^\infty u^{2-\tau} G(u/u_c) du}{\int_1^\infty u^{1-\tau} G(u/u_c) du}. \quad (3.20)$$

We use the Fisher ansatz $G(u) = \exp(-u)$ and the change of variables $y = u/u_c$ to find

$$\chi \approx \frac{u_c^{3-\tau} \int_{1/u_c}^\infty y^{2-\tau} \exp(-y) dy}{u_c^{2-\tau} \int_{1/u_c}^\infty y^{1-\tau} \exp(-y) dy}, \quad (3.21)$$

In the limit, $\lambda \rightarrow 0$, the characteristic values u_c diverges. When evaluating the first and second moment, the argument of the exponential can be taken to be zero between up to $\lambda s^\sigma \sim 1$ (Stauffer and Aharony, 2018), so the integrals can be replaced by the gamma functions Γ (Arfken and Weber, 1999),

$$\approx u_c \frac{\Gamma(3-\tau)}{\Gamma(2-\tau)}, \text{ as } \lambda \rightarrow 0. \quad (3.22)$$

The response function for the avalanche size, area and lifetime scales as

$$\chi_s \sim u_c \text{ for } u = s, a, \ell. \quad (3.23)$$

By using Eq. (3.5) and Eq. (3.23), we find the scaling laws

$$\gamma_u = \frac{1}{\sigma_u} \text{ for } u = s, a, \ell. \quad (3.24)$$

The estimated critical exponents in Fig. 3.2 and Fig. 3.5 show that the OFC model is consistent with the derived scaling in Eq.(3.24) law when $\eta > \eta_E$. Our derivation is similar to percolation theory (Stauffer and Aharony, 2018; Chen and Lin, 2009), except that for the OFC model the first moment of the avalanche distributions also contribute to the divergence.

3.5.2 Gap Exponent

Systems near the critical point are characterized by an emergent scale which is parameterized by a fractal dimension (Stanley, 1971). The existence of a single fractal dimension implies a constant gap exponent (Stauffer and Aharony, 2018; Stanley, 1971; Kadanoff et al., 1989), which characterizes how the ratio of the moments of the avalanche distribution functions,

$$R_u(k) = \frac{\sum_u u^{k+1} n_u}{\sum_u u^k n_u} \quad \text{for } u = s, a, \ell, \quad (3.25)$$

diverges for $k \geq 1$. Near the critical point, we can write $R_u(k)$ as

$$R_u(k) = \frac{\int_1^\infty u^{k+1-\tau_u} \exp(-u) du}{\int_1^\infty u^{k-\tau_u} \exp(-u) du} \quad (3.26)$$

By using similar scaling arguments as in Sec. 3.5.1, we show that $R_u(k)$ scales

$$R_u(k) \sim \lambda^{-1/\sigma_u} \quad \text{for } u = s, a, \ell. \quad (3.27)$$

In Fig. 3-7, we see that there are constant constant gap exponents for avalanche size, area and lifetime distributions as $\lambda \rightarrow 0$ for $\eta > \eta_E$.

3.5.3 Conditional distribution function relating avalanche size, area and lifetime

We can use conditional distribution functions, $S(a)$, $A(\ell)$ and $S(\ell)$, to relate the avalanche size, area and lifetime. $S(a)$ is the expected size for avalanche of area a , $A(\ell)$ is the expected area for an avalanche of lifetime ℓ , and $S(\ell)$ is the expected size for an avalanche of lifetime ℓ . $S(a)$, $A(\ell)$ and $S(\ell)$ can be written as a generalized homogeneous function near the critical point (Stanley, 1971; Hankey and Stanley, 1972; Martin et al., 2021). Uni-variate generalized homogeneous functions are power laws (Stanley, 1971; Hankey and Stanley, 1972). The conditional distribution func-

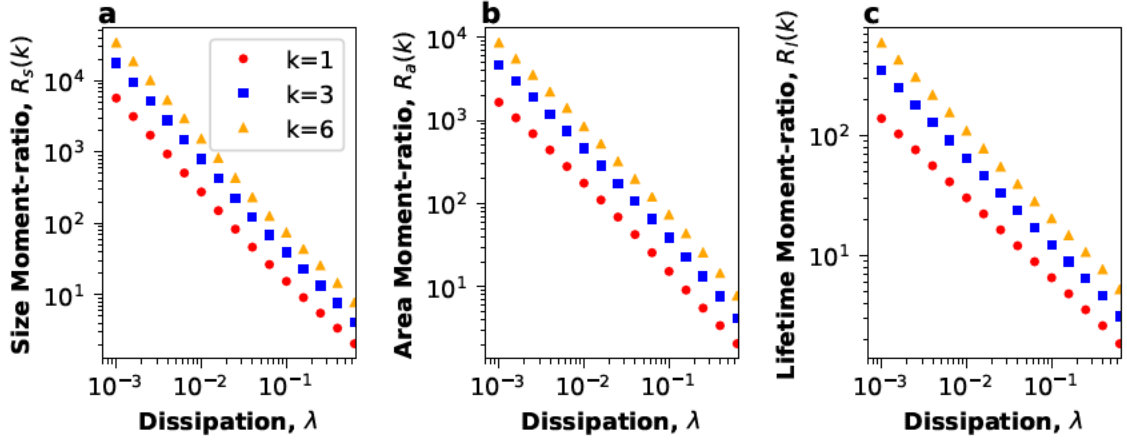


Figure 3.7: The distribution functions for avalanche size, area and lifetime are characterized by constant gap exponents as $\lambda \rightarrow 0$ for $\eta > \eta_E$. $R_u(k)$, defined in Eq. (3.26), diverges with as power laws $R_u(k) \sim \lambda^{-\frac{1}{\sigma_u}}$.

tions near the critical point are

$$S(a) \sim a^\zeta, \quad (3.28)$$

$$A(\ell) \sim \ell^\mu, \quad (3.29)$$

$$S(\ell) \sim \ell^\kappa. \quad (3.30)$$

In Fig. 3.8, we estimate the exponents ζ , κ and μ to be $\zeta = 1.38 \pm 0.07$, $\kappa = 1.35 \pm 0.07$ and $\mu = 1.77 \pm 0.07$.

We derive scaling laws which relate exponents ζ , κ and μ to the Fisher exponents σ_u . The first moment of conditional distribution functions scales with the characteristic values,

$$\overline{S(a)} \sim s_c, \quad (3.31)$$

near the critical point (Matin et al., 2021; Sethna et al., 2001). By using Eq. (3.9)

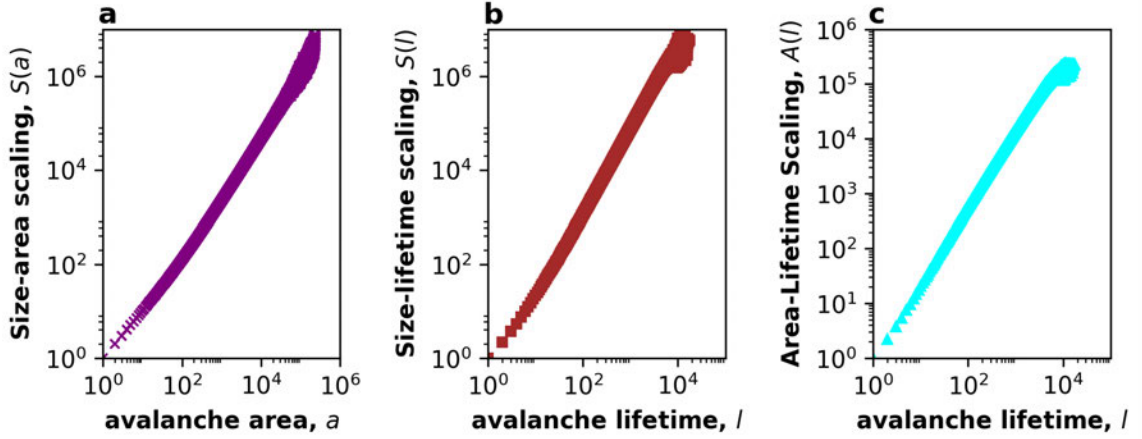


Figure 3-8: The conditional distribution functions relating avalanche size, area and lifetimes are power laws at the critical point. The size-area conditional distribution function scales as $S(a) \sim a^\zeta$, where $\zeta = 1.38 \pm 0.07$. The size-lifetime conditional distribution function scales as $S(\ell) \sim \ell^\kappa$, where $\kappa = 1.35 \pm 0.07$. The area-lifetime conditional distribution function scales as $A(\ell) \sim \ell^\mu$, where $\mu = 1.77 \pm 0.07$.

we can write

$$\overline{S(a)} \sim s_c, \quad (3.32)$$

$$\sim \xi^{1/(\sigma_s \nu)}, \quad (3.33)$$

$$\sim a_c^{(\sigma_a \nu)/(\sigma_s \nu)}, \quad (3.34)$$

$$\sim a^{\sigma_a/\sigma_s}. \quad (3.35)$$

By using similar arguments, we can derive similar relations for $S(\ell)$ and $A(\ell)$, which are

$$S(\ell) \sim \ell^{\sigma_\ell/\sigma_s}, \quad (3.36)$$

$$A(\ell) \sim \ell^{\sigma_\ell/\sigma_a}. \quad (3.37)$$

We obtain the following scaling identities

$$\zeta = \frac{\sigma_a}{\sigma_\ell}, \quad (3.38)$$

$$\mu = \frac{\sigma_\ell}{\sigma_a}, \quad (3.39)$$

$$\kappa = \frac{\sigma_\ell}{\sigma_s}, \quad (3.40)$$

which are consistent with the numerical estimates from Figs. 3·1, 3·2, and 3·8.

3.5.4 Universal Firing Rates

The avalanches dynamics in the OFC model are described by a universal scaling function when $\eta > \eta_E$ at the critical point (Matin et al., 2021; Sethna et al., 2001; Fontenele et al., 2019a). $F(t, \ell)$ is the mean firing rate at time t for avalanches of lifetime ℓ . For $\lambda = 0$, the firing rate can be described by a multivariate generalized homogeneous function (Matin et al., 2021; Sethna et al., 2001),

$$F(t, \ell) = \phi^{-b} V(\phi t, \phi \ell), \quad (3.41)$$

where ϕ is an arbitrary constant. We set $\phi = 1/\ell$ to find

$$F(t, \ell) = \ell^b F(t/\ell, 1). \quad (3.42)$$

The right side of Eq. 3.42 is only a function of the ratio t/ℓ , therefore we can introduce an appropriate uni-variate function,

$$F(t, \ell) = \ell^b f(t/\ell). \quad (3.43)$$

We express b in terms of the other critical exponents. The average avalanche size

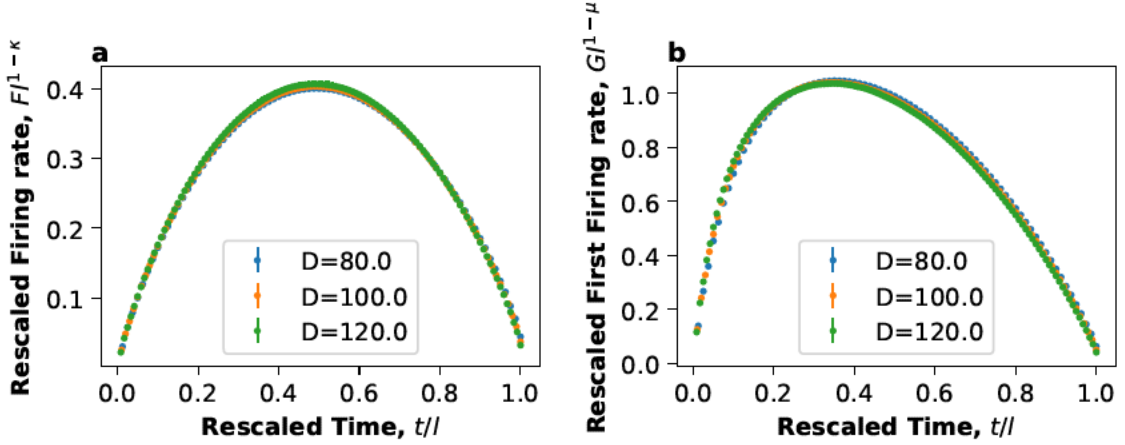


Figure 3-9: The OFC model exhibits universal avalanche profiles at the critical point when $\eta > \eta_E$. The rescaled firing rate $F l^{1-\kappa}$ and rescaled first firing rate $G l^{1-\mu}$ as a function of the rescaled time t/l show data collapse in Panels a and b respectively.

for lifetime ℓ is the integral of the firing rate,

$$S(\ell) = \int_0^{\ell} F(t, \ell) dt, \quad (3.44)$$

$$= \int_0^{\ell} \ell^b f(t/\ell) dt. \quad (3.45)$$

We introduce the change of variables $y = t/\ell$ to find

$$\ell^\kappa \sim \int_0^1 \ell^{b+1} v(y) dy, \quad (3.46)$$

$$\sim \ell^{b+1}. \quad (3.47)$$

Therefore $b = \kappa - 1$. Figure 3-9(a) shows data collapse when we plot the rescaled firing rate $F(t, \ell) \ell^{\kappa-1}$ against t/ℓ .

$G(t, \ell)$ is the first firing rate, which is number of sites which fire for the first time during an avalanche. By using similar scaling arguments, we find data collapse for

the first firing rates when we plot the rescaled variables $G(t, \ell)\ell^{\mu-1}$ as a function of the rescaled time t/ℓ in Fig 3·9(b).

The existence of universal scaling functions for the dynamics of the avalanches are a strict criteria for criticality and can be observed only sufficiently close to the critical point (Matin et al., 2021; Fontenele et al., 2019a; Sethna et al., 2001).

3.6 Scaling in the deterministic OFC model

We analyze the avalanche distributions for the deterministic ($\eta = 0$) OFC model and show that the scaling behavior is in stark contrast to the $\eta > \eta_E$ case. The deterministic OFC model is characterized by very long transients (Middleton and Tang, 1995; Wissel and Drossel, 2006; Grassberger, 1994). For all the deterministic runs reported here, we first run the system until the transient has ended. The deterministic OFC model exhibits partially synchronized stress domains, which appear as patches of identical on-site stress when we plot a snapshot of the system (Middleton and Tang, 1995; Lise and Paczuski, 2001b; Lise and Jensen, 1996). These domains originate at the edges of the lattice and slowly invade the bulk toward the center (Middleton and Tang, 1995; Lise and Paczuski, 2001b; Wissel and Drossel, 2006; Drossel, 2002). The transient time is defined as the time taken for the invasion to reach the center of the lattice (Middleton and Tang, 1995; Lise and Paczuski, 2001b; Ceva, 1998; Wissel and Drossel, 2006).

3.6.1 Generic Scale Invariant Avalanche Distribution

The avalanche size distribution exhibits generic scale invariance (power-law distributed avalanches for a range of λ values) in the deterministic OFC model. Figure 3·10 shows that the exponent τ_s which characterizes the power-law and varies with the dissipation λ , in contrast to the Fisher-Stauffer scaling form. This is consistent with results in Refs. (Olami et al., 1992; Olami and Christensen, 1992; Christensen and Olami,

1992; Boulter and Miller, 2003; Christensen et al., 1992; Middleton and Tang, 1995) We find that the avalanche area distribution also exhibits generic scale invariance and the exponent τ_a also depends on the dissipation. However, we find that the avalanche lifetime distribution cannot be fit to power laws for all values of λ .

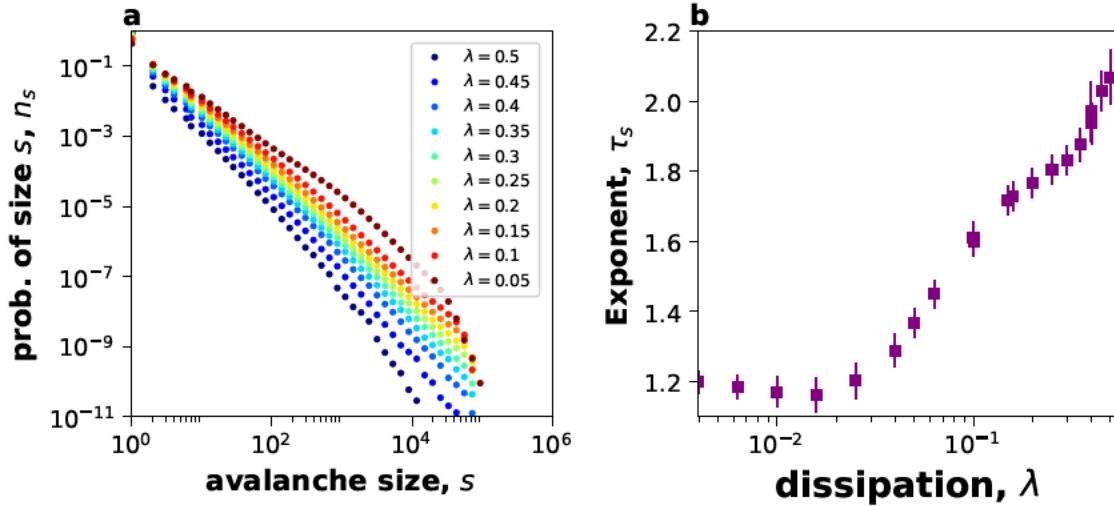


Figure 3-10: The avalanche size distribution exhibits generic scale invariance in the deterministic OFC model. The exponent τ_s characterizes the avalanche size distribution and is non-monotonic as a function of the dissipation λ in the OFC model when $\eta = 0$, in contrast to the Fisher-Stauffer scaling forms observed when $\eta > \eta_E$.

3.6.2 Multifractal distribution

Our results indicate that the deterministic OFC model is consistent with multifractal scaling, which is characterized by a nonuniform gap exponent (Stauffer and Aharony, 2018; Kadanoff et al., 1989; Tebaldi et al., 1999; Tél, 1988). Systems with multifractal scaling are characterized by a spectrum of exponents, known as the singularity spectrum (Kadanoff et al., 1989; Tebaldi et al., 1999). Figure 3-11 shows that the moment ratio Functions $R_u(k)$ for avalanche size, area and lifetime are not characterized by a constant gap exponent when $\eta = 0$. We also analyze $R_u(k)$ as a function

the system length L for $\lambda = 0$ to find that that the deterministic OFC model is not consistent with finite size scaling.

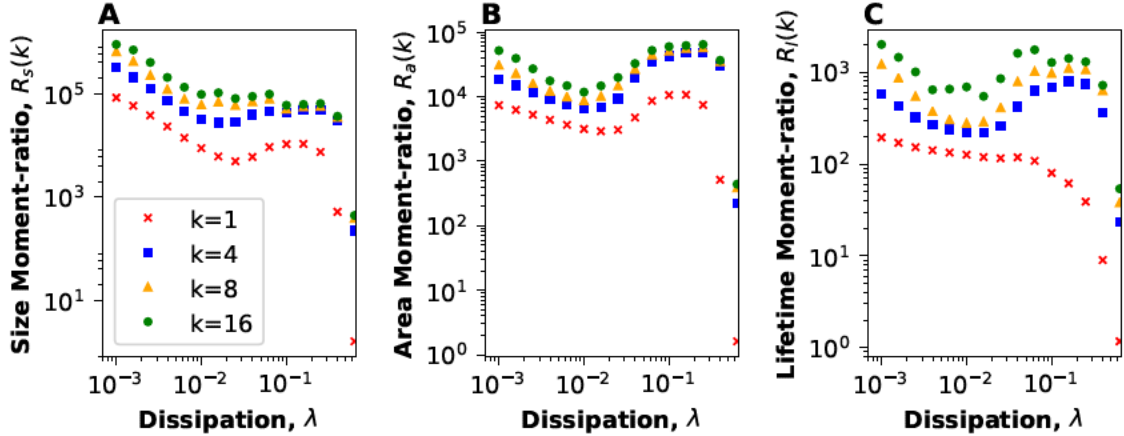


Figure 3-11: The distribution functions for avalanche size, area and lifetime are not characterized by constant gap exponents in the deterministic OFC model. $R_u(k)$, defined in Eq. 3.26, does not diverge as power laws when $\lambda \rightarrow 0$ for $\eta = 0$. The rate of divergence of $R_u(k)$ depends on k .

Multifractal scaling implies there are multiple divergent length scales which contribute to the scaling behavior of the avalanches. This is in contrast to equilibrium thermodynamic systems (Stanley, 1971) and percolation models (Stauffer and Aharony, 2018).

3.7 Discussion

We find strikingly different scaling phenomena in the two-dimensional OFC model as $\lambda \rightarrow 0$ for $\eta = 0$ and $\eta > \eta_E$. The scale invariant behavior can be attributed to an underlying critical point at $\lambda = 0$ for $\eta > \eta_E$. We have derived universal scaling functions for the avalanche statistics and dynamics. The critical exponents which characterize the scale invariant phenomena are shown to be consistent with our derived scaling laws. Our results strongly indicate the OFC model is not consistent

with self-organized criticality for $\eta > \eta_E$ and that the relevant scaling field is a function of λ . On the other hand, the deterministic OFC model exhibits generic scale invariance for a large range of dissipation values. A continuous spectrum of τ_s and τ_a exponents parameterize the avalanche distribution functions, which are consistent with multifractal scaling. Refs. (Olami et al., 1992; Olami and Christensen, 1992; Christensen and Olami, 1992; Boultter and Miller, 2003; Christensen et al., 1992; Middleton and Tang, 1995) have interpreted this behavior as an example self-organized criticality for finite dissipation. Additionally, our work sheds light on the unusual scaling behavior of systems with multifractal scaling and supports the idea that there may be an important connection to self-organized criticality (Kadanoff et al., 1989; Tebaldi et al., 1999; Olami and Christensen, 1992; Stella and De Menech, 2001).

Our finding that the relevant scaling field in the OFC model for $\eta > \eta_E$ is a function of the bulk dissipation rate has important implications for the BTW sandpile model (Bak et al., 1987) and the Manna model (Manna, 1991) which have been argued to be examples of self-organized criticality. An important question is whether certain systems exhibit apparent SOC behavior because the relevant scaling field in the problem is simply tuned to the critical value in the model definition. Additionally, we hypothesize that the multifractal scaling in the BTW sandpile (Kadanoff et al., 1989; Tebaldi et al., 1999) and the finite size scaling in the Manna (Manna, 1991; Chen and Lin, 2009) may be due to the fact that the avalanche dynamics in the BTW model are deterministic (Bak et al., 1987), and the Manna model has stochastic dynamics (Manna, 1991).

The characterization of the scaling behavior of avalanches in the OFC model may also be of interest in other fields such as neuroscience (Matin et al., 2021; Muñoz, 2018a; Fontenele et al., 2019a; Friedman et al., 2012; Friedman et al., 2012). The OFC model is the slow-driving limit of an integrate and fire system, which models

neural systems (Hopfield and Herz, 1995; Herz and Hopfield, 1995; Millman et al., 2010b; Martinello et al., 2017). The role of scale invariant neural avalanches *in vivo* and *in vitro* in brain function are an open question (Martinello et al., 2017; Fontenele et al., 2019a; Muñoz, 2018a; Friedman et al., 2012; Beggs and Plenz, 2003; Matin et al., 2021). The generalized Fisher-Stauffer scaling theory may a useful tool to analyze neural avalanches in simulations (Matin et al., 2021; Millman et al., 2010b; Martinello et al., 2017) and experiments (Zierenberg et al., 2018a; Friedman et al., 2012; Fontenele et al., 2019a; Beggs and Plenz, 2003).

Chapter 4

Stability of Foreshocks and Aftershocks in the Long-Range Olami-Feder-Christen model

4.1 Introduction

Earthquake fault systems are characterized by spatial inhomogenities across many scales (Rundle et al., 2021). These spatial inhomogenities are affected by short term properties such as water content in rocks (Vasarhelyi and Ván, 2006) and the long term geological activity of the fault itself (Rundle et al., 2021; Kazemian et al., 2015). The role of spatial inhomogenities in temporal dynamics of earthquakes is not well understood (Kazemian et al., 2015).

To obtain a deeper understanding of earthquake phenomenology, investigators have studied simple models such as the OFC model (Olami et al., 1992; Serino et al., 2011; Hergarten and Neugebauer, 2002; Kazemian et al., 2015; Dominguez et al., 2013). Early works (Olami et al., 1992; Hergarten and Neugebauer, 2002) focused on the OFC model with nearest-neighbor stress transfer to study the distribution of earthquakes (or avalanches). These studies qualitatively captured the Gutenberg-Richter law (Wesnousky, 1994; Olami et al., 1992), which describes the magnitude frequency distribution of earthquakes. Reference. (Hergarten and Neugebauer, 2002) showed that the deterministic OFC model with nearest-neighbor stress transfer is qualitatively consistent with Omori's Law (Davidsen et al., 2015), which characterizes

the distribution of foreshocks and aftershocks preceding and following a main shock.

Real earthquake fault systems have long-range elastic stress transfer (Rundle and Klein, 1993; Klein et al., 1997; Serino et al., 2011). Reference (Serino et al., 2011) studied the OFC model with long-range stress transfer to model earthquake fault systems. Aggregate statistics from different fault systems are consistent with the Gutenberg-Richter scaling law, even though single earthquake faults generally are not consistent with the Gutenberg-Richter scaling law (Serino et al., 2011). Reference (Serino et al., 2011) showed that long-range OFC models with different levels of spatial disorder can lead to quantitative agreement with the Gutenberg-Richter scaling similar to real earthquake fault systems. Additionally, the scaling distribution was shown to be related to an underlying spinodal critical point (Serino et al., 2011).

Certain earthquake fault systems exhibit temporal regularity on both short time scales (Davidsen et al., 2015) and long time scales (Veedu and Barbot, 2016). One of the most well known examples is the Parkfield fault system where a magnitude 6 or greater earthquake has occurred roughly every 22 years since 1857 (Veedu and Barbot, 2016). The latest recorded earthquake in the Parkfield fault was in 2004 showed significant deviation from the historical trend (Bakun et al., 2005). To better understand the mechanisms behind earthquake periodicity, Ref. (Kazemian et al., 2015) studied the long-range OFC model and showed that spatial disorder such as asperities can lead to temporal clustering of earthquakes in the form of foreshocks and aftershocks. The simulation results using the OFC model were compared to similar clustering in the north Iceland, southern Eyjafjaröaráll graben fault systems between August 20, 2012 through March 25, 2013 (Kazemian et al., 2015), which also exhibited temporal clustering of earthquakes.

Our work builds on the study of foreshocks and aftershocks in the OFC model in Ref. (Kazemian et al., 2015). We analyze the long time stability of temporal clustering

of earthquakes and discuss the implications on forecasting.

4.2 Model

We study the two dimensional OFC model defined on a square lattice with stress-transfer range R and periodic boundary conditions. Each site can hold stress denoted by $V_{i,j}$. The system is initialized with all sites having stress randomly assigned between the residual stress $V^R = 1.0$ and the failure threshold $V^F = 2.0$. A fraction of the sites are asperities with a much higher failure threshold $V^F = 12.0$. The OFC model is driven uniformly until one site has stress equal to its failure threshold (V^F). When the stress on the site equals the failure threshold, it topples and is reset to $V^R + \eta r$, where r is a random uniform number between $[-1, 1]$ and η is the strength of the noise. The stress $(1 - \lambda) [V^F - (V^R + \eta r)]$ is distributed evenly to the all neighbors within an a distance R , where λ is the dissipation rate. The remaning stress is dissipated. The sites within in the stress transfer range receive stress from the firing site and may fire if the stress exceeds the failure threshold. We call this cascade of firings an earthquake in the OFC model. No stress is added when an earthquake is in progress. This large separation of timescales between the slow driving and fast relaxation is consistent with the fact that earthquakes occur at time scales much shorter than geological scales typically associated with fault systems (Serino et al., 2011). We record the size s of the earthquake (number of times sites fire).

4.3 Results

We find that Gutenberg-Richter scaling (power-law distribution characterizing the magnitude-frequency relation of earthquakes) can coexist even with foreshocks and aftershocks. In Fig. 4-1, the measured value of exponent τ is consistent with theoretical value of $3/2$ (Serino et al., 2011). We measured $n_s(s)$ by averaging over a set

of 10^6 earthquakes. The distribution was fit to $n_s \sim s^{-\tau} \exp(s/s_c)$, where s_c is the characteristic size.

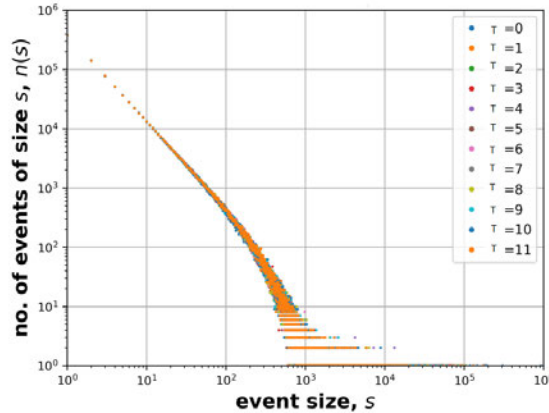


Figure 4.1: The two-dimensional OFC model with long-range stress transfer and asperities is consistent with Gutenberg Richter scaling in Ref. (Serino et al., 2011). After the system was initialized, the first $T \times 10^6$ events were discarded, and the distribution for the following 10^6 earthquakes is plotted. The distribution of event sizes follows a power-law with the exponent $\tau = 3/2$. The system size is $L = 300$ with stress transfer range $R = 10$, 5% of the sites are asperities with a failure threshold $V^A = 12.0$, and noise is $\eta = 0.10$. Our parameters values are similar to Ref. (Kazemian et al., 2015).

To study the non-stationary behavior in the OFC model, we analyzed different sequences of earthquakes. For a given sequence, we first discarded $T \times 10^6$ events after the system was initialized. Figure 4.2 shows the temporal clustering of earthquakes. Foreshocks precede a large earthquake called the main shock, which is followed by a series of aftershocks. The temporal clustering of earthquakes in the OFC model is non-stationary. Figure 4.2 shows that over time the temporal clustering becomes less pronounced. We repeated our analysis for different values of the noise η and system sizes. For higher noise, the temporal clustering disappears faster. Our finite size scaling analysis reveals that for large system sizes the temporal clustering decays at a much slower rate.

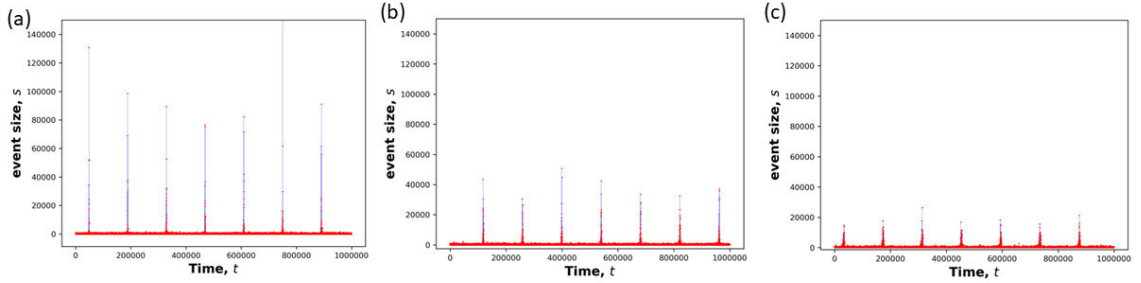


Figure 4.2: The long-range OFC model with asperities exhibits strong temporal clustering of events with foreshocks and aftershocks. The system size is $L = 300$, 5% of the sites are asperities with a failure threshold $V^A = 12.0$, and noise $\eta = 0.10$ is used. The different panels correspond to the time series of the earthquakes recorded after different transients since the initialization of the system. The transient in (a), (b) and (c) are 10^6 , 5×10^6 and 10^7 events respectively. The temporal clustering is non-stationary. The foreshocks and aftershocks becomes less pronounced over time.

Our analysis reveals that the foreshocks and aftershocks are due to collective firings of the asperity sites. Figure 4-3 shows that the weakening of the temporal clustering is accompanied by the smaller fraction of asperity sites failing during an event. Due to the presence of noise in the system, over time the asperities no longer fail collectively. Therefore, the foreshocks and aftershocks in the system becomes less pronounced.

4.4 Discussion

We showed that the temporal clustering of earthquakes in the long-range OFC model with asperities exhibit non-stationary behavior. In future works, we plan to use extend our to to model aging in earthquake fault systems (Rubin and Ampuero, 2005). Additionally, our work has important implications for the field of earthquake predictions (Rundle et al., 2021; Pun et al., 2020). The non-stationary behavior of earthquakes suggests that algorithms trained on a past data set may not be able to

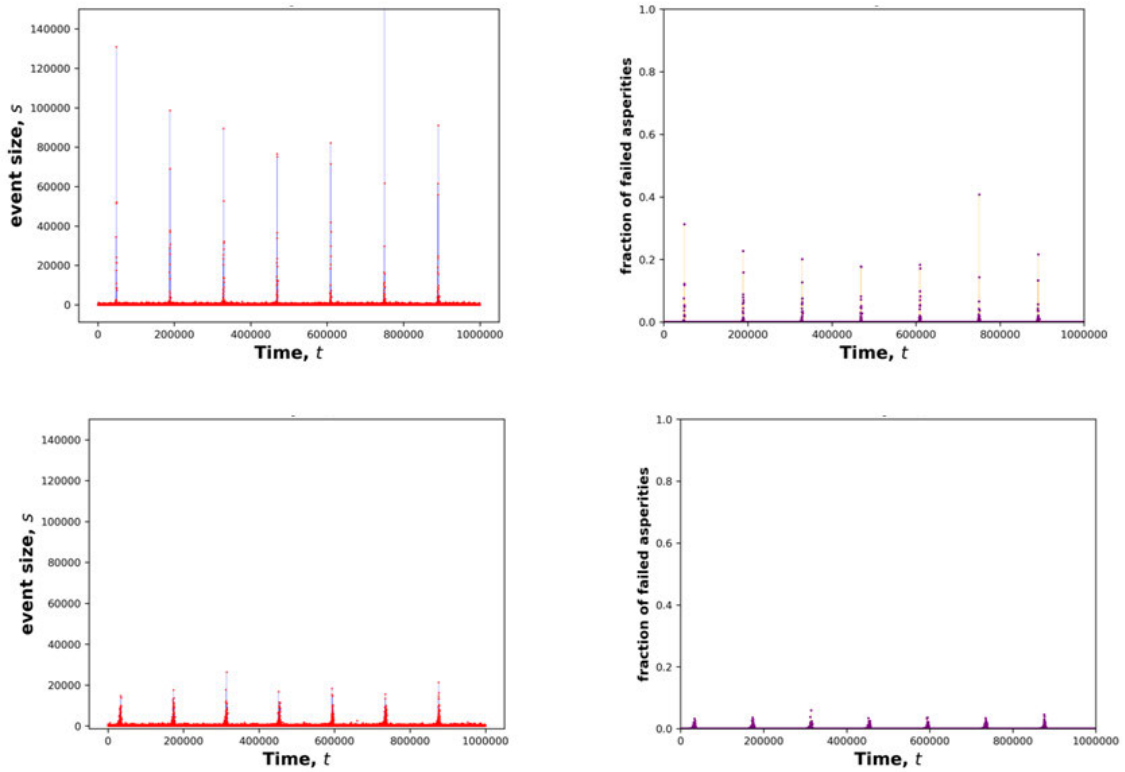


Figure 4.3: Weakening temporal clustering of earthquakes in the OFC model is due to desynchronization of the stress on the asperity sites. (a) and (b) correspond to a transient of 10^6 events. The sharp temporal clustering in (a) may be due to the large fraction of asperities that fail during the main shock as seen in (b). (c) and (d) correspond a transient of 10^7 events. (c) shows weaker temporal clustering compared to (a).

correctly predict future events. Therefore, methods that use spatial information for prediction (Pun et al., 2020) may prove useful for short-time earthquake forecasting.

Chapter 5

Scaling of causal neural avalanches in a neutral model

This thesis chapter and accompanying appendix was published as the following research article:

Sakib Matin, Thomas Tenzin, and W. Klein. “Scaling of causal neural avalanches in a neutral model.” *Physical Review Research*, **3.1** (2021): 013107.

Abstract

Neural avalanches are collective firings of neurons that exhibit emergent scale-free behavior. Understanding the nature and distribution of these avalanches is an important element in understanding how the brain functions. We study a model of neural avalanches for which the dynamics are governed by neutral theory. The neural avalanches are defined using causal connections between the firing neurons. We analyze the scaling of causal neural avalanches as the critical point is approached from the absorbing phase. By using cluster analysis tools from percolation theory, we characterize the critical properties of the neural avalanches. We identify the tuning parameters consistent with experiments. The scaling hypothesis provides a unified explanation of the power laws which characterize the critical point. The critical exponents characterizing the avalanche distributions and divergence of the response functions are consistent with the predictions of the scaling hypothesis. We use a universal scaling function for the avalanche profile to find that the firing rates for

avalanches of different durations show data collapse after appropriate rescaling. We also find data collapse for the avalanche distribution functions, which is stronger evidence of criticality than just the existence of power laws. Critical slowing-down and power law relaxation of avalanches is observed as the system is tuned to its critical point. We discuss how our results motivate future empirical studies of criticality in the brain.

5.1 Introduction

Systems with many interacting units can exhibit phenomena at macroscopic scales which cannot be elucidated from their microscopic behavior (Stanley, 1971; Wilson, 1979). For a system at its critical point, emergent phenomena occur at all length scales and can be understood using concepts such as scaling and universality (Stanley, 1971; Stanley, 1999; Klein et al., 2007). There is a growing interest in the question of whether certain biological systems operate near a critical point (Muñoz, 2018b; Mora and Bialek, 2011; Hyman et al., 2014; Vicsek et al., 1995; Lo et al., 2004). A question that has received much attention is the question of whether the brain operates near a critical point (Muñoz, 2018b; Chialvo, 2010; Van Kessenich et al., 2016; Hahn et al., 2017; Dalla Porta and Copelli, 2019; Petermann et al., 2009; Priesemann et al., 2014; Shriki et al., 2013; Scarpetta and de Candia, 2014; Haimovici et al., 2013; Millman et al., 2010a; Das and Levina, 2019), commonly referred to as the criticality hypothesis (Muñoz, 2018b). Experiments have shown that neural avalanches *in vivo* and *in vitro* can exhibit scale-free behavior similar to thermal systems near the critical point (Lo et al., 2002; Beggs and Plenz, 2003; Zierenberg et al., 2018b; Friedman et al., 2012; Fontenele et al., 2019b; Clement et al., 2008). The interest in the criticality hypothesis has been amplified by arguments that criticality in the brain may benefit memory storage and information processing (Langton, 1990; Bertschinger

and Natschläger, 2004; Stoop and Gomez, 2016; Muñoz, 2018b; Honey et al., 2012; Gautam et al., 2015; Massobrio et al., 2015; Haldeman and Beggs, 2005; Shew et al., 2015; Kinouchi and Copelli, 2006; Boedecker et al., 2012).

The temporal-proximity binning method of defining neural avalanches (Beggs and Plenz, 2003; Zierenberg et al., 2018b; Friedman et al., 2012; Fontenele et al., 2019b; Clement et al., 2008; Ribeiro et al., 2014; Levina and Priesemann, 2017) can show discrepancies from the true behavior of avalanches especially when multiple avalanches propagate through the system (Martinello et al., 2017; Villegas et al., 2019). *Martinello et al.* (Martinello et al., 2017) partly addressed this issue by defining avalanches using causal-connections between firing neurons. Additionally, *Martinello et al.* (Martinello et al., 2017), studied a minimal model of neural avalanches, which is the contact process (Hinrichsen, 2000) where multiple neutral causally connected avalanches can propagate concurrently. We also study this neutral contact process here. The avalanche distributions in the active phase of the neutral contact process were studied in Ref. (Martinello et al., 2017). In this chapter, we study the scaling of causal neural avalanches as the critical point is approached from the absorbing phase, where there are no infinite avalanches. Our analysis reveals the relevant scaling fields or tuning parameters in the absorbing phase. We show that the causal neural avalanches are consistent with the scaling hypothesis. Additionally, we discuss how our analysis can motivate future experiments.

The remainder of the chapter is structured as follows. In Sec. 5.2, we outline the neutral contact process and discuss the connections to experimental studies of criticality in neural systems. We provide a brief pedagogical introduction to cluster scaling methods in Sec. 5.3. In Sec. 5.4, we measure the critical exponents τ and σ which characterize the scale-free causal avalanche distributions at the critical point. We approach the critical point from the absorbing phase. We find data col-

lapse of the distributions of avalanche size and duration near the critical point. In Sec. 5.5 we study how the response function diverges as a power law as the critical point is approached. We show that our measured critical exponents are consistent with the scaling hypothesis in Sec. 5.6. We find that the relevant scaling field in the neutral contact process are consistent with the different tuning parameters in experiments (Zierenberg et al., 2018b; Shew et al., 2009; Beggs and Plenz, 2003; Poil et al., 2012). In Sec.5.7, we analyze the scaling relation between the avalanche size and duration. In Sec. 5.8, we use scaling arguments to derive the universal avalanche profile and show data collapse for the firing rates for avalanches of different durations. Critical slowing down is analyzed in Sec. 5.9. In Sec. 5.10, we analyze the universal relaxation dynamics in the neutral contact process near the critical point. Lastly, in Sec. 5.11 we discuss our results, which indicate that the neutral contact process is consistent with the predictions of the scaling hypothesis. Additionally, we discuss how our results may inform future empirical studies of neural systems.

5.2 Model

The brain is a complex system consisting of many interacting neurons. In the resting state, neurons have intrinsic voltages which fluctuate around some residual value. A neuron, triggered by some stimuli (endogenous or external), sends its action potential or spikes to its connected neighbors. A recipient neuron may also fire and send its spike to the connected neighbors thereby resulting in an avalanche. The firing neurons in this avalanche are causally connected. *Martinello et al.* (Martinello et al., 2017), defined neural avalanches in the neutral contact process using causal-connections and showed that this definition of neural avalanches does not suffer the ambiguities commonly found in the temporal-proximity binning method (Villegas et al., 2019). Multiple neural avalanches can propagate concurrently in the neutral contact process

because of the causally connected definition. The avalanches are neutral (Martinello et al., 2017; Kimura, 1991; Azaele et al., 2016) or symmetric because the rates that describe the dynamics of the avalanches are the same for all labels, which distinguish the different avalanches.

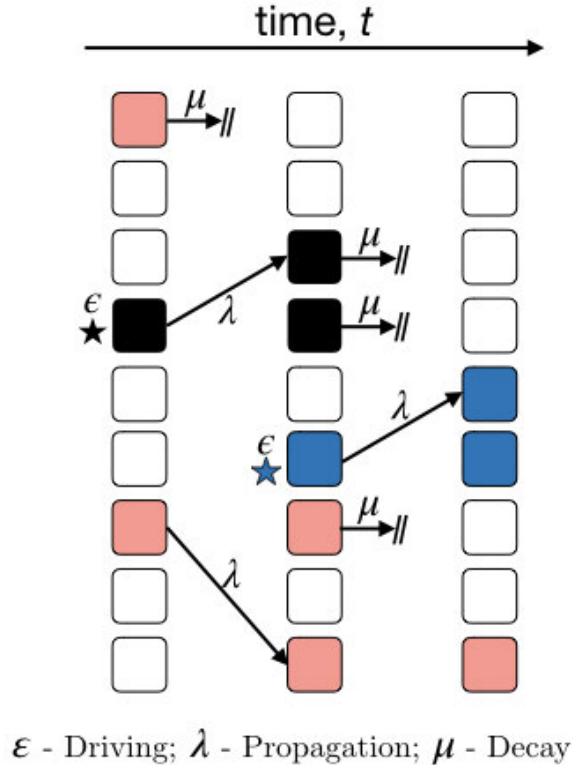


Figure 5.1: Neutral theory describes the dynamics of causal neural avalanches. The boxes correspond to neurons and each column to the right is the system at a later time step. Different colors correspond to different causal avalanches. The rates for the dynamics are identical for all avalanches. A new avalanche is triggered at the driving rate ϵ and is marked with a star. An active neuron can trigger an inactive neuron anywhere in the system at the propagation rate λ . Both neurons share the same label as they are causally connected. An active neuron becomes inactive at the decay rate μ . For the neural avalanche labeled by black, the size $S = 2$ is the total number of activated neurons and the duration $D = 2$ is the time elapsed between the first activation until all the black neurons become inactive.

The neutral contact process consists of N neurons which are fully connected. Ev-

ery neuron interacts with every other neuron. A neuron is either inactive, I , or active A_k , where the index k denotes the avalanche label. In Fig. 5-1, different colors correspond to different causal neural avalanches. The stochastic dynamics of the avalanches are described by rate equations. A new avalanche with a new label is triggered at the *driving rate* ϵ . An avalanche increases in size at the *propagation rate* λ as inactive neurons are triggered by active neurons. Active neurons become inactive at the *decay rate* μ . The rate equations describing the neutral contact process (Martinello et al., 2017) are

$$I \xrightarrow{\epsilon} A_{\max[k]+1} \quad (5.1)$$

$$I + A_k \xrightarrow{\lambda} A_k + A_k \quad (5.2)$$

$$A_k \xrightarrow{\mu} I \quad (5.3)$$

An avalanche ends when all neurons with a given label k become inactive. The size S of the causal neural avalanche is the number of activations and the avalanche duration D is the time between the activation of the first neuron with label k to when all neurons with index k become inactive, as shown in Fig. 5-1.

The neutral contact process captures many of the salient biological mechanisms relevant to neural avalanches. In neural systems, the ratio of inhibitory to excitatory neurons (Shew et al., 2009; Beggs and Plenz, 2003; Poil et al., 2012) and the spontaneous triggering rate (Zierenberg et al., 2018b; Priesemann et al., 2013) affect the statistics of neural avalanches. In the neutral contact process, we can tune the propagation rate, λ , and the decay rate, μ , to achieve an analogous result to varying the ratio of inhibitory and excitatory neurons in experiments. In addition, the driving rate ϵ in the neutral contact process is analogous to the spontaneous triggering of neurons (Zierenberg et al., 2018b; Meisel et al., 2013). For these reasons, we can explore the criticality of neural avalanches in the neutral contact process in a way

that is comparable to experiments.

We only study causal neural avalanches in the absorbing phase of the neutral contact process, where $\mu \geq \lambda$ and $\epsilon \geq 0$. We simulate the model using a discrete-time asynchronous random update (Hinrichsen, 2000; Henkel et al., 2008). We discuss how the code is implemented. A neuron is randomly chosen at each time step. If the neuron is inactive, then a new causal avalanche is triggered with probability ϵ . If the neuron is active, then it becomes inactive with probability μ ; otherwise, another inactive site becomes part of the same causal avalanche. All our simulations are run at $N = 10^4$, similar to Ref. (Martinello et al., 2017). The simulations were repeated for different systems sizes up to $N = 10^5$ to ensure that the measured values had converged. Additionally, we confirmed that the system is effectively ergodic using the Thirumalai-Mountain metric (Thirumalai et al., 1989; Thirumalai and Mountain, 1990; Thirumalai and Mountain, 1993). We collected data on time scales much larger than the mixing time (the time needed for the system to reach effective ergodicity).

5.3 Theory

Different physical systems exhibit universal properties near the critical point (Stanley, 1999). We can understand the nature of a critical point by analyzing the statistical properties of fluctuations or clusters in the system (Stanley, 1971; Stauffer and Aharony, 2018; Serino et al., 2011). By using real-space renormalization group techniques (Coniglio and Klein, 1980; Klein et al., 2007), we can map domains in magnetic systems undergoing a thermodynamic phase transition to clusters in percolation models undergoing a geometric phase transition. Cluster analysis methods from percolation theory have even been used to study non-equilibrium phase transitions in integrate-and-fire systems (Matin et al., 2020). Reference (Stauffer, 1979) provides a summary of scaling in percolation theory. We will use similar cluster anal-

ysis methods to study the scaling of causal avalanches in the absorbing phase of the neutral contact process.

We can obtain thermal quantities from the the avalanche number density, $n_S(S)$ which characterizes the probability of an avalanche of size S . Near the critical point, the number density for $S \gg 1$ is

$$n_S \sim S^{-\tau} G\left(\frac{S}{S_c}\right). \quad (5.4)$$

The τ exponent characterizes the power law distribution at the critical point. The characteristic size S_c diverges as the system approaches the critical point, and the avalanche number density becomes a power law, $n_S \sim S^{-\tau}$. The Fisher ansatz (Fisher, 1967; Stauffer, 1975) assumes that the scaling function $G(x)$ is given by $G(x) = \exp(-x)$. Equation. 5.4 and the Fisher ansatz has been applied to many systems (Matin et al., 2020; Serino et al., 2011) and we will show that it is consistent with the neutral contact process.

A system is said to be scale-free when the avalanche distribution follows a true power law, $n_S \sim s^{-\tau}$. In the scale-free case, we can plot $n_S = N_0 s^{-\tau}$ on a log-log plot to find a straight line with slope $-\tau$. Deviations from the power law occur when the system is not at the critical point. The exponential cutoff corresponds to $G(x)$ and appears as a “knee” in the log-log plot (Matin et al., 2020). Distributions with a cut-off at some characteristic scale are not scale-free. The finite lattice size in simulations also sets a cut-off.

The scaling hypothesis was originally introduced to explain the universal behavior across disparate thermodynamic systems (Stanley, 1971). According to the scaling hypothesis, the asymptotic behavior of various thermodynamic functions follow power laws characterized by critical exponents. The power laws are interconnected because they are caused by the same underlying mechanism. The predictions of the scaling

hypothesis have been verified in both experiments and numerical models (Stanley, 1971). Later, renormalization group methods have been used to justify the scaling hypothesis (Stanley, 1999).

We review the scaling of thermodynamic quantities and introduce critical exponents from statistical mechanics. Response functions quantify the change in macroscopic behavior caused by changes in intensive parameters (Stanley, 1971). Our definition of the response function χ is the same as in percolation theory (Stauffer, 1979; Stauffer and Aharony, 2018; Sahini and Sahimi, 1994), namely

$$\chi = \frac{\sum_S S^2 n_S}{\sum_S S n_S}. \quad (5.5)$$

The response function χ is analogous to the magnetic susceptibility in the Ising model (Stanley, 1971). The response function diverges (Stanley, 1971) as

$$\chi \sim h^{-\gamma}, \text{ as } h \rightarrow 0, \quad (5.6)$$

where h is the difference between the tuning parameter and its critical value. Divergent response functions are hallmarks of a system near its critical point (Stanley, 1971). The characteristic avalanche size S_c scales (Stanley, 1971; Stauffer and Aharony, 2018) as

$$S_c \sim h^{-1/\sigma}. \quad (5.7)$$

We use scaling arguments to relate the asymptotic behavior of thermodynamic quantities near a critical point. The scaling of the characteristic avalanche size S_c as a function the correlation length serves as a good pedagogical example. The correlation length ξ scales as

$$\xi \sim h^{-\nu} \implies \xi^{-1/\nu} \sim h. \quad (5.8)$$

The characteristic avalanche size scales as

$$S_c \sim h^{-1/\sigma} \sim [\xi^{-1/\nu}]^{-1/\sigma} \sim \xi^{1/\sigma\nu}. \quad (5.9)$$

We will show that similar scaling arguments hold for the causal avalanches in the neutral contact process.

5.4 Scale-free avalanche distribution

In this section, we study the causal avalanche size and duration distributions in the absorbing phase of the neutral contact process where $\mu \geq \lambda$ and $\epsilon \geq 0$.

One of the challenges of the criticality hypothesis is that the tuning parameters in real neural systems are not known. Different experiments have suggested different tuning parameters (Zierenberg et al., 2018b; Shew et al., 2009; Poil et al., 2012). In Ref. (Zierenberg et al., 2018b), the experiments *in vitro* and *in vivo* show that the spontaneous triggering rate of neurons may be interpreted as a tuning parameter. This parameter corresponds to ϵ in the neutral contact process. The experiments reported in Ref. (Shew et al., 2009; Beggs and Plenz, 2003; Poil et al., 2012) use pharmacological means to alter the excitation-inhibition ratio to alter the proximity to the critical point. We can achieve similar results by varying the rates λ and μ . Our analysis shows that the relevant scaling fields for the neutral contact process depends on ϵ and propensity $\Delta = \mu - \lambda$, which are consistent with the different experimental results (Zierenberg et al., 2018b; Shew et al., 2009; Beggs and Plenz, 2003; Poil et al., 2012). We find that the critical point for the neutral contact process is $\Delta = \mu - \lambda = 0$ and $\epsilon = 0$. We find that the distributions of avalanche sizes and durations follows power laws for $\Delta = 0$ and $\epsilon = 0$. Larger avalanches are suppressed for $\epsilon > 0$ and $\Delta > 0$.

In Fig. 5.2 we observe that the distribution of the avalanche sizes n_S and duration

n_D satisfy a power law at the critical point with the exponents τ and τ_D . As we tune the system away from the critical point by increasing the driving ϵ or the propensity Δ , we find exponential suppression of the large avalanches characterized by the exponents σ and σ_D for the size and duration respectively. The distribution functions for the avalanche size and duration are

$$n_S \sim S^{-\tau} \exp\left[-\frac{S}{S_c}\right], \quad (5.10)$$

$$n_D \sim D^{-\tau_D} \exp\left[-\frac{D}{D_c}\right], \quad (5.11)$$

where, S_c is the characteristic avalanche size and D_c is the characteristic duration size (Fisher, 1967; Stauffer, 1979; Stauffer and Aharony, 2018). For critical propensity $\Delta = 0$, the characteristic avalanche size scales as $S_c \sim \epsilon^{-1/\sigma}$ and the characteristic duration scales as $D_c \sim \epsilon^{-1/\sigma_D}$. When $\epsilon = 0$ the scaling for the characteristic size and duration are $S_c \sim \Delta^{-1/\sigma}$ and $D_c \sim \Delta^{-1/\sigma_D}$ respectively.

Our measured value of τ and τ_D in Fig. 5.2 are consistent with the theoretical mean-field values, $\tau^{\text{MF}} = 1.5$ and $\tau_D^{\text{MF}} = 2$ (Muñoz, 2018b) and experimentally reported values (Zierenberg et al., 2018b). In Fig. 5.3 we fit the exponents, σ and σ_D which characterize the exponential suppression of large avalanches. The critical exponents σ and σ_D for neural systems have not been reported in experiments.

A remarkable consequence of the scaling hypothesis is the existence of universal scaling functions which are usually obtained via data collapse (Stanley, 1971; Stanley, 1999; Sethna et al., 2001), where results for different values of the control parameters collapse on to a single curve after appropriate rescaling. In Fig. 5.2, the insets show data collapse for the distributions of the causal avalanches. In Fig. 5.2A, the causal avalanche size distribution for different values of ϵ is plotted. The scaling form is

$$n_S \sim S^{-\tau} \exp\left(-\frac{S}{S_c}\right) \sim S^{-\tau} \exp(-S\epsilon^{1/\sigma}). \quad (5.12)$$

We multiply both sides by $\epsilon^{-\tau/\sigma}$,

$$n_S \epsilon^{-\tau/\sigma} \sim \epsilon^{-\tau/\sigma} S^{-\tau} \exp(-S \epsilon^{1/\sigma}) \quad (5.13)$$

$$n_S \epsilon^{-\tau/\sigma} \sim (S \epsilon^{1/\sigma})^{-\tau} \exp(-S \epsilon^{1/\sigma}). \quad (5.14)$$

In the inset of Fig. 5.2A, we plot $n_S \epsilon^{-\tau/\sigma}$ as a function of the rescaled avalanche size $S \epsilon^{1/\sigma}$ to find data-collapse. The exact same scaling arguments can be used to derive the rescaled scaled variables in Fig. 5.2B, 5.2C and 5.2D, which are as follows

$$n_D \epsilon^{-\tau_D/\sigma_D} \sim (D \epsilon^{1/\sigma_D})^{-\tau_D} \exp(-D \epsilon^{1/\sigma_D}) \quad (5.15)$$

$$n_S \Delta^{-\tau/\sigma} \sim (S \Delta^{1/\sigma})^{-\tau} \exp(-S \Delta^{1/\sigma}) \quad (5.16)$$

$$n_D \Delta^{-\tau_D/\sigma_D} \sim (D \Delta^{1/\sigma_D})^{-\tau_D} \exp(-D \Delta^{1/\sigma_D}). \quad (5.17)$$

The data collapse of the causal avalanche distributions in the insets of Fig. 5.2 is compelling evidence relevant scaling fields or tuning parameters in the absorbing phase depends on ϵ and Δ . The results may be similar to the spinodal critical point in the Ising, where the scaling field is a linear combination of the magnetic field and temperature (Klein et al., 2007).

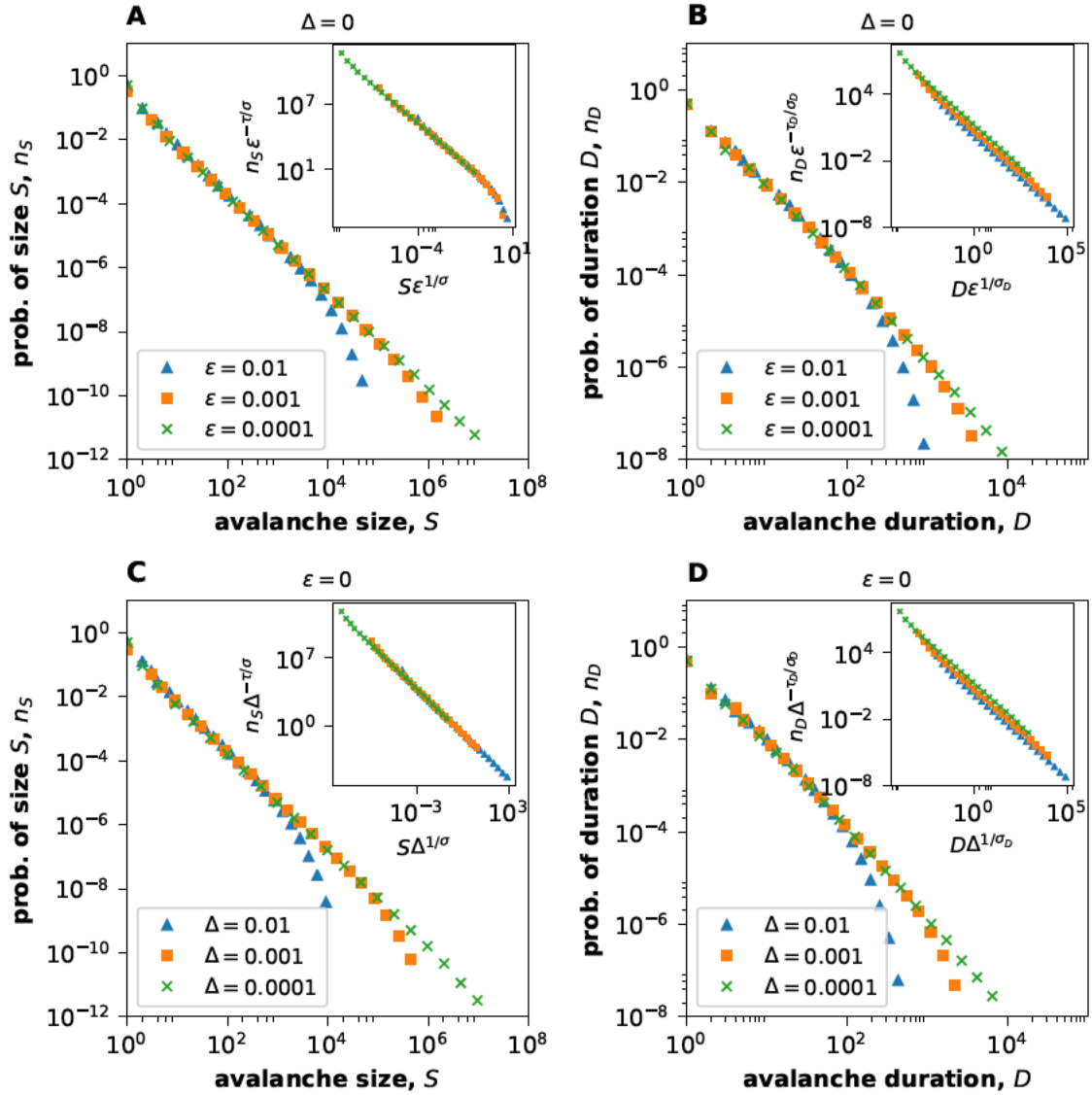


Figure 5-2: The distribution of avalanche sizes and durations follows a power law at the critical point, $\Delta = 0$ and $\epsilon = 0$. There is exponential suppression of large avalanches for $\Delta > 0$ and $\epsilon > 0$. The various exponents are the same for both tuning parameters. The inset shows data-collapse for the causal avalanche distributions. In the **top row**, $\Delta = 0$ and ϵ is varied. (A) The exponents for the avalanche size distribution $\tau = 1.53 \pm 0.05$. (B) The avalanche duration distribution is characterized by $\tau_D = 1.92 \pm 0.11$. In the **bottom row**, Δ is varied for $\epsilon = 0$. (C) The corresponding exponent $\tau = 1.51 \pm 0.05$. (D) $\tau_D = 1.93 \pm 0.11$ is the critical exponent for the avalanche duration distribution.

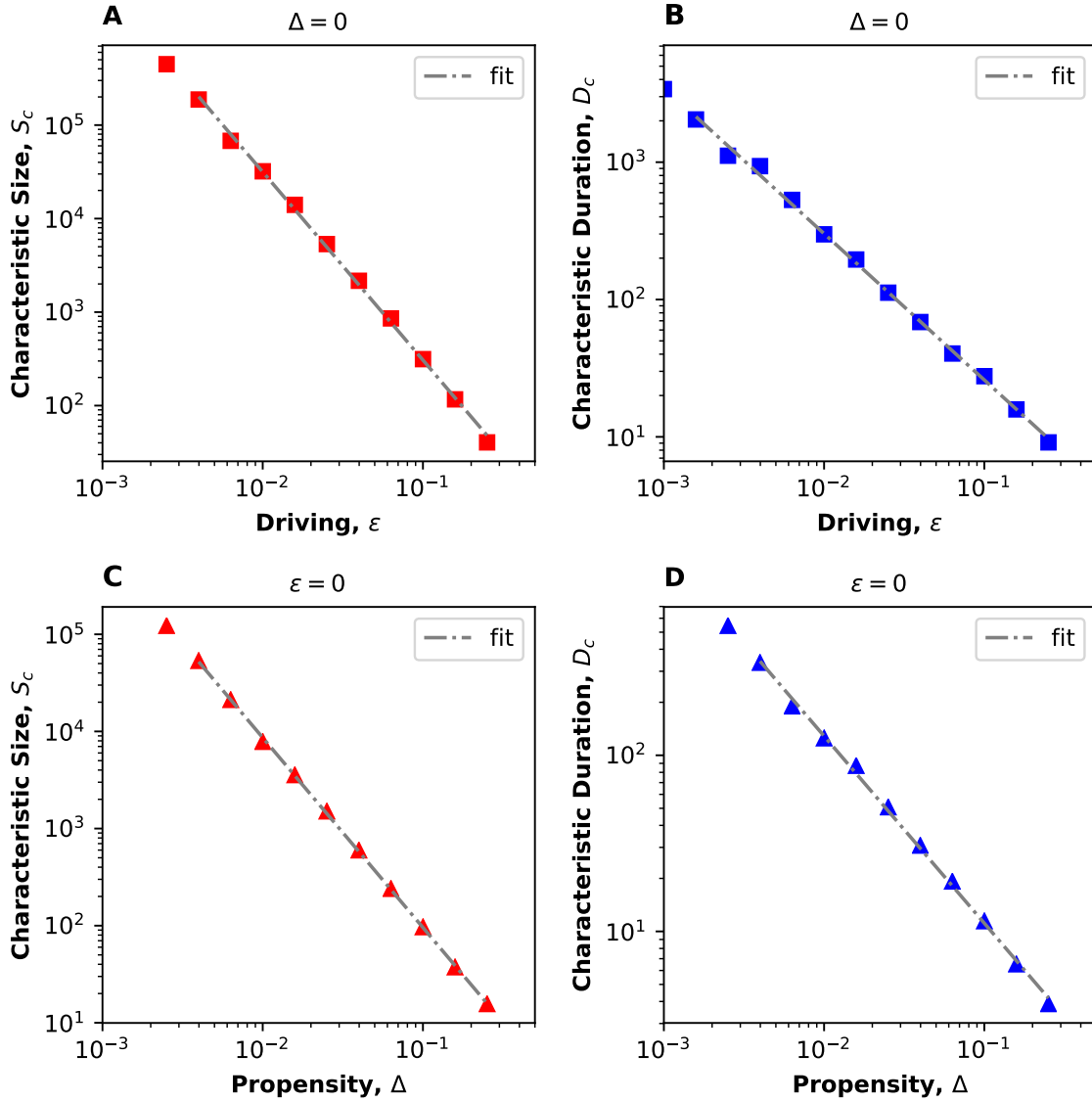


Figure 5-3: The characteristic avalanche size S_c and duration D_c diverge as the critical point is approached. For each value of Δ or ϵ , we fit the avalanche size and duration distributions to Eq. 5.10 and Eq. 5.11 to obtain S_c and D_c respectively. In the **top row**, ϵ is varied at fixed $\Delta = 0$. (A) The characteristic avalanche size S_c diverges with critical exponent $\sigma = 0.54 \pm 0.07$. (B) The characteristic duration D_c diverges with critical exponent $\sigma_D = 0.95 \pm 0.06$. In the **bottom row**, Δ is varied at fixed $\epsilon = 0$. (C) The measured exponent for S_c is $\sigma = 0.52 \pm 0.08$. (D) The characteristic duration diverges with the exponent $\sigma_D = 1.02 \pm 0.09$.

5.5 Divergent Response Functions

Divergent response functions are hallmarks of critical points (Stanley, 1971). We consider response function χ , which is from percolation theory, is given by (Stauffer, 1979; Matin et al., 2020)

$$\chi = \frac{\sum_S S^2 n_S}{\sum_S S n_S}. \quad (5.18)$$

In Fig. 5.4, the exponent γ is found to be the same whether the critical point is approached by decreasing Δ at $\epsilon = 0$ or by decreasing ϵ at $\Delta = 0$. When we vary Δ we measured $\gamma = 2.00 \pm 0.02$ and when we vary ϵ the exponent is $\gamma = 1.97 \pm 0.04$.

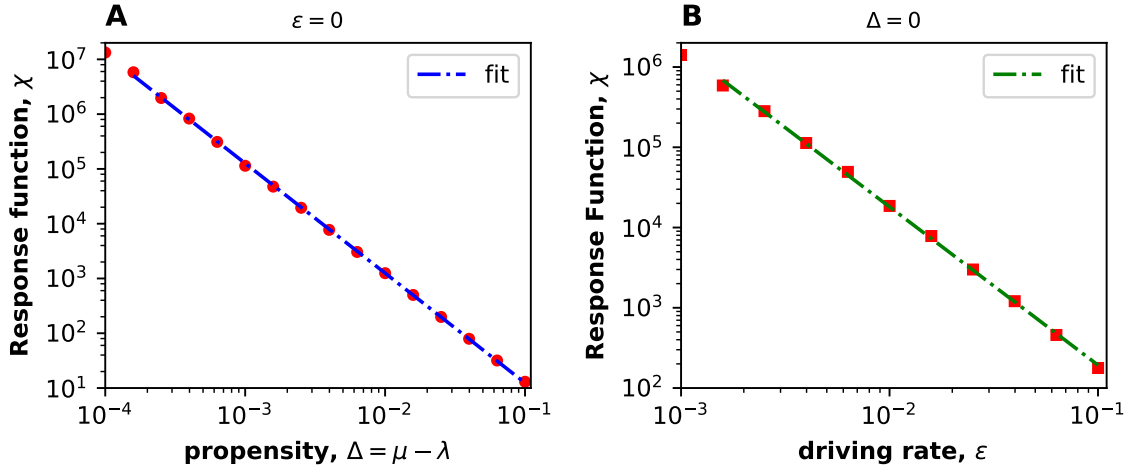


Figure 5.4: The response function χ diverges as the system approaches the critical point. The exponent γ characterizes the divergence and is the same when the critical point is approached at constant driving $\epsilon = 0$ or $\Delta = 0$. (A) For $\epsilon = 0$, when Δ is varied the exponent is $\gamma = 2.00 \pm 0.02$ (B) Varying the driving rate ϵ , the exponent is $\gamma = 1.97 \pm 0.04$ for $\Delta = 0$.

Our results indicate that the response function in the neutral contact process diverges as we vary ϵ or Δ in the absorbing phase.

5.6 Scaling Relations

The scale-free behavior at critical points can be attributed to underlying singularities in thermodynamic functions (Fisher, 1967; Stanley, 1971). We use scaling theory to relate the different critical exponents in the neutral contact process.

According to the scaling hypothesis, the response functions can be described by generalized homogeneous functions near the critical point (Stanley, 1971). We can write χ in Eq. 5.18 as

$$\chi = \frac{\sum_S S^2 n_S}{\sum_S S n_S}, \quad (5.19)$$

$$= \frac{\int_1^\infty S^{2-\tau} G(S/S_c) dS}{\int_1^\infty S^{1-\tau} G(S/S_c) dS}. \quad (5.20)$$

We make change of variables $u = S/S_c$ to find

$$\chi = \frac{S_c^{3-\tau} \int_{1/S_c}^\infty u^{2-\tau} G(u) du}{S_c^{2-\tau} \int_{1/S_c}^\infty u^{1-\tau} G(u) du}, \quad (5.21)$$

and set $G(u) = \exp(-u)$ (Fisher, 1967). As we approach the critical point, $1/S_c \rightarrow 0$. When evaluating the first and second moment, the argument of the exponential can be taken to be zero between up to $\epsilon S^\sigma \sim 1$ (Stauffer and Aharony, 2018), so the integrals can be replaced by the gamma function Γ (Arfken and Weber, 1999), and we can express χ as

$$\chi \sim S_c \frac{\Gamma(3-\tau)}{\Gamma(2-\tau)}. \quad (5.22)$$

Near the critical point, we find that the response function scales as $\chi \sim S_c$, where the characteristic size S_c scales as $\epsilon^{-1/\sigma}$. The scaling relation between the critical exponents are

$$\epsilon^{-1/\sigma} \sim \epsilon^{-\gamma} \implies \gamma = 1/\sigma. \quad (5.23)$$

Our measured exponents in Figs. 5.3 and 5.4 are consistent with Eq. (5.23). The results are the same when we vary Δ at $\epsilon = 0$. Our derivation is similar to scaling arguments used in percolation theory (Stauffer, 1979), except that the denominator of the response function also contributes to the divergence.

5.7 Size-Duration scaling of avalanches

We can relate the size of the causal avalanches to their duration using scaling arguments similar to Ref. (Sethna et al., 2001). The critical point is approached by varying ϵ for $\Delta = 0$. The average avalanche size follows the same scaling as the characteristic avalanche size, $\langle S(D) \rangle \sim \epsilon^{-1/\sigma}$ [-Reference equation 5.22 after fixing]. The correlation length scales as $\xi \sim \epsilon^{-\nu}$. The dynamic critical exponent z relates the duration D to ξ (Muñoz et al., 1999a; Roli et al., 2018). The scaling of D is

$$D \sim \xi^z \sim \epsilon^{-\nu z}, \quad (5.24)$$

$$D^{-1/\nu z} \sim \epsilon. \quad (5.25)$$

Now we can relate the average size $\langle S(D) \rangle$ to the duration as

$$\langle S(D) \rangle \sim \epsilon^{-1/\sigma} \sim [D^{-1/\nu z}]^{-1/\sigma}, \quad (5.26)$$

$$\sim D^{1/(\sigma \nu z)}. \quad (5.27)$$

The same scaling arguments can be used when Δ is varied for $\epsilon = 0$.

The critical exponents for the distribution of avalanche size and duration can be related to the exponent $\sigma \nu z$, by the identity (Sethna et al., 2001)

$$\frac{\tau_D - 1}{\tau - 1} = \frac{1}{\sigma \nu z}. \quad (5.28)$$

We measure the exponents on the left and right side of Eq. 5.28 independently. From

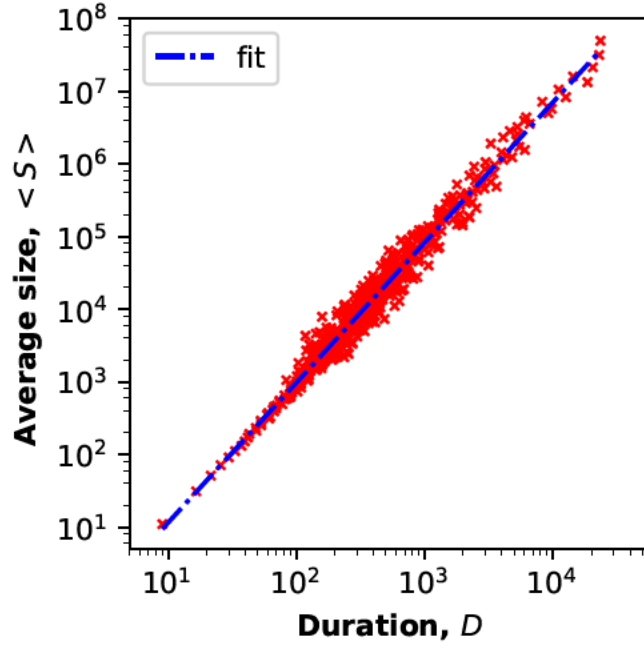


Figure 5.5: The scaling of the average avalanche size as a function of the duration at the critical point is consistent with the scaling laws. At the critical point the scaling is $\langle S(D) \rangle \sim D^{1/\sigma\nu z}$. The numerical estimate of $\frac{1}{\sigma\nu z} = 1.96 \pm 0.03$ is consistent with Eq. 5.28.

Fig. 5.5 the measured value of $1/(\sigma\nu z) = 1.93 \pm 0.03$ is consistent with the measured values of $(\tau_D - 1)/(\tau - 1)$ in Fig. 5.2. The scaling relation between the size and duration of neural avalanches has been verified experimentally (Fontenele et al., 2019b; Friedman et al., 2012). The predictions of the scaling hypothesis provide stricter criteria for criticality than just the existence of power law distributions.

5.8 Universal Avalanche Profile

The avalanche profile, which describes the firing rate as a function of time, can be described by a universal scaling function near the critical point. The firing rate corresponds to the number of activations per unit time. From the scaling hypothesis, we assume the average firing rate is described by a generalized homogeneous function,

which can be written as $f_R(t, D) = D^b f_R(t/D)$ (Stanley, 1971; Sethna et al., 2001; Gleeson and Durrett, 2017; Ponce-Alvarez et al., 2018). We compute exponent the exponent b ,

$$\langle S(D) \rangle = \int f_R(t, D) dt = \int D^b f_R(t/D) dt \sim D^{b+1}. \quad (5.29)$$

By using the scaling identity $\langle S(D) \rangle \sim D^{1/(\sigma\nu z)}$, we find $b = 1/(\sigma\nu z) - 1$. Figure 5-6 shows the data collapse for avalanches of different durations, when we scale the firing rate by $D^{1-1/(\sigma\nu z)}$ and plot it as a function of the rescaled time t/D . Our derivation follows Ref. (Sethna et al., 2001).

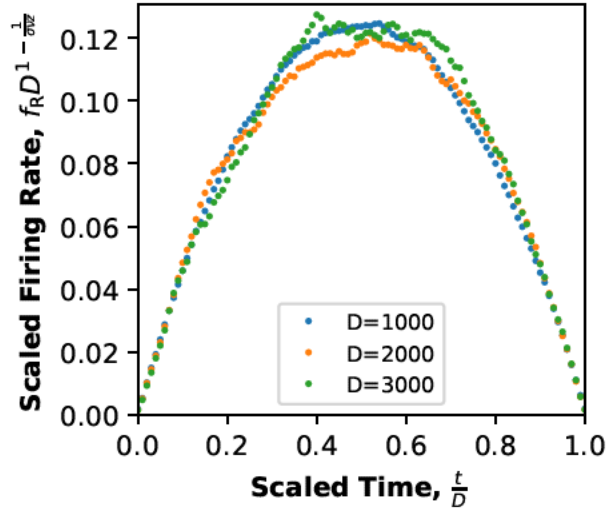


Figure 5-6: Neural avalanches have a universal avalanche profile at the critical point. The firing rate scaled by $D^{1-1/(\sigma\nu z)}$ as a function of the rescaled time t/D shows data collapse for avalanches of different durations.

Data collapse is an impressive example of universality in neural avalanches. Universal scaling functions can be used as strict criteria for criticality because the data collapse is observed only sufficiently close to the critical point. Under certain circumstances, data collapse for the avalanche profile has been reported for *in vitro*

experiments (Friedman et al., 2012; Yu et al., 2013; Fontenele et al., 2019b), where the avalanches are defined using the temporal proximity binning method. Our result shows that causal avalanches in the absorbing phase of the neutral contact process follow similar scaling behavior.

5.9 Critical Slowing down

A well-known consequence of criticality is a time scale that diverges as the critical point is approached (Hohenberg and Halperin, 1977b). This phenomenon is known as critical slowing down. Here, we analyze how the time to reach a stationary state diverges as the system is tuned to the critical point.

We study the equilibration time for neutral contact process after initializing with a single active neuron. We analyze the dynamics of $U(t)$, which is the number of unique causal avalanches at time t . $U(t)$ is a population level quantity because it is computed using information from the entire system at a particular instance in time. We determine that the system has reached a stationary state when $U(t)$ reaches a constant rolling time average. In Fig. 5.7 we plot the time for $U(t)$ to reach a steady state T_E as a function of the driving rate ϵ at $\Delta = 0$. We can use scaling arguments to relate the dynamic exponent z to the other critical exponents; the correlation length and time scale as $\xi \sim \epsilon^{-\nu}$ and $t \sim \xi^z$ respectively. In Fig. 5.7 as the system approaches the critical point, T_E diverges as

$$T_E \sim \xi^z \sim \epsilon^{-\nu z}. \quad (5.30)$$

Our measured dynamic critical exponent $\nu z = 0.95 \pm 0.04$ is consistent with Eq. 5.28 and $1/(\sigma\nu z)$, where σ is determined in Fig. 5.3. The measured exponent remains the same when we repeat the analysis using the total activity, ρ , instead of U . Hence, the neutral contact process exhibits a divergent time scale characteristic

of critical systems and is consistent with the scaling hypothesis.

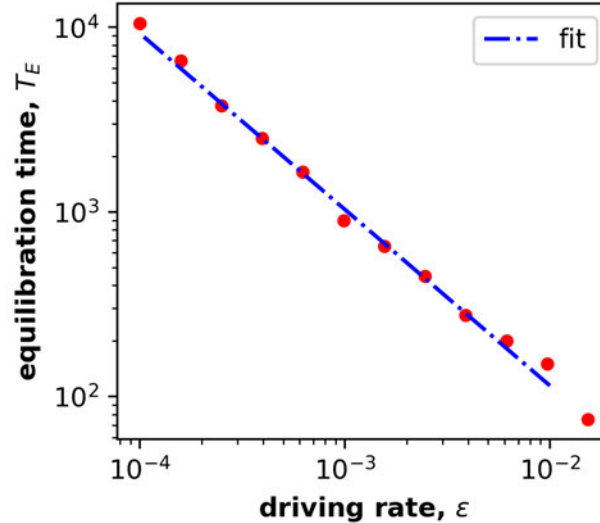


Figure 5.7: The equilibration time T_E diverges as the system approaches the critical point $\epsilon \rightarrow 0$ with $\Delta = 0$. T_E is the time for $U(t)$ to reach a steady-state value when the neutral contact process is initiated with a single active neuron. We find $T_E \sim \epsilon^{-\nu z}$. The measured value, $\nu z = 0.95 \pm 0.04$, is consistent with scaling arguments.

5.10 Relaxation Dynamics

Power law temporal relaxation is a hallmark of critical systems (Hohenberg and Halperin, 1977b). We initialize the neutral contact process with every neuron active and belonging to a unique causal avalanche and analyze the relaxation to either a fluctuating state or to an absorbing (inactive) state. In Fig. 5.8A, we vary ϵ for $\Delta = 0$ and analyze how the system decays to a fluctuating state. In Fig. 5.8B the system decays to an absorbing state as we have set the driving rate $\epsilon = 0$. We find that the number of unique avalanches, $U(t)$, decays as a power law for the critical value $\Delta = 0$, and exponentially for $\Delta > 0$. The critical exponent α characterizes the power law relaxation. Our measured value is $\alpha = 0.99 \pm 0.04$ in Fig. 5.8 and is consistent with the mean-field value $\alpha_{\text{MF}} = 1$ (Hinrichsen, 2000). Inset plots in

Figs. 5-8 show data collapse for the relaxation of $U(t)$ by plotting the rescaled variables $U \rightarrow Ut^\alpha$ as a function of $t \rightarrow (t|\epsilon|)^{\nu z}$ and $t \rightarrow (t|\Delta|)^{\nu z}$ respectively in Figs. 5-8A and B. This technique has been used in the study of directed percolation, which exhibits a nonequilibrium phase transition (Henkel et al., 2008; Hinrichsen, 2000). The data was averaged over 10^6 iterations.

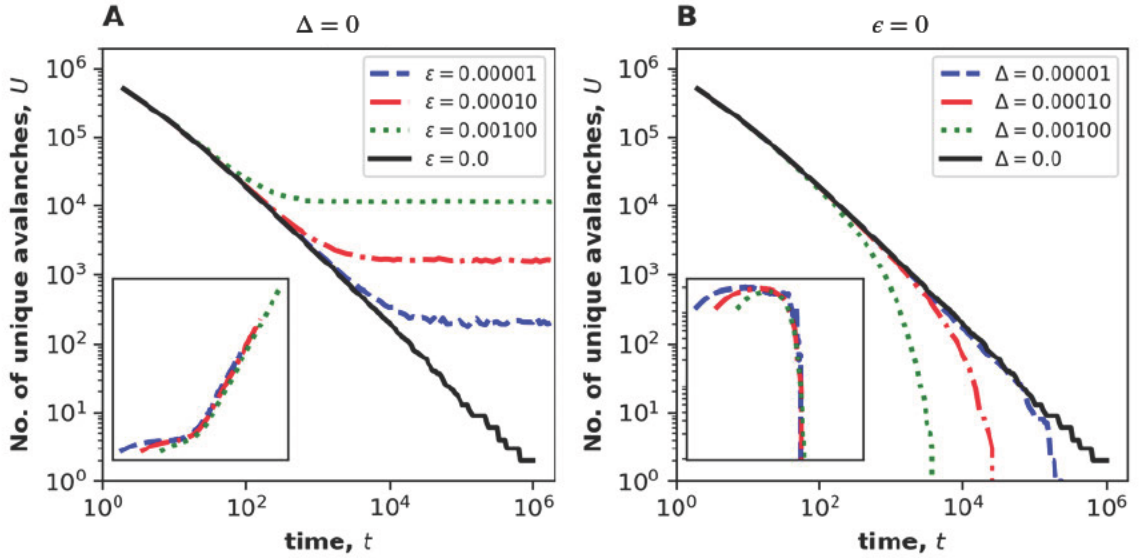


Figure 5-8: The number of unique causal neural avalanches $U(t)$ decays as a power law, $U(t) \sim t^{-\alpha}$, at the critical point. The measured critical exponent $\alpha = 0.99 \pm 0.04$ matches mean-field value $\alpha_{\text{MF}} = 1$. (A) For $\epsilon > 0$ and critical propensity $\Delta = 0$, $U(t)$ reaches a fluctuating state. (B) For sub-critical propensity $\Delta > 0$ and $\epsilon = 0$, $U(t)$ decays exponentially to the absorbing state. Inset plots show data collapse for the rescaled variables.

Our analysis of other dynamical properties in the neutral contact process also support criticality. For finite values of the driving rate ϵ the system evolves to a stationary state. The time-averaged value of the number of unique clusters scales as $\langle U \rangle \sim \epsilon^\lambda$ where $\lambda = 0.80 \pm 0.02$. The divergence in the time scale to reach the stationary state was analyzed in Sec 5.9.

By studying the dynamics of population level quantities, we have found character-

istic power laws at the critical point. Furthermore, the data collapse for the decay of $U(t)$ highlights the universal dynamics in the neutral contact process near the critical point.

5.11 Discussion

Scale-free neural avalanches *in vivo* and *in vitro* are a remarkable emergent phenomena which have intrigued physicists (Muñoz, 2018b) and neuroscientists (Beggs and Timme, 2012; Clawson et al., 2017; Shew and Plenz, 2013). The theory of critical phenomena is a promising explanation of the scale-free behavior (Friedman et al., 2012; Fontenele et al., 2019b; Levina et al., 2009), and is further motivated by the arguments that criticality in the brain may have functional advantages (Shew and Plenz, 2013).

We have analyzed the scaling of causal neural avalanches in the absorbing phase of the neutral contact process. As we allow the different parameters to approach their critical values, the response function exhibits a power law divergence, similar to thermal systems (Stanley, 1971). Additionally, the causal neural avalanches show scale-free distributions for $\Delta = 0$ and $\epsilon = 0$. Large causal neural avalanches are exponentially suppressed when $\epsilon > 0$ and $\Delta > 0$. The values of the critical exponents τ and τ_D in Ref. (Martinello et al., 2017) are consistent with our measured values. We used cluster analysis techniques to study the causal avalanches and measure critical exponents, σ , σ_D , γ and νz . Our measured exponents obey scaling laws in Eq. 5.23. We use scaling arguments to relate the average avalanche size to the duration and numerically verify the result.

We construct a strict criteria for criticality in the neutral contact process using the scaling hypothesis. A striking prediction of the scaling hypothesis is the existence of universal scaling functions. In the neutral contact process, the avalanche profile shows

data collapse after appropriate rescaling. Similar data collapse has been observed in experiments (Friedman et al., 2012). We also find data collapse for the avalanche size and duration distribution. We showed that the dynamics of population level observables in the neutral contact process are also consistent with criticality. When we initialize the system with a single active neuron, the steady state is reached after some characteristic time. As the critical point is approached, we find there is a divergent time scale. The dynamic critical exponent is consistent with scaling arguments. We analyze how the system relaxes from a maximally diverse state. We find deviations from power law decay depend on the distance from the critical point. By using scaling arguments, we find data collapse for the relaxation dynamics.

Our analysis of the neutral contact process shows that the relevant scaling field in the absorbing phase depends on ϵ and Δ . The results of Ref. (Martinello et al., 2017) suggest that relevant scaling field depends only on ϵ in the active phase of the neutral contact process, where $\Delta < 0$. An important question is about the correspondence between the tuning parameters in experiments and those in the neutral contact process. The experiments in Ref. (Zierenberg et al., 2018b) imply that the control parameter may be the spontaneous triggering rate, which corresponds to the driving rate ϵ in the neutral contact process. In separate experiments (Shew et al., 2009; Beggs and Plenz, 2003; Poil et al., 2012), the excitation-inhibition ratio was varied to tune the system toward criticality, which we achieved by varying the propensity, Δ in the neutral contact process. However, in experiments the neural avalanches are defined using a temporal proximity binning method which can be different from the causal avalanche definition used in this work and in Ref. (Martinello et al., 2017). Our results emphasize the need to incorporate causal connections in future experiments studying neural avalanches as pointed out by Ref. (Martinello et al., 2017). Inferring causal information in real neural systems remains an open problem. Refer-

ences (Williams-García et al., 2017; Stavroglou et al., 2020) provide promising steps to address this issue. Additionally, Ref. (Zierenberg et al., 2020) has studied how coalescence in the microscopic dynamics can affect the macroscopic observables in the branching process.

Our results may motivate future experimental studies of neural avalanches. The divergence of the response function can be used to identify the critical point in real neural systems. We outline a possible way to experimentally verify the scaling relation $\gamma = 1/\sigma$. In an experiment, neural avalanches are recorded for different values of the tuning parameter f . The avalanche distribution function can be fit to $n_S \sim S^{-\tau} \exp[-S/S_c(f)]$, where $S_c(f)$ is the characteristic avalanche size for a given value of f . Additionally, the response function $\chi(f)$ can also be computed. We rescale the tuning parameter $f \rightarrow \bar{f}$ such that the log-log scaled plot of S_c against \bar{f} gives a straight line. Similarly, we can plot the response function χ against \bar{f} on a log-log scaled plot. The measured slopes for the two graphs will be the same if the $\gamma = 1/\sigma$ scaling law is obeyed. We would find better data collapse for firing rates from data sets where S_c and χ are large, as the data collapse indicates that the experimental system is near the critical point. Some of predictions of our scaling may even be verified using existing neural data as the effects of coalescence is expected to be small near the critical point. Experiments in Ref. (Friedman et al., 2012) reported data collapse for the avalanche profile in certain samples.

Numerous studies (Langton, 1990; Beggs and Plenz, 2003; Bertschinger and Natschläger, 2004; Muñoz, 2018b; Kinouchi and Copelli, 2006) have discussed the possible functional benefits of criticality in the brain. Ref. (Beggs and Plenz, 2003) showed that information transmission is maximized for critical neural avalanches. Our results raise the important question of if there are similar benefits associated with causal neural avalanches near the critical point. Spike-timing-dependent plasticity (STDP)

is a biological learning mechanism which uses causal information about firing neurons (Martinello et al., 2017; Stepp et al., 2015) to update synaptic weights between neurons. STDP has been shown to be responsible for maintaining stable retrievable firing patterns (Stepp et al., 2015). We have shown that the causal neural avalanches of all scales occur at the critical point. We plan to address the question of whether criticality enhances the number or stability of STDP firing patterns by studying causal neural avalanches in integrate and fire models of neurons.

Our work sheds new light on the scaling of causal neural avalanches. Our results indicate that the relevant scaling field in the absorbing phase of the neutral contact process is consistent with experiments (Zierenberg et al., 2018b; Beggs and Plenz, 2003). Our results motivate questions for future studies and provide a promising path to a unified theory of neural avalanches.

Acknowledgements

We would like to thank Ashish B. George and Harvey Gould for insightful comments and critical reading of the manuscript. T.T. would like to acknowledge financial support from Boston University's Undergraduate Research Opportunities Program.

Chapter 6

Scaling theory of Random Walk Return times in Arbitrary Dimensions

6.1 Introduction

Non-equilibrium phenomena such as stochastic dynamical systems are believed to be profoundly different from equilibrium thermodynamic processes which rely on highly restrictive assumptions such as detailed balance and ergodicity (Stanley, 1971; Sethna, 2021). Random walks are one of the earliest and well studied problems in statistics and are often used to model many non-equilibrium dynamical processes (Redner, 2001; Zwanzig, 2001) in finance (Peters and Klein, 2013; Smidt, 1968), biology (Birzu et al., 2019; Dalla Porta and Copelli, 2019; Azaele et al., 2016) and physics (Redner, 2001). Random walks go by colorful names such the drunkard's walk (Mlodinow, 2009). Despite their deceptive simplicity, random walks are known to exhibit intricate mathematical properties (Mlodinow, 2009; Redner, 2001).

We study the scaling behavior of trapping or return of biased random walkers. The trapping time is the number of steps taken for by a walker to reach an absorbing boundary condition. We will focus on random walks where the traps are set adjacent to the initial conditions. This is sometimes referred to as the return time of random walks (Redner, 2001). We show that vanishing bias (drift towards the absorbing boundary) corresponds to the critical point, where the distribution of return times can be described by a Fisher-Stauffer theory similar to percolation (Stauffer,

1979; Stauffer and Aharony, 2018). Our work suggest that certain non-equilibrium problems may be analyzed using scaling theories originally developed for the study of equilibrium systems (Stanley, 1971).

6.2 Model

We consider a D -dimensional discrete time unit step size random walker \mathbf{X} . The dynamics along each of the dimensions are independent. Therefore, we can write $\mathbf{X} = (x_1, x_2, \dots, x_D)$, where the components x_1, x_2, \dots, x_D are independent one-dimensional random walkers. At each time step x_i will increase by 1 with probability $p = 1/2 - \Delta$ and decrease by 1 according to probability $q = 1/2 + \Delta$, where Δ is the bias parameter.

We place traps or an absorbing boundary condition at the origin for each of our component random walkers. The random walk \mathbf{X} ends when any of the component walkers hit the trap. The size s of \mathbf{X} is incremented by 1, when each of the components takes a step without hitting the trap. We analyze the the statistics of the s the random walks that reach the trap at the origin.

We can visualize this model in an Euclidean coordinate system. For $D = 1$, the system is a one-dimensional random walker with a trap at the origin and the walker is constrained to the positive half of the x -axis. For $D = 2$, the walker is constrained to the positive quadrant and the traps are placed placed along the x and y axis. For $D = 3$, the traps are placed along the x , y and z axis and the walker is constrained to the positive octant. Although we are not able to visualize higher dimensions for arbitrary D dimension, the walker is constrained to the positive orthant with traps along each of the axes.

6.3 Scaling Theory

We can understand the nature of a critical point by studying the statistics of fluctuations or clusters (Stauffer and Aharony, 2018; Stanley, 1971; Klein et al., 2007; Serino et al., 2011; Fisher, 1967). Our main tool is cluster analysis, which is synonymous with percolation theory (Stauffer and Aharony, 2018; Stauffer, 1979) and has been applied to magnetic systems (Klein et al., 2007; Sethna et al., 2001), non-equilibrium phase transitions (Matin et al., 2020) and neural systems (Matin et al., 2021; Martinello et al., 2017; Fontenele et al., 2019b; Beggs and Plenz, 2003; Lo et al., 2002)

We briefly review the Fisher-Stauffer scaling theory in the context of our random walk model. The size (number of steps taken before hitting an absorbing boundary) distribution satisfies the Fisher-Stauffer form,

$$n_s \sim s^{-\tau} \exp\left(-\frac{s}{s_c}\right) \quad (6.1)$$

The characteristic size s_c diverges (Stauffer, 1979; Stauffer and Aharony, 2018) as the tuning parameter approaches the critical value

$$s_c \sim \Delta^{-1/\sigma} \quad (6.2)$$

The exponents τ and σ are the Fisher exponents. At the critical point, the distribution follows a power law and the system is said to be scale free (Matin et al., 2021; Stanley, 1999). As the system deviates from the critical point, the avalanche distribution is described by the power law with an exponential cut off. The exponential cut off appears as a ‘knee’ in a log-log scaled plot (Serino et al., 2011; Matin et al., 2021).

One of the most striking features of systems near a critical point is the existence of universal scaling functions which are obtained via data collapse, where plots for

different parameters collapse onto a single curve after appropriate rescaling. We rewrite the size distribution function from Eq. (6.1) as

$$n_s \sim s^{-\tau} \exp(-s\Delta^{1/\sigma}) \quad (6.3)$$

by using Eq. (6.2). We multiply both sides by $\Delta^{-\tau/\sigma}$, and regroup the terms, to find

$$\Delta^{-\tau/\sigma} n_s \sim [\Delta^{1/\sigma} s]^{-\tau} \exp(-s\Delta^{1/\sigma}). \quad (6.4)$$

From our simulations, we find that the rescaled distribution function $\Delta^{-\tau/\sigma} n_s$ as a function of the rescaled size $s\Delta^{1/\sigma}$ exhibits data collapse for different dimensions. Data collapse of the size distribution function is further evidence of criticality and that Δ is the relevant scaling field in this problem.

Critical exponents characterize the singular behavior of thermodynamic functions near the critical point. These critical exponents are related because they are all associated with the singular behavior at the critical point (Stanley, 1971). We can define thermodynamic functions using moments of the avalanche distribution function (Stauffer and Aharony, 2018; Klein et al., 2007; Reynolds et al., 1977). The response function, analogous to susceptibility in magnetic systems (Stanley, 1971), is defined as the ratio of the second moment of the distribution function to the first,

$$\chi = \frac{\sum_s s^2 n_s}{\sum_s s n_s} \quad (6.5)$$

Divergent response functions are hallmarks of systems near the critical point (Stanley, 1971; Stanley, 1999). The response function diverges (Stanley, 1971) as

$$\chi \sim \Delta^{-\gamma} \quad (6.6)$$

D	τ	σ	γ
1	1.52 ± 0.057	0.49 ± 0.07	2.01 ± 0.01
2	2.03 ± 0.04	0.51 ± 0.11	1.90 ± 0.17 (log-corrections)
3	2.55 ± 0.08	0.56 ± 0.08	1.06 ± 0.08
4	2.94 ± 0.14	0.45 ± 0.09	log-divergence

Table 6.1: Measures values of τ , σ , and γ critical exponents for random walk return times in $D = 1, 2, 3, 4$.

6.4 Measured Values of Critical Exponents

From our simulations, we have measured the τ , σ and γ exponents for $D = 1, 2, 3, 4$, as listed in Table. 6.1

Our simulations suggest indicates the exponent τ exponent depends on the dimension $\tau = 1 + D/2$. We find that the measured value of σ is consistent with $1/2$.

6.5 Return times for one dimensional walker

Without loss of generality, we consider only the discrete-time unit step size random walks which start at the origin. The probability that the random walker is at the origin after exactly $2n$ steps is the occupation probability g_{2n} in Eq. 6.7. The probability that the random walker returns to the origin for the first time at exactly $2n$ steps is first return probability f_{2n} in Eq. 6.28. The first return probability and the occupation probability are related by the convolution (Redner, 2001),

$$g_{2n} = \sum_{k=0}^{2n} f_k g_{2n-k}. \quad (6.7)$$

We introduce the generating functions for f_{2n} and g_{2n} respectively,

$$F(z) = \sum_{m=0}^{\infty} f_{2m} z^m \quad (6.8)$$

$$G(z) = \sum_{m=0}^{\infty} g_{2m} z^m \quad (6.9)$$

We can use the generating functions to show that the convolution relations in Eq. 6.7, becomes a product, which can be simplified as

$$F(z)G(z) = \left[\sum_{m=0}^{\infty} f_{2m} z^m \right] \left[\sum_{k=0}^{\infty} u_{2k} z^k \right]. \quad (6.10)$$

We introduce the change of variables $n = m + k$ for the summation indices, and use $f_{2n-2k} = 0$ for $k > n$ to write

$$F(z)G(z) = \sum_{n=0}^{\infty} \sum_{k=0}^n f_{2n-2k} g_{2k} z^n \quad (6.11)$$

$$= \sum_{n=0}^{\infty} g_{2n} z^n \quad (6.12)$$

$$= G(z) - 1 \quad (6.13)$$

$$F(z) = 1 - \frac{1}{G(z)} \quad (6.14)$$

$$(6.15)$$

Note that these relations hold for any finite bias and D .

For the one dimensional unbiased random walk, the occupation probabilities cor-

respond to the binomial distribution (Redner, 2001),

$$g_{2n} = \binom{2n}{n} 2^{-2n} \quad (6.16)$$

$$= \frac{(2n)!}{(n!)^2} 2^{-2n} \quad (6.17)$$

$$= \frac{(2n-1)!! 2^n}{n!} 2^{-2n} \quad (6.18)$$

$$= 2^{2n} (-1)^n \binom{-\frac{1}{2}}{n} 2^{-2n} \quad (6.19)$$

$$= (-1)^n \binom{-\frac{1}{2}}{n} \quad (6.20)$$

The generating function for the occupation probability is given by

$$G(z) = \sum_{n=0}^{\infty} g_{2n} z^n \quad (6.21)$$

$$= \sum_{n=0}^{\infty} g_{2n} z^n (-1)^n \binom{-\frac{1}{2}}{n} \quad (6.22)$$

$$G(z) = (1-z)^{-\frac{1}{2}} \quad (6.23)$$

By using Eq. 6.23 and Eq. 6.20 we can write the generating function of the first return probability

$$F(z) = 1 - \sum_{n=0}^{\infty} \binom{\frac{1}{2}}{n} (-z)^n \quad (6.24)$$

$$= \sum_{n=1}^{\infty} \binom{\frac{1}{2}}{n} (-1)^{n-1} z^n \quad (6.25)$$

The probability for first return in $2n$ steps can be written as

$$f_{2n} = (-1)^{n-1} \binom{\frac{1}{2}}{n} \quad (6.26)$$

$$= \frac{(-1)^n}{2n-1} \binom{-\frac{1}{2}}{n} \quad (6.27)$$

$$f_{2n} = \frac{g_{2n}}{2n-1} \quad (6.28)$$

Now, the random walker is biased to move away from the trap. The probability to step away from the trap is $1/2 - \Delta$.

The occupation probability at $2n$ step is given by

$$u_{2n} = \binom{2n}{n} \left[\frac{1}{2} - \Delta \right]^2 \left[\frac{1}{2} + \Delta \right]^2 \quad (6.29)$$

$$= \binom{2n}{n} \left[\frac{1}{4} - \Delta^2 \right]^n \quad (6.30)$$

$$= \binom{2n}{n} p^{2n} \quad (6.31)$$

The generating function for the biased one dimensional random walker is given by

$$U(z) = \sum_{n=0}^{\infty} \binom{2n}{n} p^{2n} z^n \quad (6.32)$$

$$= \sum_{n=0}^{\infty} \binom{-\frac{1}{2}}{n} 2^{2n} p^{2n} (-1)^n z^n \quad (6.33)$$

$$= \sum_{n=0}^{\infty} \binom{-\frac{1}{2}}{n} (4p^2)^n (-z)^n \quad (6.34)$$

$$= [1 - 4p^2 z]^{-\frac{1}{2}} \quad (6.35)$$

The generating function for the first return probability for the biased one dimensional walker is

$$F(z) = 1 - \frac{1}{G(z)} \quad (6.36)$$

$$= 1 - \sum_{n=0}^{\infty} \binom{-\frac{1}{2}}{n} (4p^2)^n (-z)^n \quad (6.37)$$

$$= \sum_{n=1}^{\infty} \binom{-\frac{1}{2}}{n} (4p^2)^n (-1)^{n-1} z^n \quad (6.38)$$

Therefore, the first return probability in $2n$ steps is given by

$$f_{2n} = \binom{\frac{1}{2}}{n} (-1)^{n-1} (4p^2)^n \quad (6.39)$$

$$= \frac{[-1]^n}{2n-1} \binom{-\frac{1}{2}}{n} (4p^2)^n \quad (6.40)$$

$$f_{2n} = \frac{u_{2n}}{2n-1} \quad (6.41)$$

6.6 Divergence Response Function

We present some preliminary work on analytically verifying the our numerical estimates of the critical exponent γ using the measured values of τ and σ for $D = 1, 2, 3, 4$.

The response function χ is the ratio of the second moment of the size distribution function to the first moment. We reproduce the expression here for convenience.

$$\chi = \frac{M_2}{M_1}. \quad (6.42)$$

We look at the response function for $D = 1, 2, 3, 4$.

We are interested in the limit $s \gg 1$ where the moment can be written as

$$M_k = \sum_{s=1}^{\infty} s^k n_s \quad (6.43)$$

$$\simeq \int_1^{\infty} s^k n_s ds \quad (6.44)$$

$$= \int_1^{\infty} s^{k-\tau} \exp\left(-\frac{s}{s_c}\right) ds \quad (6.45)$$

where s is now treated as quasi-continuous variable. We use the change of variable $y = -s/s_c$ to rewrite the integral,

$$M_k = \int_{1/s_c}^{\infty} s_c^{k+1-\tau(T)} s^{k-\tau(T)} \exp(-y) dy \quad (6.46)$$

where $\tau(D) = 1 + D/2$.

The response function χ is

$$\chi \simeq \frac{\int_{1/s_c}^{\infty} s_c^{3-\tau} y^{2-\tau} \exp(-y) dy}{\int_{1/s_c}^{\infty} s_c^{2-\tau} y^{1-\tau} \exp(-y) dy} \quad (6.47)$$

In the following derivation we suppress the argument of $\tau(D)$ to simplify our notation.

$D = 1$

The Fisher exponent is $\tau = 3/2$ and we find both M_2 and M_1 diverge for $T = 1$. Equation 6.47 can be evaluated as follows

$$\chi \simeq s_c \frac{\Gamma(3 - \tau)}{\Gamma(2 - \tau)} \text{ as } s_c \rightarrow \infty \quad (6.48)$$

$$= s_c \tau = \frac{3}{2} s_c. \quad (6.49)$$

We have used the definition of the Gamma-function

$$\Gamma(z) = \int_0^{\infty} e^{-t} t^{z-1} dt \quad (6.50)$$

and the identity,

$$\Gamma(z + 1) = z\Gamma(z) \quad (6.51)$$

The response function χ scales as the gap exponent, namely

$$\chi = \frac{M_2}{M_1} \sim s_c \sim \Delta^{-1/\sigma}. \quad (6.52)$$

Therefore, $\gamma = 2$ from our calculations, which is consistent with our numerical simulations for $D = 1$.

$D = 2$

We start from the Eq. 6.47 and use $\tau(2) = 2$ to find

$$\chi \simeq \frac{s_c \int_{1/s_c}^{\infty} \exp(-y) dy}{s_c^0 \int_{1/s_c}^{\infty} \frac{\exp(-y)}{y} dy} \quad (6.53)$$

$$= \frac{s_c \exp(-\frac{1}{s_c})}{E_1(1/s_c)} \quad (6.54)$$

The denominator has been expressed as the exponential function $E_1(1/s_c)$. The Puiseux series expansion for the Exponential Integral function (Arfken and Weber, 1999),

$$E_1(z) \simeq -\mu - \ln(z) \quad (6.55)$$

where μ is the Euler-Mascheroni constant.

When $D = 2$, the response function scales as

$$\chi \sim \frac{s_c}{\ln(s_c)} \quad (6.56)$$

$$\sim \frac{\Delta^{-1/\sigma}}{-\ln(\Delta)} \quad (6.57)$$

Therefore, the exponent $\gamma = 2 + \text{log-corrections}$, which we have numerically verified.

$D = 3$

We show that only M_2 diverges for $D = 3$, where $\tau = 5/2$. Equation 6.47 can be written as

$$\chi \simeq \frac{\sqrt{s_c \pi} \text{Erfc} \left[\frac{1}{\sqrt{s_c}} \right]}{\left[2 \exp \left(-\frac{1}{s_c} \right) - 2\sqrt{\pi} \text{Erfc}(s_c^{-1/2}) \right]} \quad (6.58)$$

We take the limit $s_c \rightarrow \infty$ to find that the denominator approaches 2 and the asymptotic scaling of the numerator determines the scaling of the response function,

$$\chi \sim \sqrt{s_c} \sim \Delta^{-1} \quad (6.59)$$

We show that the response function satisfies the equilibrium scaling law $\gamma = \frac{\tau-3}{\sigma}$ (Stanley, 1971). We start from Eq. 6.47, and consider only the scaling of the second moment

$$\chi \sim \int_{1/s_c}^{\infty} s_c^{3-\tau} y^{2-\tau} \exp(-y) dy \quad (6.60)$$

$$\sim s_c^{3-\tau} \sim \Delta^{\frac{\tau-3}{\sigma}}, \quad (6.61)$$

to find $\gamma = (3 - \tau)/\sigma$.

$D = 4$

We show that the response function diverges logarithmically for $T = 4$, where $\tau = 3$.

We start with Eq. 6.47,

$$\chi \simeq \frac{E_1(1/s_c)}{\exp(-1/s_c) - \Gamma(0, 1/s_c)/s_c}. \quad (6.62)$$

We consider the limit $s_c \rightarrow \infty$, the denominator approaches 1 and the numerator diverges as a log as seen in Eq. 6.55. Therefore χ scales as

$$\chi \sim \ln(s_c) \quad (6.63)$$

6.7 Discussion and Future work

We have presented some preliminary work on the scaling behavior of trapping times for random walkers. Our work highlights interesting behavior such as the fact that

the exponents τ and γ strongly depend on the dimension. Additionally, the dimension controls the lowest order moment that diverges and therefore it determines the order of the phase transition (Stanley, 1971).

Chapter 7

Conclusions and Future Work

We have applied the generalized the Fisher-Stauffer scaling, originally developed in percolation theory (Stauffer, 1979; Stauffer and Aharony, 2018), to study scale invariant avalanches in a simple model of earthquakes (Matin et al., 2020) and system of neurons (Martinello et al., 2017; Matin et al., 2021).

We show that Fisher-Stauffer scaling can be used to study noise-driven dynamical phase transition in the two-dimension OFC model with nearest-neighbor stress transfer (Matin et al., 2020). We plan to extend the Fisher-Stauffer scaling theory to the other noise driven transitions such as the synchronization-desynchronization transition in the Kuramoto model (Acebrón et al., 2005).

Our analysis of the two-dimensional OFC model with nearest-neighbor stress transfer shows that the bulk dissipation is the relevant scaling field, thereby ruling out self-organized criticality in the 2D OFC model. This work raises an important question about the BTW sandpile model (Bak et al., 1987) and the Manna model (Manna, 1991), which have been argued to be examples of self-organized criticality. Our hypothesis is that certain systems exhibit apparent SOC behavior because the relevant scaling field in the problem is simply tuned to the critical value in the model definition. We plan to apply the generalized Fisher-Stauffer scaling theory to the BTW (Bak et al., 1987) model and the Manna model (Manna, 1991) to analyze how the bulk dissipation affects the observed scaling behavior.

The 2D OFC model with long range stress transfer and spatial inhomogeneity

can capture interesting earthquake phenomenology such as Gutenberg-Richter scaling (Serino et al., 2011) and Omori’s law (Kazemian et al., 2015; Hergarten and Neugebauer, 2002), which describes the temporal clustering of earthquakes. Our analysis reveals that the temporal clustering of earthquakes in the OFC model exhibits strong non-stationary behavior. We intend to study how the non-stationary behavior of earthquakes affects our ability to forecast using machine learning algorithms such as Recurrent Neural Networks and Echo-State network (Mehta et al., 2019; LeCun et al., 2015), which learn from past data to make predictions about the future.

We have applied the Fisher-Stauffer scaling to a simple model of neurons (Martinello et al., 2017) and discussed how our derived scaling relations may be verified in future experiments (Langton, 1990; Beggs and Plenz, 2003; Bertschinger and Natschläger, 2004; Muñoz, 2018b; Kinouchi and Copelli, 2006). There is growing interest in the question of functional benefits of criticality in the brain (Muñoz, 2018a). Reference. (Beggs and Plenz, 2003) showed that information transmission is maximized for power-law distributed neural avalanches. Our results raise the important question of whether similar benefits are associated with causal neural avalanches (Matin et al., 2020) near the critical point. To address this question, we will apply the Fisher-Stauffer scaling to a neural system with spike-timing-dependent plasticity(STDP), which is a biological learning mechanism which uses causal information about firing neurons (Martinello et al., 2017; Stepp et al., 2015) to update synaptic weights between neurons. STDP has been shown to be responsible for maintaining stable retrievable firing patterns (Stepp et al., 2015). We plan to address the question of whether criticality enhances the number or stability of STDP firing patterns by studying causal neural avalanches in integrate and fire models of neurons.

We applied Fisher-Stauffer scaling to the return times of random walkers in ar-

bitrary dimensions and found that the dimension controls the different critical exponents and the order of the phase transition. We intend to study the random walk return times problem using the Parisi-Sourlas method (Parisi and Sourlas, 1979) to understand the thermodynamic properties of random walks.

Our work highlights the unreasonable effectiveness of scaling theory for models of earthquakes (Serino et al., 2011; Matin et al., 2020; Klein et al., 1997) and neural systems (Martinello et al., 2017; Fontenele et al., 2019b; Matin et al., 2021). The Fisher-Stauffer can be used to analyze the emergent scale invariant avalanches (Matin et al., 2020; Matin et al., 2021; Pun et al., 2020; Serino et al., 2011), which may be related to an underlying critical point (Serino et al., 2011; Matin et al., 2020; Matin et al., 2021; Pun et al., 2020). The successful application of the Fisher-Stauffer scaling theory to interdisciplinary problems also raises questions about necessary and sufficient conditions for using equilibrium tools for inter-disciplinary models (Matin et al., 2020). Our on-going work (Klein et al., b), indicates that the one-dimensional OFC model can be reformulated as a equilibrium thermodynamic problem. We intend to explore whether certain models of earthquakes (Olami et al., 1992; Rundle and Jackson, 1977) and neural systems (Hopfield and Herz, 1995; Millman et al., 2010a; Martinello et al., 2017) may also be in thermal equilibrium.

References

- Acebrón, J. A., Bonilla, L. L., Pérez Vicente, C. J., Ritort, F., and Spigler, R. (2005). The kuramoto model: A simple paradigm for synchronization phenomena. *Rev. Mod. Phys.*, 77:137–185.
- Arfken, G. B. and Weber, H. J. (1999). *Mathematical methods for physicists*.
- Azaele, S., Suweis, S., Grilli, J., Volkov, I., Banavar, J. R., and Maritan, A. (2016). Statistical mechanics of ecological systems: Neutral theory and beyond. *Rev. Mod. Phys.*, 88:035003.
- Bak, P., Tang, C., and Wiesenfeld, K. (1987). Self-organized criticality: An explanation of the $1/f$ noise. *Physical Review Letters*, 59:381–384.
- Bakun, W., Aagaard, B., Dost, B., Ellsworth, W., Hardebeck, J., Harris, R., Ji, C., Johnston, M., Langbein, J., Lienkaemper, J., et al. (2005). Implications for prediction and hazard assessment from the 2004 parkfield earthquake. *Nature*, 437(7061):969–974.
- Beggs, J. M. and Plenz, D. (2003). Neuronal avalanches in neocortical circuits. *Journal of neuroscience*, 23(35):11167–11177.
- Beggs, J. M. and Timme, N. (2012). Being critical of criticality in the brain. *Frontiers in physiology*, 3:163.
- Berman, G. and Izrailev, F. (2005). The fermi–pasta–ulam problem: fifty years of progress. *Chaos: An Interdisciplinary Journal of Nonlinear Science*, 15(1):015104.
- Bertschinger, N. and Natschläger, T. (2004). Real-time computation at the edge of chaos in recurrent neural networks. *Neural computation*, 16(7):1413–1436.
- Birzu, G., Matin, S., Hallatschek, O., and Korolev, K. S. (2019). Genetic drift in range expansions is very sensitive to density dependence in dispersal and growth. *Ecology Letters*, 22(11):1817–1827.
- Boedecker, J., Obst, O., Lizier, J. T., Mayer, N. M., and Asada, M. (2012). Information processing in echo state networks at the edge of chaos. *Theory in Biosciences*, 131(3):205–213.

- Bonachela, J. A. and Munoz, M. A. (2009). Self-organization without conservation: true or just apparent scale-invariance? *Journal of Statistical Mechanics: Theory and Experiment*, 2009(09):P09009.
- Boulter, C. J. and Miller, G. (2003). Nonuniversality and scaling breakdown in a nonconservative earthquake model. *Phys. Rev. E*, 68:056108.
- Bröker, H.-M. and Grassberger, P. (1997). Random neighbor theory of the olami-feder-christensen earthquake model. *Phys. Rev. E*, 56:3944–3952.
- Brown, S. R., Scholz, C. H., and Rundle, J. B. (1991). A simplified spring-block model of earthquakes. *Geophysical Research Letters*, 18(2):215–218.
- Burridge, R. and Knopoff, L. (1967). Model and theoretical seismicity. *Bulletin of the seismological society of america*, 57(3):341–371.
- Ceva, H. (1998). On the asymptotic behavior of an earthquake model. *Physics Letters A*, 245(5):413–418.
- Chabanol, M.-L. and Hakim, V. (1997). Analysis of a dissipative model of self-organized criticality with random neighbors. *Phys. Rev. E*, 56:R2343–R2346.
- Chen, C.-F. and Lin, C.-Y. (2009). Scalings of a modified manna model with bulk dissipation. *International Journal of Modern Physics C*, 20(02):273–284.
- Chialvo, D. R. (2010). Emergent complex neural dynamics. *Nature physics*, 6(10):744–750.
- Christensen, K. (1993). Christensen replies. *Physical review letters*, 71(8):1289.
- Christensen, K. and Olami, Z. (1992). Scaling, phase transitions, and nonuniversality in a self-organized critical cellular-automaton model. *Phys. Rev. A*, 46:1829–1838.
- Christensen, K., Olami, Z., and Bak, P. (1992). Deterministic $1/f$ noise in nonconservative models of self-organized criticality. *Physical Review Letters*, 68:2417–2420.
- Clawson, W. P., Wright, N. C., Wessel, R., and Shew, W. L. (2017). Adaptation towards scale-free dynamics improves cortical stimulus discrimination at the cost of reduced detection. *PLoS computational biology*, 13(5):e1005574.
- Clement, E. A., Richard, A., Thwaites, M., Ailon, J., Peters, S., and Dickson, C. T. (2008). Cyclic and sleep-like spontaneous alternations of brain state under urethane anaesthesia. *PloS one*, 3(4):e2004.
- Coniglio, A. and Klein, W. (1980). Clusters and Ising critical droplets: a renormalisation group approach. *Journal of Physics A: Mathematical and General*, 13(8):2775.

- Dalla Porta, L. and Copelli, M. (2019). Modeling neuronal avalanches and long-range temporal correlations at the emergence of collective oscillations: Continuously varying exponents mimic m/eeg results. *PLOS Computational Biology*, 15(4):e1006924.
- Das, A. and Levina, A. (2019). Critical neuronal models with relaxed timescale separation. *Phys. Rev. X*, 9:021062.
- Davidsen, J., Gu, C., and Baiesi, M. (2015). Generalized omori–utsu law for aftershock sequences in southern california. *Geophysical Journal International*, 201(2):965–978.
- de Carvalho, J. X. and Prado, C. P. C. (2000). Self-organized criticality in the olami-feder-christensen model. *Physical Review Letters*, 84:4006–4009.
- Dickman, R., Vespignani, A., and Zapperi, S. (1998). Self-organized criticality as an absorbing-state phase transition. *Phys. Rev. E*, 57:5095–5105.
- Ding, E. J. and Lu, Y. N. (1993). Analytical treatment for a spring-block model. *Physical Review Letters*, 70:3627–3630.
- Dominguez, R., Tiampo, K., Serino, C. A., and Klein, W. (2013). Scaling of earthquake models with inhomogeneous stress dissipation. *Phys. Rev. E*, 87:022809.
- Drossel, B. (2002). Complex scaling behavior of nonconserved self-organized critical systems. *Physical Review Letters*, 89:238701.
- Duan-Ming, Z., Fan, S., Bo-Ming, Y., Gui-Jun, P., Hong-Zhang, S., Yan-Ping, Y., Rui, L., and Xiang-Ying, S. (2006). Self-organized criticality in an earthquake model on random network. *Communications in Theoretical Physics*, 45(2):293.
- Eckmann, J.-P., Kamphorst, S. O., Ruelle, D., et al. (1995). Recurrence plots of dynamical systems. *World Scientific Series on Nonlinear Science Series A*, 16:441–446.
- Eurich, C. W., Herrmann, J. M., and Ernst, U. A. (2002). Finite-size effects of avalanche dynamics. *Phys. Rev. E*, 66:066137.
- Fisher, M. E. (1967). The theory of condensation and the critical point. *Physique Fizika*, 3:255–283.
- Fontenele, A. J., de Vasconcelos, N. A. P., Feliciano, T., Aguiar, L. A. A., Soares-Cunha, C., Coimbra, B., Dalla Porta, L., Ribeiro, S., Rodrigues, A. J. a., Sousa, N., Carelli, P. V., and Copelli, M. (2019a). Criticality between cortical states. *Physical Review Letters*, 122:208101.

- Fontenele, A. J., de Vasconcelos, N. A. P., Feliciano, T., Aguiar, L. A. A., Soares-Cunha, C., Coimbra, B., Dalla Porta, L., Ribeiro, S., Rodrigues, A. J. a., Sousa, N., Carelli, P. V., and Copelli, M. (2019b). Criticality between cortical states. *Physical Review Letters*, 122:208101.
- Frey, N. C., Matin, S., Stanley, H. E., and Salinger, M. A. (2019). Universal fluctuations in growth dynamics of economic systems. *Scientific reports*, 9(1):713.
- Friedman, N., Ito, S., Brinkman, B. A. W., Shimon, M., DeVille, R. E. L., Dahmen, K. A., Beggs, J. M., and Butler, T. C. (2012). Universal critical dynamics in high resolution neuronal avalanche data. *Physical Review Letters*, 108:208102.
- Gautam, S. H., Hoang, T. T., McClanahan, K., Grady, S. K., and Shew, W. L. (2015). Maximizing sensory dynamic range by tuning the cortical state to criticality. *PLoS computational biology*, 11(12):e1004576.
- Gleeson, J. P. and Durrett, R. (2017). Temporal profiles of avalanches on networks. *Nature communications*, 8(1):1227.
- Grassberger, P. (1993). On a self-organized critical forest-fire model. *Journal of Physics A: Mathematical and General*, 26(9):2081.
- Grassberger, P. (1994). Efficient large-scale simulations of a uniformly driven system. *Phys. Rev. E*, 49:2436–2444.
- Hahn, G., Ponce-Alvarez, A., Monier, C., Benvenuti, G., Kumar, A., Chavane, F., Deco, G., and Frégnac, Y. (2017). Spontaneous cortical activity is transiently poised close to criticality. *PLoS computational biology*, 13(5):e1005543.
- Haimovici, A., Tagliazucchi, E., Balenzuela, P., and Chialvo, D. R. (2013). Brain organization into resting state networks emerges at criticality on a model of the human connectome. *Physical Review Letters*, 110:178101.
- Haldeman, C. and Beggs, J. M. (2005). Critical branching captures activity in living neural networks and maximizes the number of metastable states. *Physical Review Letters*, 94:058101.
- Hankey, A. and Stanley, H. E. (1972). Systematic application of generalized homogeneous functions to static scaling, dynamic scaling, and universality. *Phys. Rev. B*, 6:3515–3542.
- Henkel, M., Hinrichsen, H., Lübeck, S., and Pleimling, M. (2008). *Non-equilibrium phase transitions*, volume 1. Springer.
- Hergarten, S. and Neugebauer, H. J. (2002). Foreshocks and aftershocks in the olami-feder-christensen model. *Physical Review Letters*, 88:238501.

- Herz, A. V. M. and Hopfield, J. J. (1995). Earthquake cycles and neural reverberations: Collective oscillations in systems with pulse-coupled threshold elements. *Physical Review Letters*, 75:1222–1225.
- Hinrichsen, H. (2000). Non-equilibrium critical phenomena and phase transitions into absorbing states. *Advances in Physics*, 49(7):815–958.
- Hohenberg, P. C. and Halperin, B. I. (1977a). Theory of dynamic critical phenomena. *Rev. Mod. Phys.*, 49:435–479.
- Hohenberg, P. C. and Halperin, B. I. (1977b). Theory of dynamic critical phenomena. *Rev. Mod. Phys.*, 49:435–479.
- Honey, C. J., Thesen, T., Donner, T. H., Silbert, L. J., Carlson, C. E., Devinsky, O., Doyle, W. K., Rubin, N., Heeger, D. J., and Hasson, U. (2012). Slow cortical dynamics and the accumulation of information over long timescales. *Neuron*, 76(2):423–434.
- Hopfield, J. J. and Herz, A. V. (1995). Rapid local synchronization of action potentials: Toward computation with coupled integrate-and-fire neurons. *Proceedings of the National Academy of Sciences*, 92(15):6655–6662.
- Hwa, T. and Kardar, M. (1989). Dissipative transport in open systems: An investigation of self-organized criticality. *Physical Review Letters*, 62:1813–1816.
- Hyman, A. A., Weber, C. A., and Jülicher, F. (2014). Liquid-liquid phase separation in biology. *Annual review of cell and developmental biology*, 30:39–58.
- Kadanoff, L. P., Nagel, S. R., Wu, L., and Zhou, S.-m. (1989). Scaling and universality in avalanches. *Phys. Rev. A*, 39:6524–6537.
- Kawamura, H., Hatano, T., Kato, N., Biswas, S., and Chakrabarti, B. K. (2012). Statistical physics of fracture, friction, and earthquakes. *Rev. Mod. Phys.*, 84:839–884.
- Kazemian, J., Tiampo, K. F., Klein, W., and Dominguez, R. (2015). Foreshock and aftershocks in simple earthquake models. *Physical Review Letters*, 114:088501.
- Kimura, M. (1991). The neutral theory of molecular evolution: A review of recent evidence. *The Japanese Journal of Genetics*, 66(4):367–386.
- Kinouchi, O. and Copelli, M. (2006). Optimal dynamical range of excitable networks at criticality. *Nature physics*, 2(5):348.
- Kinouchi, O., Pinho, S. T. R., and Prado, C. P. C. (1998). Random-neighbor olami-feder-christensen slip-stick model. *Phys. Rev. E*, 58:3997–4000.

- Klein, W., Gould, H., Gulbahce, N., Rundle, J. B., and Tiampo, K. (2007). Structure of fluctuations near mean-field critical points and spinodals and its implication for physical processes. *Phys. Rev. E*, 75:031114.
- ”Klein, W., Gould, H., and Matin, S. Cluster scaling and critical points: A cautionary tale(manuscript in preparation).
- ”Klein, W., Gould, H., Matin, S., and Leung, N. (manuscript in preparation).
- Klein, W. and Rundle, J. (1993). Comment on “self-organized criticality in a continuous, nonconservative cellular automaton modeling earthquakes”. *Physical Review Letters*, 71:1288–1288.
- Klein, W., Rundle, J. B., and Ferguson, C. D. (1997). Scaling and nucleation in models of earthquake faults. *Physical Review Letters*, 78:3793–3796.
- Kotani, T., Yoshino, H., and Kawamura, H. (2008). Periodicity and criticality in the olami-feder-christensen model of earthquakes. *Phys. Rev. E*, 77:010102.
- Langton, C. G. (1990). Computation at the edge of chaos: phase transitions and emergent computation. *Physica D: Nonlinear Phenomena*, 42(1-3):12–37.
- LeCun, Y., Bengio, Y., and Hinton, G. (2015). Deep learning. *nature*, 521(7553):436–444.
- Levina, A., Herrmann, J. M., and Geisel, T. (2009). Phase transitions towards criticality in a neural system with adaptive interactions. *Physical Review Letters*, 102:118110.
- Levina, A. and Priesemann, V. (2017). Subsampling scaling. *Nature communications*, 8:15140.
- Li, B.-Q. and Wang, S.-J. (2018). Self-organized criticality in an anisotropic earthquake model. *Communications in Theoretical Physics*, 69(3):280.
- Lise, S. (2002). Self-organization to criticality in a system without conservation law. *Journal of Physics A: Mathematical and General*, 35(22):4641.
- Lise, S. and Jensen, H. J. (1996). Transitions in nonconserving models of self-organized criticality. *Physical Review Letters*, 76:2326–2329.
- Lise, S. and Paczuski, M. (2001a). Scaling in a nonconservative earthquake model of self-organized criticality. *Phys. Rev. E*, 64:046111.
- Lise, S. and Paczuski, M. (2001b). Self-organized criticality and universality in a nonconservative earthquake model. *Phys. Rev. E*, 63:036111.

- Lo, C.-C., Amaral, L. N., Havlin, S., Ivanov, P. C., Penzel, T., Peter, J.-H., and Stanley, H. E. (2002). Dynamics of sleep-wake transitions during sleep. *EPL (Europhysics Letters)*, 57(5):625.
- Lo, C.-C., Chou, T., Penzel, T., Scammell, T. E., Strecker, R. E., Stanley, H. E., and Ivanov, P. C. (2004). Common scale-invariant patterns of sleep-wake transitions across mammalian species. *Proceedings of the National Academy of Sciences*, 101(50):17545–17548.
- Manna, S. S. (1991). Two-state model of self-organized criticality. *Journal of Physics A: Mathematical and General*, 24(7):L363–L369.
- Martinello, M., Hidalgo, J., Maritan, A., di Santo, S., Plenz, D., and Muñoz, M. A. (2017). Neutral theory and scale-free neural dynamics. *Phys. Rev. X*, 7:041071.
- Marwan, N., Romano, M. C., Thiel, M., and Kurths, J. (2007). Recurrence plots for the analysis of complex systems. *Physics reports*, 438(5-6):237–329.
- Massobrio, P., de Arcangelis, L., Pasquale, V., Jensen, H. J., and Plenz, D. (2015). Criticality as a signature of healthy neural systems. *Frontiers in systems neuroscience*, 9:22.
- Matin, S., Pun, C.-K., Gould, H., and Klein, W. (2020). Effective ergodicity breaking phase transition in a driven-dissipative system. *Phys. Rev. E*, 101:022103.
- Matin, S., Tenzin, T., and Klein, W. (2021). Scaling of causal neural avalanches in a neutral model. *Phys. Rev. Research*, 3:013107.
- Mehta, P., Bukov, M., Wang, C.-H., Day, A. G., Richardson, C., Fisher, C. K., and Schwab, D. J. (2019). A high-bias, low-variance introduction to machine learning for physicists. *Physics reports*, 810:1–124.
- Meisel, C., Olbrich, E., Shriki, O., and Achermann, P. (2013). Fading signatures of critical brain dynamics during sustained wakefulness in humans. *Journal of Neuroscience*, 33(44):17363–17372.
- Middleton, A. A. and Tang, C. (1995). Self-organized criticality in nonconserved systems. *Physical Review Letters*, 74:742–745.
- Miller, G. and Boultter, C. J. (2002). Measurements of criticality in the olami-feder-christensen model. *Phys. Rev. E*, 66:016123.
- Miller, G. and Boultter, C. J. (2003). Crossover behavior in the event size distribution of the olami-feder-christensen model. *Phys. Rev. E*, 67:046114.

- Millman, D., Mihalas, S., Kirkwood, A., and Niebur, E. (2010a). Self-organized criticality occurs in non-conservative neuronal networks during ‘up’states. *Nature physics*, 6(10):801.
- Millman, D., Mihalas, S., Kirkwood, A., and Niebur, E. (2010b). Self-organized criticality occurs in non-conservative neuronal networks during ‘up’states. *Nature physics*, 6(10):801.
- Mlodinow, L. (2009). *The drunkard’s walk: How randomness rules our lives*. Vintage.
- Mohanty, P. K. and Dhar, D. (2002). Generic sandpile models have directed percolation exponents. *Physical Review Letters*, 89:104303.
- Mora, T. and Bialek, W. (2011). Are biological systems poised at criticality? *Journal of Statistical Physics*, 144(2):268–302.
- Mousseau, N. (1996). Synchronization by disorder in coupled systems. *Physical Review Letters*, 77:968–971.
- Muñoz, M. A., , R., Vespignani, A., and Zapperi, S. (1999a). Avalanche and spreading exponents in systems with absorbing states. *Phys. Rev. E*, 59:6175–6179.
- Muñoz, M. A. (2018a). Colloquium: Criticality and dynamical scaling in living systems. *Rev. Mod. Phys.*, 90:031001.
- Muñoz, M. A. (2018b). Colloquium: Criticality and dynamical scaling in living systems. *Rev. Mod. Phys.*, 90:031001.
- Muñoz, M. A., Dickman, R., Vespignani, A., and Zapperi, S. (1999b). Avalanche and spreading exponents in systems with absorbing states. *Phys. Rev. E*, 59:6175–6179.
- Olami, Z. and Christensen, K. (1992). Temporal correlations, universality, and multifractality in a spring-block model of earthquakes. *Phys. Rev. A*, 46:R1720–R1723.
- Olami, Z., Feder, H. J. S., and Christensen, K. (1992). Self-organized criticality in a continuous, nonconservative cellular automaton modeling earthquakes. *Physical Review Letters*, 68:1244–1247.
- Onsager, L. (1944). Crystal statistics. i. a two-dimensional model with an order-disorder transition. *Physical Review*, 65(3-4):117.
- Pak, S. I. and Hayakawa, T. (2011). Forest fire modeling using cellular automata and percolation threshold analysis. In *Proceedings of the 2011 American Control Conference*, pages 293–298. IEEE.

- Palmer, R. (1982). Broken ergodicity. *Advances in Physics*, 31(6):669–735.
- Parisi, G. and Sourlas, N. (1979). Random magnetic fields, supersymmetry, and negative dimensions. *Physical Review Letters*, 43(11):744.
- Peixoto, T. P. and Davidsen, J. (2008). Network of recurrent events for the olami-feder-christensen model. *Phys. Rev. E*, 77:066107.
- Peixoto, T. P. and Prado, C. P. C. (2006). Network of epicenters of the olami-feder-christensen model of earthquakes. *Phys. Rev. E*, 74:016126.
- Perković, O., Dahmen, K., and Sethna, J. P. (1995). Avalanches, barkhausen noise, and plain old criticality. *Physical Review Letters*, 75:4528–4531.
- Petermann, T., Thiagarajan, T. C., Lebedev, M. A., Nicolelis, M. A. L., Chialvo, D. R., and Plenz, D. (2009). Spontaneous cortical activity in awake monkeys composed of neuronal avalanches. *Proceedings of the National Academy of Sciences*, 106(37):15921–15926.
- Peters, O. and Klein, W. (2013). Ergodicity breaking in geometric brownian motion. *Physical review letters*, 110(10):100603.
- Poil, S.-S., Hardstone, R., Mansvelder, H. D., and Linkenkaer-Hansen, K. (2012). Critical-state dynamics of avalanches and oscillations jointly emerge from balanced excitation/inhibition in neuronal networks. *Journal of Neuroscience*, 32(29):9817–9823.
- Ponce-Alvarez, A., Jouary, A., Privat, M., Deco, G., and Sumbre, G. (2018). Whole-brain neuronal activity displays crackling noise dynamics. *Neuron*, 100(6):1446–1459.
- Priesemann, V., Valderrama, M., Wibral, M., and Le Van Quyen, M. (2013). Neuronal avalanches differ from wakefulness to deep sleep—evidence from intracranial depth recordings in humans. *PLoS computational biology*, 9(3):e1002985.
- Priesemann, V., Wibral, M., Valderrama, M., Pröpper, R., Le Van Quyen, M., Geisel, T., Triesch, J., Nikolić, D., and Munk, M. H. (2014). Spike avalanches in vivo suggest a driven, slightly subcritical brain state. *Frontiers in systems neuroscience*, 8:108.
- Pun, C.-K., Matin, S., Klein, W., and Gould, H. (2020). Prediction in a driven-dissipative system displaying a continuous phase transition using machine learning. *Physical Review E*, 101(2):022102.
- Ramos, O., Altshuler, E., and Måløy, K. J. (2006). Quasiperiodic events in an earthquake model. *Physical Review Letters*, 96:098501.

- Redner, S. (2001). *A guide to first-passage processes*. Cambridge University Press.
- Reynolds, P., Stanley, H., and Klein, W. (1977). Ghost fields, pair connectedness, and scaling: exact results in one-dimensional percolation. *Journal of Physics A: Mathematical and General*, 10(11):L203.
- Ribeiro, T. L., Ribeiro, S., Belchior, H., Caixeta, F., and Copelli, M. (2014). Under-sampled critical branching processes on small-world and random networks fail to reproduce the statistics of spike avalanches. *PloS one*, 9(4):e94992.
- Roli, A., Villani, M., Filisetti, A., and Serra, R. (2018). Dynamical criticality: overview and open questions. *Journal of Systems Science and Complexity*, 31(3):647–663.
- Rubin, A. M. and Ampuero, J.-P. (2005). Earthquake nucleation on (aging) rate and state faults. *Journal of Geophysical Research: Solid Earth*, 110(B11).
- Rundle, J., Stein, S., Donnellan, A., Turcotte, D. L., Klein, W., and Saylor, C. (2021). The complex dynamics of earthquake fault systems: new approaches to forecasting and nowcasting of earthquakes. *Reports on progress in physics*.
- Rundle, J. B. and Jackson, D. D. (1977). Numerical simulation of earthquake sequences. *Bulletin of the Seismological Society of America*, 67(5):1363–1377.
- Rundle, J. B. and Klein, W. (1993). Scaling and critical phenomena in a cellular automaton slider-block model for earthquakes. *Journal of statistical Physics*, 72(1):405–412.
- Sahini, M. and Sahimi, M. (1994). *Applications of percolation theory*. CRC Press.
- Scarpetta, S. and de Candia, A. (2014). Alternation of up and down states at a dynamical phase-transition of a neural network with spatiotemporal attractors. *Frontiers in systems neuroscience*, 8:88.
- Serino, C. A., Tiampo, K. F., and Klein, W. (2011). New approach to gutenbergrichter scaling. *Physical Review Letters*, 106:108501.
- Sethna, J. (2021). *Statistical mechanics: entropy, order parameters, and complexity*, volume 14. Oxford University Press, USA.
- Sethna, J. P., Dahmen, K. A., and Myers, C. R. (2001). Crackling noise. *Nature*, 410(6825):242.
- Shew, W. L., Clawson, W. P., Pobst, J., Karimipannah, Y., Wright, N. C., and Wessel, R. (2015). Adaptation to sensory input tunes visual cortex to criticality. *Nature Physics*, 11(8):659.

- Shew, W. L. and Plenz, D. (2013). The functional benefits of criticality in the cortex. *The neuroscientist*, 19(1):88–100.
- Shew, W. L., Yang, H., Petermann, T., Roy, R., and Plenz, D. (2009). Neuronal avalanches imply maximum dynamic range in cortical networks at criticality. *Journal of neuroscience*, 29(49):15595–15600.
- Shriki, O., Alstott, J., Carver, F., Holroyd, T., Henson, R. N., Smith, M. L., Coppola, R., Bullmore, E., and Plenz, D. (2013). Neuronal avalanches in the resting MEG of the human brain. *Journal of Neuroscience*, 33(16):7079–7090.
- Sinai, Y. G. (1963). On the foundations of the ergodic hypothesis for a dynamical system of statistical mechanics. In *Doklady Akademii Nauk*, volume 153, pages 1261–1264. Russian Academy of Sciences.
- Smidt, S. (1968). A new look at the random walk hypothesis. *Journal of Financial and Quantitative Analysis*, 3(3):235–261.
- Smyth, W., Nash, J., and Moum, J. (2019). Self-organized criticality in geophysical turbulence. *Scientific reports*, 9(1):1–8.
- Sornette, A. and Sornette, D. (1989). Self-organized criticality and earthquakes. *EPL (Europhysics Letters)*, 9(3):197.
- Stanley, H. E. (1971). *Phase transitions and critical phenomena*. Clarendon Press, Oxford.
- Stanley, H. E. (1999). Scaling, universality, and renormalization: Three pillars of modern critical phenomena. *Rev. Mod. Phys.*, 71:S358–S366.
- Stanley, M. H., Amaral, L. A., Buldyrev, S. V., Havlin, S., Leschhorn, H., Maass, P., Salinger, M. A., and Stanley, H. E. (1996). Scaling behaviour in the growth of companies. *Nature*, 379(6568):804.
- Stauffer, D. (1975). Violation of dynamical scaling for randomly dilute ising ferromagnets near percolation threshold. *Physical Review Letters*, 35:394–397.
- Stauffer, D. (1979). Scaling theory of percolation clusters. *Physics Reports*, 54(1):1–74.
- Stauffer, D. and Aharony, A. (2018). *Introduction to percolation theory*. CRC press.
- Stavroglou, S. K., Pantelous, A. A., Stanley, H. E., and Zuev, K. M. (2020). Unveiling causal interactions in complex systems. *Proceedings of the National Academy of Sciences*, 117(14):7599–7605.

- Stella, A. L. and De Menech, M. (2001). Mechanisms of avalanche dynamics and forms of scaling in sandpiles. *Physica A: Statistical Mechanics and its Applications*, 295(1-2):101–107.
- Stepp, N., Plenz, D., and Srinivasa, N. (2015). Synaptic plasticity enables adaptive self-tuning critical networks. *PLoS computational biology*, 11(1):e1004043.
- Stoop, R. and Gomez, F. (2016). Auditory power-law activation avalanches exhibit a fundamental computational ground state. *Physical Review Letters*, 117:038102.
- Stumpf, M. P. and Porter, M. A. (2012). Critical truths about power laws. *Science*, 335(6069):665–666.
- Tebaldi, C., De Menech, M., and Stella, A. L. (1999). Multifractal scaling in the Bak-Tang-Wiesenfeld sandpile and edge events. *Physical Review Letters*, 83:3952–3955.
- Tél, T. (1988). Fractals, multifractals, and thermodynamics. *Zeitschrift für Naturforschung A*, 43(12):1154–1174.
- Thirumalai, D. and Mountain, R. D. (1990). Ergodic convergence properties of supercooled liquids and glasses. *Phys. Rev. A*, 42:4574–4587.
- Thirumalai, D. and Mountain, R. D. (1993). Activated dynamics, loss of ergodicity, and transport in supercooled liquids. *Phys. Rev. E*, 47:479–489.
- Thirumalai, D., Mountain, R. D., and Kirkpatrick, T. R. (1989). Ergodic behavior in supercooled liquids and in glasses. *Phys. Rev. A*, 39:3563–3574.
- Torvund, F. and Frøyland, J. (1995). Strong ordering by non-uniformity of thresholds in a coupled map lattice. *Physica Scripta*, 52(6):624.
- Turcotte, D. L. (1999). Self-organized criticality. *Reports on progress in physics*, 62(10):1377.
- Van Kessenich, L. M., de Arcangelis, L., and Herrmann, H. (2016). Synaptic plasticity and neuronal refractory time cause scaling behaviour of neuronal avalanches. *Scientific reports*, 6:32071.
- Vasarhelyi, B. and Ván, P. (2006). Influence of water content on the strength of rock. *Engineering Geology*, 84(1-2):70–74.
- Veedu, D. M. and Barbot, S. (2016). The parkfield tremors reveal slow and fast ruptures on the same asperity. *Nature*, 532(7599):361–365.
- Vespignani, A. and Zapperi, S. (1997). Order parameter and scaling fields in self-organized criticality. *Physical Review Letters*, 78:4793–4796.

- Vicsek, T., Czirók, A., Ben-Jacob, E., Cohen, I., and Shochet, O. (1995). Novel type of phase transition in a system of self-driven particles. *Physical Review Letters*, 75:1226–1229.
- Villegas, P., di Santo, S., Burioni, R., and Muñoz, M. A. (2019). Time-series thresholding and the definition of avalanche size. *Phys. Rev. E*, 100:012133.
- Wesnowsky, S. G. (1994). The gutenbergrichter or characteristic earthquake distribution, which is it? *Bulletin of the Seismological Society of America*, 84(6):1940–1959.
- Williams-García, R. V., Beggs, J. M., and Ortiz, G. (2017). Unveiling causal activity of complex networks. *EPL (Europhysics Letters)*, 119(1):18003.
- Wilson, K. G. (1979). Problems in Physics with many Scales of Length. *Scientific American*, 241(2):158–179.
- Wilson, K. G. (1983). The renormalization group and critical phenomena. *Rev. Mod. Phys.*, 55:583–600.
- Wissel, F. and Drossel, B. (2006). Transient and stationary behavior of the olami-feder-christensen model. *Phys. Rev. E*, 74:066109.
- Yu, S., Yang, H., Shriki, O., and Plenz, D. (2013). Universal organization of resting brain activity at the thermodynamic critical point. *Frontiers in systems neuroscience*, 7:42.
- Zapperi, S., Cizeau, P., Durin, G., and Stanley, H. E. (1998). Dynamics of a ferromagnetic domain wall: Avalanches, depinning transition, and the barkhausen effect. *Phys. Rev. B*, 58:6353–6366.
- Zierenberg, J., Wilting, J., and Priesemann, V. (2018a). Homeostatic plasticity and external input shape neural network dynamics. *Phys. Rev. X*, 8:031018.
- Zierenberg, J., Wilting, J., and Priesemann, V. (2018b). Homeostatic plasticity and external input shape neural network dynamics. *Phys. Rev. X*, 8:031018.
- Zierenberg, J., Wilting, J., Priesemann, V., and Levina, A. (2020). Description of spreading dynamics by microscopic network models and macroscopic branching processes can differ due to coalescence. *Phys. Rev. E*, 101:022301.
- Zwanzig, R. (2001). *Nonequilibrium statistical mechanics*. Oxford university press.

CURRICULUM VITAE

